Inverse Heat Conduction Approach for Infrared Non-destructive Testing of Single and Multi-Layer Materials

by

Ehsan Borazjani

Thesis submitted to the
Faculty of Graduate and Postdoctoral Studies
In partial fulfillment of the requirements
For the M.A.Sc. degree in
Mechanical Engineering

Department of Mechanical Engineering
Faculty of Engineering
University of Ottawa

Abstract

The focus of this thesis is to derive analytical tools for the design of infrared nondestructive tests in single and multi layer material bodies. This requires the predetermination of the parameters of the experiment such that the infrared image has the required resolution for defect detection.

Inverse heat conduction in single and multi-layer materials is investigated to determine the required frequency of excitation in order to obtain a desired temperature at the observation point. We use analytical quadrupole representation to derive a polynomial relation to estimate the frequency of the periodic excitation as a function of the temperature amplitude at a given observation point within the body. The formula includes characteristic geometric and material parameters of the system. The polynomial formula can be an effective design tool for quick frequency predetermination in the design of non-destructive testing experiments with infrared thermography. The convergence and accuracy of the formula is assessed by comparison with the analytical thermal quadrupole solution and experimental results.

We also investigate the effect of the finite length of the material domain in order to establish the range of applicability of a simplified formula based on semi-infinite domain assumption. The effect of finite length is investigated analytically by using (i) Fourier series which accounts for transients and (ii) Time varying solution associated to the steady state solution when a purely periodic excitation is applied. These results are also compared with numerical solution obtained with commercial finite element software ANSYS^{TM}.

Acknowledgements

I would like to thank all the people who have been a constant support and whose wisdom has inspired me throughout my Masters study.

First and foremost, I would like to offer my especial gratitude to my supervisors, professor D. Necsulescu and D. Spinello for their guidance, supervision and support from the early stage of this research. They were always accessible and willing to help which enabled me to carry out my research in a much more effective way. I am very grateful for their patience and understanding.

I would like to thank Dr. Robitaille for his generous help and support to run the experiment by providing us with his IR camera.

It is a pleasure to thank my best friend and graduate student at university of Ottawa, Houman Rastegar for his friendship, help and his knowledge and experience.

My deepest gratitude goes to my family, Sadegh, Azar and Iman Borazjani for their all kinds of support, spiritually and financially, through my life. They spare no effort to provide the best possible environment for me to continue my education. They have always been a constant source of encouragement during my graduate study.

Finally, I would like to thank everybody who was important to the successful realization of thesis, as well as expressing my apology that I could not mention personally one by one.

Contents

1 Introduction **1**

1.1 Overview 1

1.2 Research Objective 2

1.3 Outline of the Thesis 3

2 Literature Review **5**

2.1 Non Destructive Testing 5

2.1.1 Overview 5

2.2 Non Destructive Testing Methods 6

2.2.1 Radiography 6

2.2.2 Ultrasonic 8

2.2.3 Eddy Current 9

2.3 Infrared Thermography 10

2.3.1 Overview 10

2.3.2 Background and History 11

2.3.3 Infrared Fundamentals 11

2.3.4 Approaches in infrared thermography 14

2.3.5 Modeling in infrarerd thermography 17

2.3.6 Heat Transfer Fundamental 21

3 Governing equations **23**

3.1 Heat conduction in a multi-layer slab 23

3.1.1 Thermal Quadrupole Method 25

4 Approximate closed form solution for damage detection in multi-layer materials **29**

4.1 Introduction 29

4.2 Approximate solution of the inverse problem 30
4.2.1 Homogeneous slab 32
4.2.2 Two layer slab 34
4.3 Inclusion at the interface 38
4.3.1 Approximation of air gap at the interface with resistance R 39
4.3.2 Detachment at the interface approximated by a capacitance . . . 43

5 Effect of the finite length of the domain in the problem of frequency predetermination 49
5.1 Introduction 49
5.2 Fourier series solution 49
5.2.1 Approximate eigenfrequencies 53
5.2.2 Error of eigenvalues approximation 54
5.3 Periodic solution 56
5.4 Results and Comparison 58

6 Experimental validation 65
6.1 Introduction 65
6.2 Experiment design 65
6.2.1 Material and geometry 65
6.2.2 Experiment set-up 67
6.2.3 Experiment 67

7 Summary and Future work 77
7.1 Summary of contributions 77
7.2 Future work 78

A MATLAB codes 79
A.1 MATLAB code for single layer wall with persistant sinusoidal osciliation on the boundary 79
A.2 MATLAB code for single layer wall in Fourier series 80
A.3 MATLAB code for single layer wall using quadrupole method 81
A.4 MATLAB code for two layer wall using quadrupole method with inclusion at the interface (Resistance and Capacitance) 82

Bibliography 85

List of Tables

4.1 Nondimensional parameters for two layer material with observation point at the interface 36

4.2 Comparison between analytical solution, quadrupole method with approximation with R 40

5.1 Numerical values for the approximation of $\tan(\lambda_n l) = \frac{-k}{\mu}\lambda_n$ 54

6.1 FLIR $i7$ specification 68

6.2 Required time for excitation in experiment for different ω 68

List of Figures

2.1 Typical radiography set-up [26] 7
2.2 Typical arrangement for ultrasonic testing [26] 8
2.3 Typical arrangement for Eddy Current [12] 10
2.4 Electromagnetic spectrum [13] 12
2.5 Sketch showing incident energy(pics from google) 13
2.6 Set-up for pulse thermography [40] 15
2.7 Set-up for Lock-in thermography (from [56] 16
2.8 Sensitivity coefficient for defects at different depth considering properties (a)depth, (b)thermal conductivity and(c) heat capacity [29]. 18

3.1 Two layer model with sinusoidal excitation in front face and convection at rear face 24
3.2 For a two layers slab, lumped parameters representation of the linear system (3.10) via thermal quadrupoles, with an observation point x located within layer 1. The case with observation point located in layer 2 can be easily obtained. 27

4.1 Plots of β_1 versus $|U_x(\jmath\beta_1)|$ from the analytical quadrupoles solution (solid line), and the approximated polynomial solution with $N = 1$ (dashed line) and $N = 2$ (dot-dashed line) for a homogeneous slab. 33
4.2 Plots of the relative percentage error $100\,|1 - \beta_1^a/\beta_1|$ versus $|U_x|$ for $N = 1$ (solid line) and $N = 2$ (dashed line) 34
4.3 Plots of β_1 versus $|U_x(\jmath\beta_1)|$ from the analytical quadrupoles solution (solid line), and the approximated polynomial solution with $N = 1$ (dashed line) and $N = 2$ (dot-dashed line) for a two layer slab. 36
4.4 Plots of the relative percentage error $100\,|1 - \beta_1^a/\beta_1|$ versus $|U_x|$ for $N = 1$ (solid line) and $N = 2$ (dashed line) (Two layer slab). 37

4.5 For a two layer slab comprised of carbon steel and aluminum, plot of the frequency of excitation ω versus $|u_x|/U$. 38
4.6 Schematic of the two-layer slab with an inclusion at the interface and the boundary condition of the sinusoidal excitation on one side and convection on the other side. q and q_{inc} are the flux at interface for perfect contact and inclusion, respectively 39
4.7 Temperature distribution through the domain with an inclusion (resistance) at the interface 40
4.8 Plots of the left hand side of (4.6) versus β_1 for $n = 2$ (dashed line0 and $n = 3$ (dashed-dotted line). The solid line is the graph (versus β_1) of the right-hand side for $|u_2| = 0.6289$ 43
4.9 Temperature distribution through the domain with a high conductive inclusion at the interface. 44
4.10 Comparison between the analytical solution (solid line) and approximation of the inclusion with C_t (dashed line) 46
4.11 Plots of the left hand side of (4.6) versus β_1 for $n = 2$ (dashed line and $n = 3$ (dashed-dotted line). The solid line is the graph (versus β_1) of the right-hand side for $|u_2| = 0.3403$ 48

5.1 Plot of the function $\tan \lambda l$ vs. λl and of the line $-\frac{k}{\mu l}\lambda l$ vs. λl for three values of the non dimensional group $\frac{k}{\mu l}\lambda l$, that is 10,15, and 20. Circles are located on the first root of the characteristic equation (5.12) 54
5.2 Relative error introduce by the approximated frequency vs. $k/\mu l \in [0.2, 20]$ for $n = 1, 2, 3$ (respectively: continuous line, dashed line, dashed-dotted line). 55
5.3 Temperature profile in space coordination corresponding to Fourier series solution. 59
5.4 Temperature profile in space coordination corresponding to periodic solution. 59
5.5 For $l = 1m$,$t = 300sec$, and $x = 0.03m$ plots of ω versus $|u_{ss}|$ corresponding to semi-infinite solution (solid line), Fourier series solution in the finite domain (dashed line), and ANSYS numerical simulation(*). 60
5.6 For $l = 1m$,$t = 300sec$, and $x = 0.03m$ plots of ω versus $|u_{ss}|$ corresponding to semi-infinite solution (solid line), Periodic solution in the finite domain (dotted-dashed line), and ANSYS numerical simulation (*). . . . 61

5.7 For $l = 0.03m$,$t = 300sec$, and $x = 0.03m$ plots of ω versus $|u_{ss}|$ corresponding to semi-infinite solution (solid line), Fourier series solution (dashed line), Periodic solution in the finite domain (dotted-dashed line), and ANSYS numerical simulation (*). 62
5.8 Plot of the relative error function $\epsilon(0.03, l)$ versus l for $\omega = 0.01rad/sec$(dotted-dashed line), $\omega = 0.06rad/sec$(dashed line), $\omega = 0.11rad/sec$(solid line). . 62
5.9 Plot of the first four fitting coefficients in (5.42) for $x = 0.03m$. Fine dashed, coarse dashed, continuous, and dashed-dotted lines correspond respectively to fitting coefficients with increasing index. Material is carbon steel. 64
5.10 Plot of the first four fitting coefficients in (5.42) for $x = 0.03m$. Fine dashed, coarse dashed, continuous, and dashed-dotted lines correspond respectively to fitting coefficients with increasing index. Material is aluminum. 64

6.1 Illustrate the specimen with defects, $\phi = 2''$, $\phi = 1''$ and $\phi = 0.5''$ 66
6.2 Experimental set-up for infrared thermography 67
6.3 Plot of frequency of excitation versus temperature at observation point for acrylic glass with the thickness 6 mm 69
6.4 Image of temperature distribution for the defect size $\phi = 0.5''$ with the excitation frequency $\omega = 0.02\ rad/sec$ 70
6.5 Image of temperature distribution for the defect size $\phi = 0.5''$ with the excitation frequency $\omega = 0.05\ rad/sec$ 70
6.6 Image of temperature distribution for the defect size $\phi = 0.5''$ with the excitation frequency $\omega = 0.15\ rad/sec$ 71
6.7 Image of temperature distribution for the defect size $\phi = 1''$ with the excitation frequency $\omega = 0.02\ rad/sec$ 71
6.8 Image of temperature distribution for the defect size $\phi = 1''$ with the excitation frequency $\omega = 0.05\ rad/sec$ 72
6.9 Image of temperature distribution for the defect size $\phi = 1''$ with the excitation frequency $\omega = 0.15\ rad/sec$ 72
6.10 Image of temperature distribution for the defect size $\phi = 2''$ with the excitation frequency $\omega = 0.02\ rad/sec$ 73
6.11 Image of temperature distribution for the defect size $\phi = 2''$ with the excitation frequency $\omega = 0.05\ rad/sec$ 73

6.12 Image of temperature distribution for the defect size $\phi = 2''$ with the excitation frequency $\omega = 0.15\ rad/sec$ 74
6.13 Plots of frequency of excitation versus temperature at observation point for comparison between the experiment result (*), approximation solution, (4.7c), for $N = 1$(dashed line),and approximation solution for $N = 3$ (dotted-dashed line) for material acrylic glass with the thickness of $6mm$. 75
6.14 Plots of frequency of excitation versus temperature at observation point for comparison between the experiment result (*), approximation solution, (4.7c), for $N = 1$(dashed line),and approximation solution for $N = 3$ (dotted-dashed line) for two-layer panel with the thickness of $6mm$. . . . 76

Chapter 1

Introduction

1.1 Overview

Non destructive testing is used in industrial and scientific applications to detect surface and subsurface defects of material specimens. Non destructive testing includes a wide range of techniques among which the most common are: infrared thermography, ultrasonic, eddy-current testing, magnetic-particle and radiography. Each method has advantages and disadvantages which lead to different applications.

In the past few decades, the interest in infrared thermography has grown among scientists and researchers. Reasonable accuracy, non-contact technique, low-cost developments, no or less damage on testing object and inspection under normal operating condition are some of the reasons of attention to this technique [3, 34]. These advantages give high potential and active applications for infrared thermography to be used in different fields such as aerospace, civil engineering, biomedical, electronics, and environment. Some of these applications are:

- *Medicine*: study of body temperature which can be used for tumor diagnosis, and open heart surgery [34].
- *Non-destructive evaluation*: detecting a defect and its characteristics in wide variety of material and components.
- *Environment*: monitoring and investigating the pollution in the sea, river coastal and landfill or information about indoor climate, building and road thermal mapping [6, 32].

- *Maintenance*:by infrared thermography all the instruments in electric power plant and also all mechanical parts like, pumps, motors, and bearing can be inspected. These thermogrpahy images give this opportunity to predict any failure which saves money, time and also avoids damage [34].

- *Agriculture*: study the process of ice nucleation and ice propagation in sensitive plants like fruit trees [54].

Infrared thermography is based on electromagnetic radiation. Electromagnetic radiation emits from any objects above temperature of absolute zero [34]. This thermal energy can be captured by a camera and transformed in to the electronic signal which leads to the visible image. Since the camera captures the temperature distribution on the surface which is $2D$, infrared thermography can be categorized as two-dimensional technique for temperature measurements [34].

Active and passive thermography are the two main approaches in infrared thermography. In active thermography, the tested object is excited by external sources by heating or cooling it. In passive thermography, the natural temperature between the ambient and tested object is measured. The surface image can be seen in different colors or different shades of grey. The color changes with respect to the temperature at each point of surface, and by analyzing it, defects can be detected. Also, thermal constitutive properties such as thermal conductivity and heat capacity can be obtained by infrared thermography.

The first technology advances in infrared imaging were started during World War II [34]. Afterwards, the technique was extended to other fields such as medical, agriculture, and environment. Despite the substantial advances, several unknown factors still need investigation in order to improve the detectability prediction and the consequent resolution of thermal images.

1.2 Research Objective

The primary objective of this thesis is to investigate the inverse heat conduction problem in a solid slab in order to obtain the boundary temperature corresponding to a given amplitude in the body. This allows for the predetermination of the excitation temperature in the design of infrared thermography tests. We derive approximated closed form solutions of the inverse problem in a multi-layer heat conductive slab, formalized by formulas that express the frequency of the boundary temperature excitation in terms of

the observation point in the domain and the related temperature amplitude. Ultimately, such formulas allow for the quantification of the detectability of a defect in terms of the frequency of the boundary excitation.

Experimental validation of the proposed formulas is done through a sinusoidal excitation exerted by a infrared lamp while infrared camera captures the temperature distribution on the surface. This temperature distribution correlates size and characteristics of the flaws which can be rendered to identify possible anomalies by detecting patterns associated with reflected thermal waves. Based on the characteristics of the temperature distribution, effective experimental design requires predetermination of the frequency of excitation that corresponds to certain temperature amplitude at the observation point.

Another objective of this thesis is to investigate the effect of the finite length of the material specimen in order to establish the range of applicability of the modeling assumption of semi-infinite domain. This assumption was exploited in [38] to obtain a closed form solution relation between the temperature amplitude in the domain and the frequency of excitation associated to such amplitude

1.3 Outline of the Thesis

The Thesis is organized as follows:

Chapter 1: Overview and research objectives

Chapter 2: Summarizes the non-destructive testing and its existing techniques, recent developments in infrared thermography, heat transfer fundamentals

Chapter 3: Heat conduction in multi-layer slab with its boundary condition and a brief description about thermal quadrupole method and its derivation are presented.

Chapter 4: Inverse heat conduction in a single and multi-layer material is investigated. Non-dimensional thermal quadrupole method is considered to obtain a transfer function between the frequency of excitation and temperature at observation point. The generally transcendental transfer function is approximated with a power series, which allows for a polynomial implicit approximated solution of the inverse problem. In addition, polynomial implicit approximated solution for two different possible imperfections at interface, air gap and detachment, is presented.

Chapter 5: Fourier series and periodic time varying solution are used to investigate the effect of the finite length and therefore the range of applicability of the semi-infinite domain modeling assumption.

Chapter 6: The aim of this part is to verify the theoretical results experimentally. At first, healthy objects (single and two-layer) are excited with a sinusoidal boundary temperature with frequency of excitation determined by the formulas derived in Chapter 4. The temperature at the observation point is captured by an infrared camera in order to record the frequency of excitation versus temperature at observation point.

Chapter 7: Summary and future work

Appendix A: The MATLAB codes regarding the Fourier series and periodic solution for single layer and quadrupole method for two-layer material are presented.

Chapter 2

Literature Review

2.1 Non Destructive Testing

2.1.1 Overview

Non-destructive testing is a wide group of analysis techniques used to evaluate and determine material or any component or system's property, flaws, leaks, discontinuity and any imperfection without impairing the integrity or function of the tested object. Non-destructive testing has a long history, however, it has mainly become popular in the past 50 years. One of the first times that nondestructive testing was used dates back to 1895 when X-ray was discovered by Wilhelm Conrad Roentgen (1845-1923) [26]. The importance of non-destructive testing, however, became much clearer after World War II. In the post war era, modern industry developed very fast and the needs for flawless material and testing equipment increased. Therefore, equipments and new methods for non-destructive testing were developed.

Non destructive evaluation is a term which is often used as a synonymous of non-destructive testing. Non-destructive evaluation is used to detect the material flaws and to obtain information about the characteristics of the flaws such as size, shape and orientation [26]. Non-destructive evaluation can be used for real-time monitoring during manufacturing to find out defects induced during design-through-manufacturing process [53].These abilities make this method to be widely used in several fields such as structural and civil engineering, [16, 9], material and aerospace engineering [35, 36, 22]. Environmental and liability concerns have also resulting in increased use of non-destructive evaluation [53].

Quality control is another valuable capability of non-destructive testing. Safety and

reliability are the two main factors in design and manufacturing of materials or systems [33, 14]. Any defect during manufacturing or a weak design may cause an unexpected failure, the result of which could be an expensive repair or early replacement that imposes excessive cost or may threaten human life in working areas [33]. To assure good quality control a complete knowledge of the limitations and capabilities of different methods in non-destructive testing is needed. In addition, a certain degree of skill is required to apply the techniques properly in order to obtain the maximum amount of information concerning the product [53].

Non-destructive testing has wide range of uses incorporating various methodologies and it is constantly improved with new methods and techniques. Moreover, new technology and improvements in other fields like computers, optical fibers, laser and imaging technology (including video, holography and thermography) [53] make non-destructive testing methods easier to use and more accurate.

2.2 Non Destructive Testing Methods

2.2.1 Radiography

Radiography is applied to detect defects in ferrous and nonferrous materials. Radiography was discovered in 1895 by Wilhelm Conrad Roentgen (1845-1923) who was a Professor at Wuerzburg University in Germany [26]. The first use of radiography is recorded six months after its discovery when physicians used it to help in surgery on wounded soldiers [26].

Radiography is based on X-ray and Gamma-ray which are short wavelength electromagnetic radiations with the ability to penetrate various materials. The energy associated to the radiation is absorbed by the material in a characteristic way which is determined by the properties of the specimen. By directing the radiation to a film anomalies are detected due to differential absorption properties of related areas. The clarity of the film is related to the intensity of the radiation which reaches the film. For example, imperfections like a void in the material appear as darkened areas in the film because of increased intensity from the radiation see, figure 2.1.

One of the new developments in radiography is real time radiography in which the film is replaced by digital imaging production [26]. It finds various applications in automotive, aerospace, pressure vessels, and electronics. Reduced equipment cost and also increased the quality of images (digital) are two of the reasons that have made this method well-

established in industry.

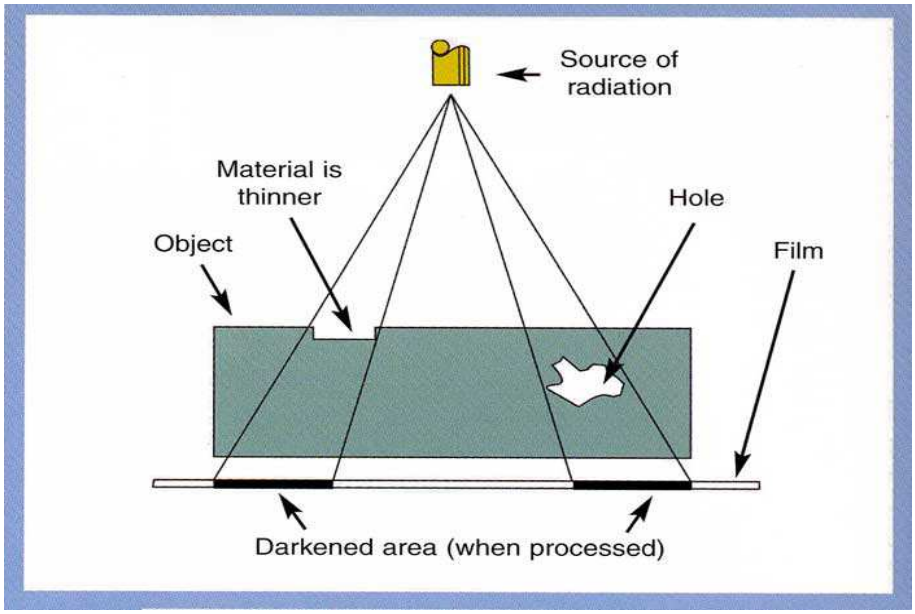

Figure 2.1: Typical radiography set-up [26]

Some of the advantages of the method are:

- good results for thin materials
- preservation of film
- visual result
- can be used for any material

Main disadvantages are:

- not accurate for thick sections
- negative effects on human
- not suitable for surface defects
- does not show the depth of defects

2.2.2 Ultrasonic

Ultrasonic is a method which is used to detect surface and subsurface defects. The idea of using sound energy signal has been exploited prior to World War II to detect submerged objects. This idea inspired researches to develop ultrasound techniques for medical purposes. After 1970's, improvements in technology and emerging the discipline of fracture mechanics (fatigue) caused a major developments in ultrasonic non destructive testing [26].

Ultrasound techniques are based on high frequency traveling sound wave and on the analysis of the reflected wave. The wave propagates in the material and portion of it reflects when it reaches any cracks or flaws, figure 2.2. By analyzing the signal associated with reflected waves, flaws and their characteristics such as kind, size, and depth can be detected. Other applications of this method are leak detection, steam trap assessment, energy saving, material properties and predictive maintenance [26].

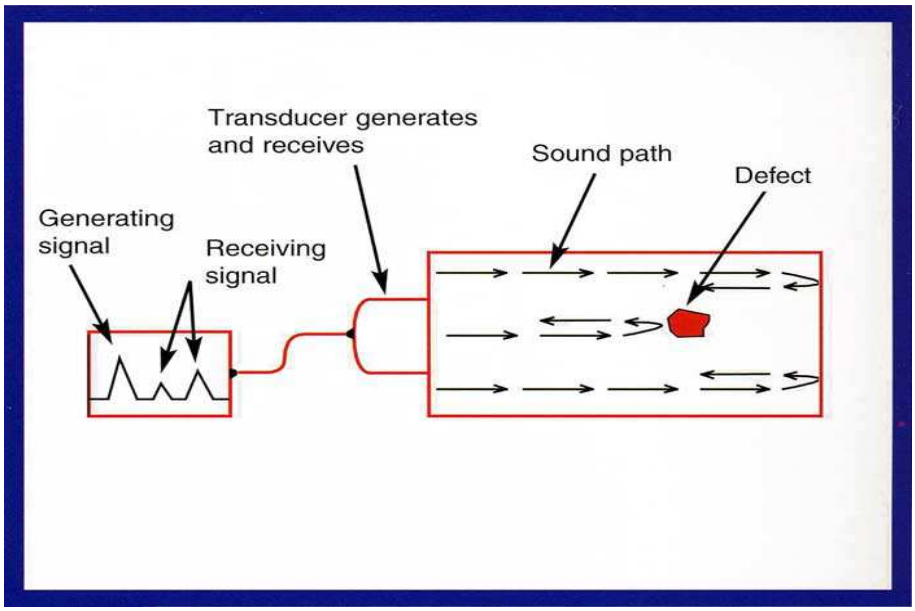

Figure 2.2: Typical arrangement for ultrasonic testing [26]

Advantages:

- good for material with thickness or length up to 30 ft
- gives information about characteristic and position of a defect
- real-time test results

- portable
- only one side is needed for test

Disadvantages:

- probe should have an access to the surface
- hard to inspect irregular shape, rough material
- not good for very small and thin material
- the technician should have certain skill and reference standards are required

2.2.3 Eddy Current

Eddy current is a well-established method for inspection. This method was developed during and after World War II, but it was discovered by Michael Faraday in 1831.

By passing an alternative current through a probe (coil), an electromagnetic field is produced around the probe figure 2.3. If another conductive material (test object) enters this field, the alternative field induces eddy current in the test object. If any flaws are in the testing object, eddy current changes and this change affects coil impedance which is measurable [26]. The return signal from probe is processed to extract information about the characteristics and position of the defects.

This method has also some advantages and limitations:

Advantages are:

- detects small cracks
- good for surface and near surface inspection
- instant test results
- portable
- complex shape can be tested

Limitations are:

- only can be used for conductive materials
- limited depth of penetration

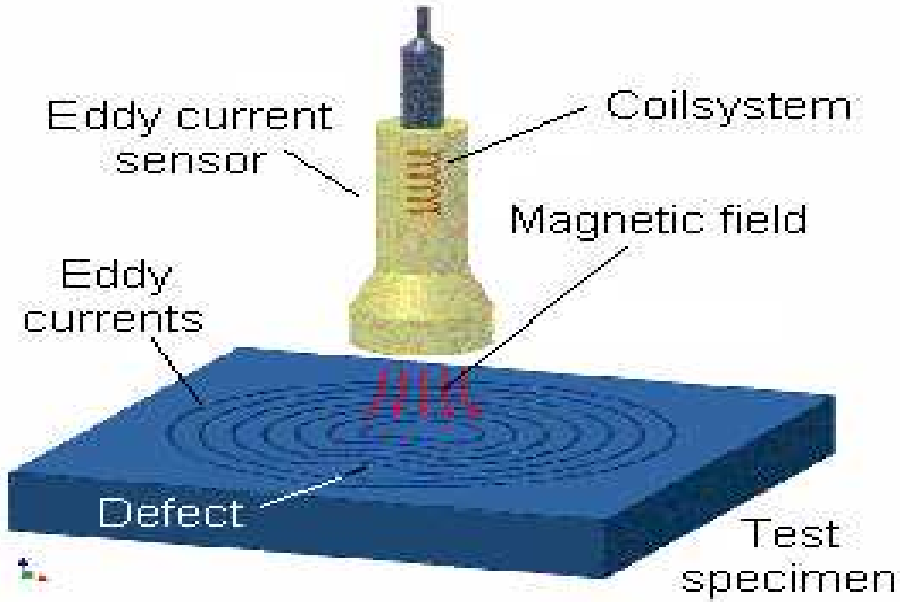

Figure 2.3: Typical arrangement for Eddy Current [12]

- quality of surface can affect the result
- probe should have an access to the testing object

2.3 Infrared Thermography

2.3.1 Overview

Infrared thermography is an inspection method in non-destructive testing to detect defects on the surface and inside objects. It is a no-contact method and the inspection can be implemented by exposing the object to infrared thermal waves. Infrared is invisible and it is associated to heating effects. The heat distribution can be captured by camera. By analyzing the image, position and characteristics of the defects can be detected.

Infrared thermography has several applications in different fields such as material property estimation, detecting defects in pipe or other plastic or metal material, heating-ventilation and air conditioning systems, biomedical application, civil engineering and art [8, 20, 50, 28, 44].

2.3.2 Background and History

Infrared energy was discovered in 19th century by Sir William Herschel. Infrared energy is the invisible part of electromagnetic spectrum with wave length of $0.7 - 1000\mu m$. However it was not until 1830 that thermopiles developed to measure the testing object surface temperature. A thermopile is made of thermocouples connected in series. A thermocouple is made of two metal strips which are connected together from one end. A temperature differences at the junction induces a voltage difference. The phenomenon is known as Seebeck effect.

Around 1880, it was discovered that material resistivity varies with temperature. Based on this discovery, the bolometer was developed by Samuel Langley and it had a great influence on infrared detecting sensitivity. Quantum detector was another development during 1870-1920 which was the result of technological advances. Early thermal detector had a low sensitivity and slow response [57]. Quantum detector directly converts a quantum of radiation to an electrical signal instead of converting heating effect of radiation to electrical signal. As a result, the photoconductor was developed which was faster (shorter time response), more accurate and was more sensitive. In late 1940, the first practical infrared detectors was developed by using lead sulfide (PbS) which is sensitive to wavelength up to $\sim 3\mu m$. In 1940- 1950, new materials like Lead Selenide (PbSe), lead telluride (PbTe), and Indium Antimonide (InSb) were developed which increased the sensitivity in the medium wavelength, $3 - 5\mu m$. In the mid-1960, commercial infrared camera was developed and had a great influence on infrared thermography testing applications [7].

2.3.3 Infrared Fundamentals

Radiation

Thermal radiation is an electromagnetic radiation which is emitted from matter and is measured by its temperature. Thermal radiation is emitted at the speed of light, 3×10^8 m/sec [21]. This speed is equal to the product of the wavelength and frequency of a radiation

$$c = \lambda\nu \tag{2.1}$$

where c is the speed of light, λ is the wavelength and ν is the frequency [21]. Thermal radiation is associated with a temperature range of approximately 30 to 30,000K and

wavelength range of 0.1 to 100μm [46]. Electromagnetic radiation is classified based on the wavelength. X-ray, gamma ray, infrared waves and microwave are some of the forms based on such classification. Figure 2.4 shows the electromagnetic spectrum [13]. Infrared is also subdivided into three ranges based on their bandwidth; near infrared $0.78-3\mu m$, mid infrared $(3-50\mu m)$ and far infrared $(50-1000\mu m)$. They are invisible.

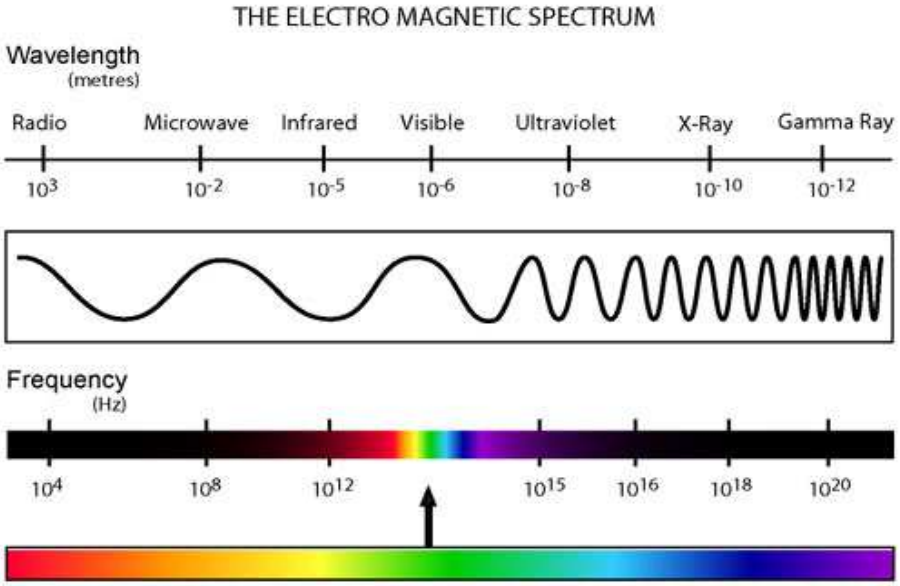

Figure 2.4: Electromagnetic spectrum [13]

Matter emits electromagnetic radiation at a given temperature in discrete energy quanta called photons [46]. By modeling each quantum as a particle with mass m, the energy E associated with one particle is

$$E = h\nu = mc^2 \tag{2.2}$$

where h is the Plank's constant with the value of 6.625×10^{-34} $J.sec.$ Equation (2.2) is for one particle; to calculate the total energy emitted, the energy density is integrated over all wavelength to obtain the Stefan-Boltzman law

$$E_b = \sigma T^4 \tag{2.3}$$

where E_b is the energy radiated per unit time and per unit area, and σ is the Stefan-Boltzman constant with the value $5.669 \times 10^{-8}\mathrm{W/m^2K^4}$.

Temperature difference between two surfaces corresponds to energy exchange by radiation. From (2.4) one can obtain the net radiant exchange between a convex surface at temperature T_1 and a large encloser at temperature T_2

$$q = \sigma A_1 \epsilon_1 \left(T_1^4 - T_2^4\right) \tag{2.4}$$

where A_1 and ϵ_1 are the area and the emissivity of convex surface, respectively.

Blackbody and graybody

In radiation theory material bodies are categorized in to two groups, namely *blackbody* and *graybody*. Radiation properties of material bodies are the reason for this categorizing. The balance of energy exchange by radiation between body surfaces is described by these radiation properties in the following equation, visualized in figure 2.5:

$$\rho + \alpha + \tau = 1 \tag{2.5}$$

where ρ is the reflectivity, α is the absorptivity and τ is the transmissivity. These parameters are radiation properties and depend on the material [21].

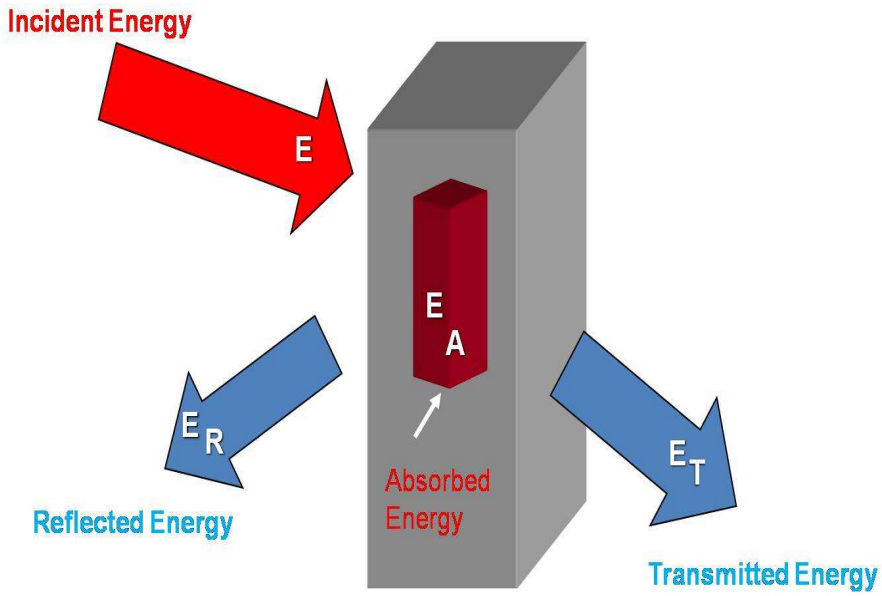

Figure 2.5: Sketch showing incident energy(pics from google)

Blackbodies are characterized by $\rho = 0$, which means that no radiation is reflected. This characteristic results into the black color [21]. Another characteristics of blackbody

is that at a given wavelength it emits more energy than any other material body [7] and also it absorbs all electromagnetic radiation.

Any material with $\rho \neq 0$ is considered a graybody.

2.3.4 Approaches in infrared thermography

The two main approaches in experimental infrared thermography are called Active thermography and Passive Thermography.

Active thermography

Active thermography is based on the use of an external heat source to stimulate a target by heating or cooling to detect flaws inside it [47]. Active thermography can be performed in different forms such as pulse thermography, lock-in thermography, and pulse phase thermography and by a combination of different forms in non-destructive testing like lock-in thermography with ultrasound or eddy current. Each one has been developed for a specific need in their field of applications.

Pulsed thermography

Integrated systems for active thermography, commonly known as pulsed thermography or thermal wave imaging systems, are becoming increasingly popular for non-destructive evaluation [48]. In this method, a short duration of heat pulse is used to stimulate the testing object and responses are processed in transient state [25]. Thermal distribution after a given time shows defective and non-defective regions related to the depth of the defects [25]. The setup is shown in figure 2.6.

Photographic flashes, lamps, laser beam and heat gun [31] are some of the sources which are used in pulse thermography. These sources produce high surface temperature [55]and the duration of excitation is chosen based on the thermal property of object and flaws which can vary from few milliseconds ($2 - 15msec$) to several seconds [25]. The advantages of this methods are that they are fast and easy to use, but data may be affected by non-uniform heating and local variation of thermal emission [5].

Lock-in thermography

In lock-in thermography a sinusoidal thermal wave is applied to a tested object to detect flaws, disbond or any imperfection, see figure 2.7. Information about the size and position

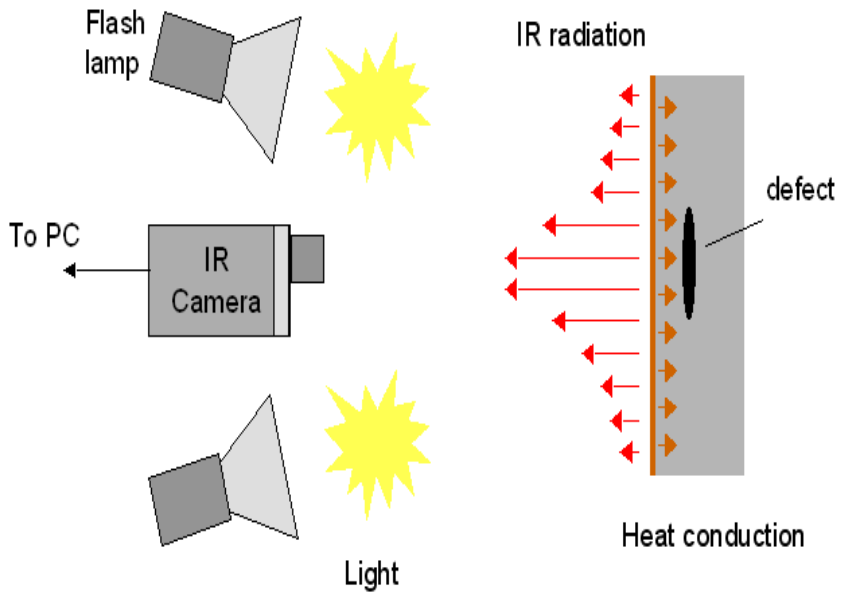

Figure 2.6: Set-up for pulse thermography [40]

of the defects can be revealed by processing of the captured images. The excitation is imposed by a lamp emitting at the frequency ω until a steady state is achieved [25]. Since a thermal wave is used the characteristics of the wave like amplitude and phase can be applied for fault detection. Amplitude and phase of thermal wave change after passing any internal defects. Disbond or any defects can be revealed by phase shift [25].Lock-in thermography is a faster version of photothermal radiometry. Photothermal radiometry is a method for remote measurement of local harmonic method that has sensitive phase angle to subsurface defects [55]. Lock-in thermography gives good information about size, depth and thermal resistance without post-processing procedures. As opposed to pulse thermography, it is not sensitive to non-uniform heating and local emissivity coefficient. Although, one of the disadvantages is the difficulty of detection of deeper small defects since sufficiently low excitation frequencies are difficult to produce [5].

Lock-in thermography can be combined with other non-destructive testing methods such as ultrasound and eddy current. The combination makes the detection simpler and faster. In ultrasound lock-in thermography, loss angle is used which is part of the elastic energy and it is irreversibly converted to heat [55]. The basic idea is that each defect has specific properties that can be detected under certain conditions [56]. This method is more effective in area of stress concentration, cracks and delamination [55, 33]. This wave makes these areas act as internal heat sources that reach to the surface of testing

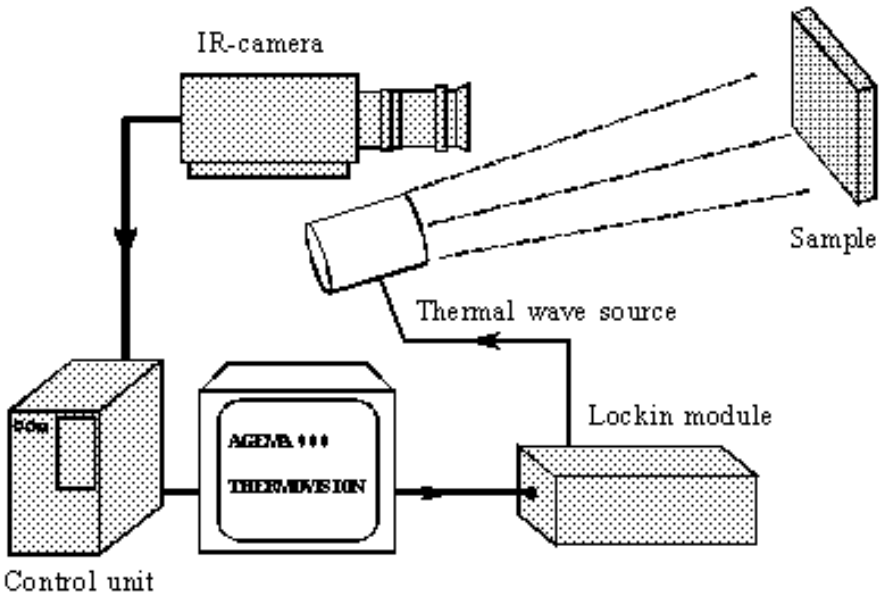

Figure 2.7: Set-up for Lock-in thermography (from [56]

object which can be detected by lock-in thermography system. Imaging is based on the phase shift. After the internal generated heat source reaches to the surface, the phase image shows the distance that wave has traveled. Therefore, such image displays the defects depth.

Pulse Phase thermography

Pulse phase thermography is an approach in infrared thermography application which was introduced as a signal processing technique [5, 31]. Pulse phase thermography, developed by Maldague and Marinetti, is a combination of pulse and lock-in thermography in which tested objects are exposed to a periodic excitation [5]. In pulse phase thermography the surface of the testing object is excited by a rectangular pulse and the result is represented in terms of phase or amplitude images. Using this method, deeper defects can be detected in comparison with lock-in thermography, but to reach this result, certain temperature differences between each image sequence is needed.

It is found that, in the cooling phase, defects are much more visible than the heating phase [5]. Tested object are submitted to a heating source and immediately after the surface temperature reaches to 2, 7, or 15 °C above the ambient temperature, the heating source shuts down. Then the imaging process stars. To find the defects deeper in the material, a higher surface temperature is required. This makes pulse phase thermography

an appropriate technique but only when the surface is insensible to temperature. It makes a limitation for pulse phase thermography because the surface temperature cannot be as low as lock-in thermography [5].

Passive thermography

In passive thermography no external sources are used. The method is based on natural temperature differences between the surrounding environment and the tested object [15]. Passive thermography is not an appropriate method to detect a defect in a deeper layer because it cannot make a high temperature contrast over the defect and non-defect areas [15]. In civil engineering, passive thermography is used to inspect structures like bridge decks [7]. One of the reasons is that construction materials like concrete have a specific thermal characteristic. Usually they have a low thermal conductivity but high specific heat that causes them to reach balance with surrounding environment in a longer time [7]. This longer time corresponds to enough temperature contrast to be captured.

2.3.5 Modeling in infrarerd thermography

Bison et al. proposed an algorithm to detect and evaluate the characteristics of the defects in the back side of a thin metallic plate [43]. The purpose of this algorithm is to detect a damage as small as possible in real time [43]. The algorithm is based on the mathematical tool Domain Derivative, which is used for real time linearization of the nonlinear inverse problem [43]. One side of the specimen is inside the laboratory and heated by a lamp with a constant heat flux and the other side is in contact with the outside. Convection boundary condition is also considered for the outside surface. Defects are modeled as loss of an amount of matter at the back side of the plate, so the back side is no longer a plane. The heat flux is assumed to be constant in space. The algorithm allows for the detection of the position of the damage [43].

In infrared thermography several factors influence the thermographic signal received by the infrared camera. Some of these factors are thermal conductivity; heat capacity; defect depth as internal factors and convection heat transfer; variation on surface emissivity and ambient radiation reflectivity as external factors [29].Each of these has its own effects and Lopez et al. tried to determine them quantitatively [29]. Modeling is based on the physics of non-destructive testing by infrared thermography. Physical effects included are transient, three dimensional heat conduction equations and convection and radiation as boundary conditions. Finite Volume Method is used to obtain an

approximation of the heat equation. The model is analyzed during a cool down process. The sensitivity analysis obtains from the Sensitivity Matrix or Jacobian:

$$J(P) = \left[\frac{\partial T^T}{\partial P}(P)\right] \tag{2.6}$$

where J_{ij} is the sensitivity coefficient, and estimated temperature T_i is measured with respect to perturbation in the parameter P_i, depth, thermal conductivity, and heat capacity [42].

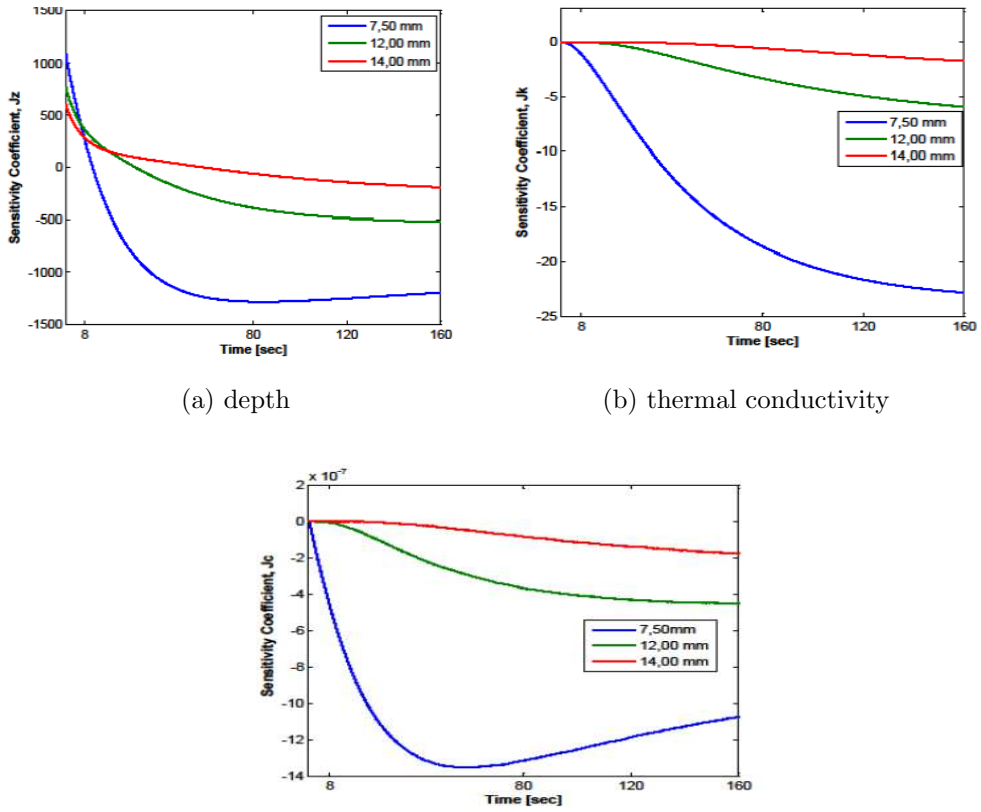

(a) depth

(b) thermal conductivity

(c) heat capacity

Figure 2.8: Sensitivity coefficient for defects at different depth considering properties (a)depth, (b)thermal conductivity and(c) heat capacity [29].

As the results show in figure 2.8 depth has more effect on temperature than thermal conductivity and heat capacity [29].

In experimental non-destructive testing, frequency of excitation is one of the important parameters. By choosing a correct excitation frequency, the location and charac-

teristics of defects can be detected. For example, smaller frequency of excitation leads to deeper penetration in the tested object [15]. Necsulescu et al. derived an equation to predetermine a frequency of excitation given the defect size and the first time that steady state values can be recorded [38].

The heat conduction equation is used in a semi-infinite domain with the cosinusoidal excitation at $u(0,t) = U\cos(\omega t - \epsilon)$. After a characteristic time, the transient part of the excitation vanishes and only the steady state remains. This time is called settling time and it is given by

$$t_{2\%}(x) = \frac{1}{k\pi}\left(\frac{x}{.02e^{-x\sqrt{\frac{\omega}{2\alpha}}}}\right)^2 \tag{2.7}$$

According to equation (2.7), a lower frequency is needed to have a shorter transient time. To detect a defect, the amplitude of thermal waves must be large enough at the position of the defect, x. For a semi-infinite domain the following closed form relation for the frequency of excitation as a function of the temperature amplitude and the point x is derived in [38]

$$\omega = \frac{2k}{x^2}\left[\ln\left|u_{ss}(x,t)\right|\right]^2 \tag{2.8}$$

where k is the diffusivity, x is the observation point, and $u_{ss}(x,t)$ is the temperature at observation point. As the (2.8) shows, the temperature at observation point decays exponentially with the increase of the distance x which implies that for a deeper defects the lower frequency is required. After the excitation, the thermal wave propagates inside the objects and it is reflected at the boundary. The composition of the thermal wave and the reflected thermal wave is more complex to be analyzed in non-destructive testing. In this regard, the first reflection time is derived and given by

$$\Delta t = \frac{m}{V} = \frac{m}{\sqrt{2k\omega}} \tag{2.9}$$

where m is the mass and V is the velocity.

G. Gralewicz et al. [17] studied a defect detection in composite and single and multi-layer materials by using dynamic thermography. Composite materials are made from two or more materials or components which have different material properties and characteristic. Carbon fiber reinforced composites is one of the composite material which because of its constitutive properties, low weight with high strength, is widely used in civilian, military, and aircraft [2] [17]. Presence of any imperfections such as ply

separation and air bubbles in composite materials strongly affect the quality of their properties. These imperfections may threaten the human's life, in aerospace for example. A thin film of carbon-fiber-reinforced polymer was considered. The upper side of the film is exposed to periodic heat flux and convective boundary condition is applied to upper and bottom side. An analytical solution for single and multilayer materials was obtained. In multilayer material, the interface is characterized by its thermal resistance. Phase difference for the temperature between the homogenous material and the place where the defect is, is computed for fault detection. It was shown that lock-in thermography is a very effective in evaluating single and multi-layer materials for non-destructive testing.

V. Feuillet et al. used active thermography to detect defects and their characteristics in composite materials, carbon/epoxy composite plate, [11]. They used the long pulse excitation for experimental setup with singular value decomposition analysis and quadrupole method for analytical one-dimensional transient thermal model. In they approach, front face and back face are observed. The characterization of thermo-physical properties can be obtained from the rear face (sound part of the plate), and from the front face thermal resistance and depth of the defect can be identified. In their research, four sets of composite plates were used. In the analytical modeling, they applied a known resistance R as defect between the plies. The specimen is excited by a uniform heat flux on the front face under different heating durations $(0.5, 1, 2, 5sec)$, and also the plate is submitted to convective boundary conditions both on rear and front faces. The thermal quadrupole method gives the temperature-heat flux density spectra on both faces. Singular value decomposition is used in inverse procedure to detect sound and defect areas. According to the result of singular value decomposition analysis, increasing heating duration reduces the influence of measurement noise. In addition, active infrared thermography coupled with singular value decomposition analysis and thermal quadrupole modeling is a good method to characterizing different defects in carbon/epoxy composite samples [11].

G. Gralewicz et al. suggested a new thermal model and simulation for detecting a defect in composite materials [18]. They simulate the lock-in thermography in ANSYS software and the obtained data is processed in MATLAB to locate the inclusion and decrements in the composite materials. One face is subjected to sinusoidal excitation while all the faces subjected to convection boundary condition. A cylindrical inclusion with a radius $r = 0.005m$ and depth $d = 0.0005m$ is introduced for this simulation, (the defect is very small in comparison with the dimensions of the plate). ANSYS analysis shows that the defect does not have a significant influence on the temperature close to

it.

Detection of a defect thermal properties, size, and position in a composite material is studied in [52] by using lock-in and pulse thermography. Analytical solution is obtained for single and multi-layer materials for two different excitations' periodic and impulse. A thermal contrast between the region close to the defect and the homogenous region is introduced in order to detect a defect. This contrast depends on the defect depth and it is measured during the cooling down process. To detect a defect in solid material, the defect is modeled with a low thermal conductivity. To obtain the location of the imperfection in the solid material, the model is excited by an energy pulse. Then, the temperature difference is measured between the defect locations and where the homogenous material is. To measure the thickness of a specimen, several thermal images are captured and temperature variation in each sequence is studied. Since temperature variation changes with time, it can be effectively used to measure the thickness. The effect of infrared reflection, non-stable ambient conditions, and undefined convective heat transfer coefficient on the accuracy of these measurements were also investigated [52]. These elements significantly reduce the accuracy of thermography results.

Almond et al. derived an analytical solution for defect sizing detection by transient thermography [1]. Transient thermography or pulsed video thermography was developed for the first time by Milne and Reynolds [37], [1]. Almond and Lau derived the analytical solution to explain the image formation process. In their approach they modeled a disc air gap as a defect at a specific depth of the tested object. An intense optical flash is used for excitation with a very short duration (milliseconds). This duration is enough to apply a uniform heat flux to the object which is blocked by the air gap. This air gap reduces the thermal gradient over the defect which makes a thermal contrast, which is captured by the infrared camera, on the surface between the area over the defect and its hotter surrounding area. The resulting temperature gradient generates heat flow around the edge of the crack from the hotter to the cooler area. To have a better and more clear image, Green functions are used to determine the lateral extent of a defect image and its apparent size [1]. Green functions give a thermal contrast at each point on the surface. This study was applied to straight-edge and circular crack. Results show the essential role of heat flow around the crack for edge detection of the crack [1].

2.3.6 Heat Transfer Fundamental

Heat transfer takes place in three different classes; conduction, convection and radiation.

Conduction

Conduction is associated with the gradient of temperature inside the body, the energy transfers from high-temperature region to low-temperature region. In conduction, the heat transfer per unit area is proportional to the normal temperature gradient:

$$q_x = -Ak\frac{\partial T}{\partial x} \tag{2.10}$$

where q_x is the heat flux in x direction , k thermal conductivity, A is the cross section area, the minus sign indicates that heat is transferred in the direction of decreasing temperature (to satisfy thermodynamic second law). This equation is generally known as Fourier's law of heat conduction [21].

Convection

Convection is an important class in heat transfer that takes place in fluids. It is intrinsically associated to bulk current flow and diffusion which cannot occur in solids. Gradient temperature causes the heat transfer from high-temperature to the low- temperature region and in fluids it affects the density. This induces currents in the fluid and consequent heat transfer associated to mass transport. The rate of heat transfer between the wall and fluid is related to the velocity of the fluid. High velocity produces a large temperature gradient [21]. Newton's law of cooling expresses the overall effect of convection [21]

$$q_x = \mu A\left(T_w - T_\infty\right) \tag{2.11}$$

where μ is the convection heat-transfer coefficient, A is the cross-section area and $(T_w - T_\infty)$ is the temperature difference between the wall and the fluid. μ is also called film conductance because of the relation of conduction of the thin layer of fluid and the wall surface [21].

Radiation

The fundamental relation between the radiating heat flux and the temperature has been discussed in in section 2.3.3.

Chapter 3

Governing equations

3.1 Heat conduction in a multi-layer slab

We consider a multi-layer slab-like domain, see figure 3.1 which is a three dimensional continuum with two sides very large with respect to thickness so that the effect of the edges can be neglected. It is therefore appropriate to introduce a reduced one-dimensional approximation along the spatial coordinate $x \in [0, l]$ of the initial boundary values problem governing the heat conduction. Moreover, we assume that the lateral surface has no heat loss and that there is no internal heat source, F, and formulate the one-dimensional initial-boundary value heat conduction problem as[19]

$$\frac{\partial T_i}{\partial t} = \alpha_i \frac{\partial^2 T_i}{\partial x^2} + F \tag{3.1a}$$

$$T_1(0, t) = T_\infty + U \sin(\omega t) \tag{3.1b}$$

$$T_i(a_i, t) = T_{i+1}(a_i, t) \tag{3.1c}$$

$$k_i \frac{\partial T_i(a_i, t)}{\partial x} = k_{i+1} \frac{\partial T_{i+1}(a_i, t)}{\partial x} \tag{3.1d}$$

$$k_n \frac{\partial T_n}{\partial x}(l, t) = -\mu \left(T_n(l, t) - T_\infty\right) \tag{3.1e}$$

$$T_i(x, 0) = T_\infty \tag{3.1f}$$

where T_i is the temperatures in the $i-th$ layer at point $(x, t) \in \mathbb{R} \times \mathbb{R}$, $a_1, a_2, ..., a_{n-1}$ are the coordinate of the material interfaces in the slab that are assumed to be parallel to the sides at $x = 0$ and $x = l$, and constants α_i and k_i represent respectively the thermal diffusivity and the thermal conductivity of the materials. We consider $a_1 = 0$ and $a_n = l$.

The slab is assumed to be initially a the ambient temperature,T_∞, consistently with the initial condition(3.1f). At time zero a persistent oscillating perturbation of amplitude U and radian frequency ω is added at $x = 0$, as formalized by the boundary condition (3.1b). Equation (3.1e) is a convective boundary condition with themal coefficient of μ describing the experimental condition that we want to reproduce. We assume no internal heat source therefore setting $F = 0$.

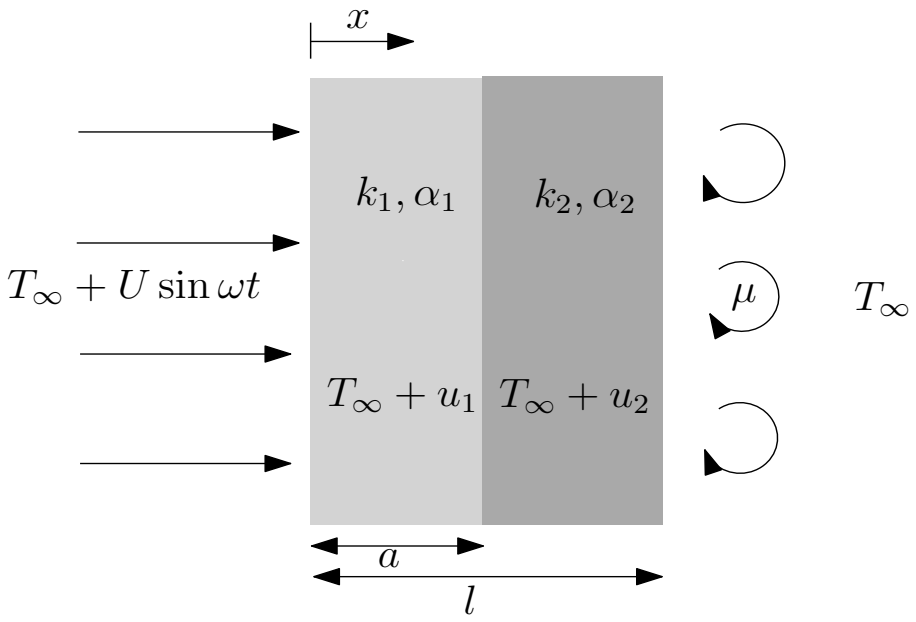

Figure 3.1: Two layer model with sinusoidal excitation in front face and convection at rear face

According to boundary condition (3.1b), there is an oscillation around ambient temperature T_∞. By introducing the $u_i(x,t) = T_i(x,t) - T_\infty$, we obtain the following set of equations

$$\frac{\partial u_i}{\partial t} = \alpha_i \frac{\partial^2 u_i}{\partial x^2}, i = 1, 2, ..., n \tag{3.2a}$$

$$u_1(0, t) = U \sin(\omega t) \tag{3.2b}$$

$$u_i(a_i, t) = u_{i+1}(a_i, t) \tag{3.2c}$$

$$k_i \frac{\partial u_i(a_i, t)}{\partial x} = k_{i+1} \frac{\partial u_{i+1}(a_i, t)}{\partial x}, i = 1, 2, ..., n \tag{3.2d}$$

$$k_n \frac{\partial u_n}{\partial x}(l, t) = -\mu u_n(l, t) \tag{3.2e}$$

$$u_i(x, 0) = 0 \tag{3.2f}$$

For any ambient temperature $T_\infty \neq 0$, the resulting temperature can be calculated as $T_\infty + u_i$.

By introducing the non-dimensional variables, $x^* = x/l$, $t^* = t\omega$, $u^* = u/U$, we rewrite the initial-boundary value problem (3.2) in non-dimensional form

$$\frac{\partial u_i^*}{\partial t^*} = \frac{1}{\beta_i} \frac{\partial^2 u_i^*}{\partial x^{*2}}, \quad i = 1, 2, ..., n \tag{3.3a}$$

$$u_1^*(0, t) = \sin t^* \tag{3.3b}$$

$$u_i^*(a_i, t) = u_{i+1}^*(a_i, t) \tag{3.3c}$$

$$\varrho_i \frac{\partial u_i^*(a_i, t)}{\partial x^*} = \varrho_{i+1} \frac{\partial u_{i+1}^*(a_i, t)}{\partial x^*} \tag{3.3d}$$

$$\varrho_n \frac{\partial u_n^*}{\partial x^*}(1, t) + \sigma u_n^*(1, t) = 0 \tag{3.3e}$$

$$u_i^*(x, 0) = 0 \tag{3.3f}$$

where the nondimensional parameters are defined by

$$\varrho_i = \frac{k_i}{k_1}, \quad \beta_i = \frac{\omega l^2}{\alpha_i}, \quad \sigma = \frac{\mu l}{k_1} \tag{3.4}$$

with $\varrho_1 = 1$. Therefore the system of equations (3.3) depends on $n + (n - 1) + 1 = 2n$ nondimensional parameters. Unless otherwise stated, in the remaining part of the thesis we will drop the superscript star and refer to non-dimensional variables by using the same symbol as the corresponding dimensional ones.

3.1.1 Thermal Quadrupole Method

A thermal quadrupole is a two-port network that can be used to obtained a lumped parameters representation of the system [30]. The temperature and heat flux are respec-

tively the across and the through network variables. The structure of the one dimensional initial-boundary value problem allows for the input to output representation of the system [30] in terms of temperature and heat flux at two points in the spatial domain, mapped by a linear transformation that is the transfer function defined by thermal quadrupoles.

Quadrupole derivation

We consider the one side Laplace transform of equation (3.3a)

$$\frac{d^2U_i}{dx^2} = s\beta_i U_i \tag{3.5}$$

where s is the Laplace parameter and $U_i(s)$ is the Laplace transform of temperature. The general solution of this ordinary differential equation is

$$U_i(s,x) = c_1^i \cosh\left(x\sqrt{\beta_i s}\right) + c_2^i \sinh\left(x\sqrt{\beta_i s}\right) \tag{3.6}$$

where constants c_1^i and c_2^i are determined by the boundary conditions (3.3b) and (3.3c).

The Laplace transform of the heat flux is related to the temperature by Fourier law

$$Q_i(s,x) = -\varrho_i \frac{dU_i}{dx}(s,x) = -\varrho_i\sqrt{\beta_i s}\left(c_1^i \cosh(x\sqrt{\beta_i s}) + c_2^i \sinh(x\sqrt{\beta_i s})\right) \tag{3.7}$$

Since the temperature and the heat flux are linearly related, we can represent the input to output relationships between two interfaces, say a_{i-1} and a_i,

$$U_{i-1}(a_{i-1},s) = A_i U_i(a_i,s) + B_i Q_i(a_i,s) \tag{3.8a}$$
$$Q_{i-1}(a_{i-1},s) = C_i U_i(a_i,s) + D_i Q_i(a_i,s) \tag{3.8b}$$

In the following we will drop the spatial argument of the functions appearing in equation (3.8) and uniquely identify the interface at which they are evaluated with the subscript. For example U_1 and U_2 are the temperatures at the front and at the first interface respectively. By imposing the continuity of the temperature and heat flux at the interfaces through equations (3.3b) and (3.3c) we determine the constants in equation (3.7) and we can represent the above linear system as

$$U_{i-1} = \cosh((a_i - a_{i-1})\sqrt{\beta_i s})U_i + \frac{1}{\varrho_i\sqrt{\beta_i s}}\sinh((a_i - a_{i-1})\sqrt{\beta_i s})Q_i \tag{3.9a}$$
$$Q_{i-1} = \varrho_i\sqrt{\beta_i s}\sinh((a_i - a_{i-1})\sqrt{\beta_i s})U_i + \cosh((a_i - a_{i-1})\sqrt{\beta_i s})Q_i$$

in matrix form

$$\begin{bmatrix} U_{i-1}(s) \\ Q_{i-1}(s) \end{bmatrix} = M_{i-1}^{i} \begin{bmatrix} U_i(s) \\ Q_i(s) \end{bmatrix} \tag{3.10}$$

Specifically, for the system (3.3) the thermal quadrupoles representation is given in figure 3.2, with matrix M_{i-1}^{i} given by

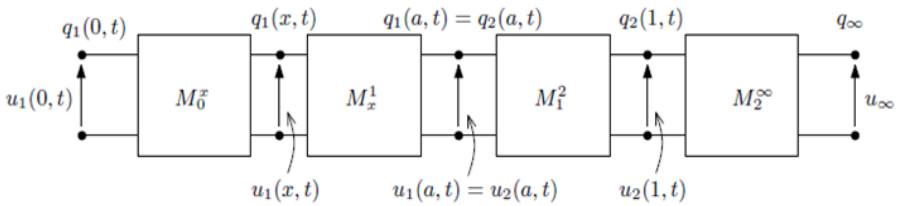

Figure 3.2: For a two layers slab, lumped parameters representation of the linear system (3.10) via thermal quadrupoles, with an observation point x located within layer 1. The case with observation point located in layer 2 can be easily obtained.

$$M_{i-1}^{i} = \begin{pmatrix} A_i & B_i \\ C_i & D_i \end{pmatrix}, i = 1, 2, ..., n \tag{3.11a}$$

$$A_i = D_i = \cosh\left((a_i - a_{i-1})\sqrt{\delta_i \beta_1 s}\right) \tag{3.11b}$$

$$B_i = \frac{1}{\varrho_i \sqrt{\delta_i \beta_1 s}} \sinh\left((a_i - a_{i-1})\sqrt{\delta_i \beta_1 s}\right) \tag{3.11c}$$

$$C_i = \varrho_i \sqrt{\delta_i \beta_1 s} \sinh\left((a_i - a_{i-1})\sqrt{\delta i \beta_1 s}\right) \tag{3.11d}$$

whereM_{i-1}^{i} is the transition matrix for the $i-th$ layer that is used to represent the input to output behavior of an homogeneous layer of thickness $a_i - a_{i-1}$, and $\delta_i = \beta_i/\beta_1 = \alpha_1/\alpha_i$.

The transition matrices M_{i-1}^{x} and M_i^x are defined analogously by substituting a_i and a_{i-1} with x respectively. The transition matrix M_n^∞ which accounts for the convective boundary condition is given by

$$M_n^\infty = \begin{pmatrix} 1 & \frac{\varrho_n}{\sigma} \\ 0 & 1 \end{pmatrix} \tag{3.12}$$

Consistently with the formulation of the problem (3.3) we have $U_\infty = 0$.

The non-dimensional lumped parameters representation in (3.11) implies that the transfer function depends on the excitation frequency ω through β_1. In other words, the parameter β_1 is the non-dimensional equivalent of ω.

The input to output relation between the lumped variables U_1 and U_x that is the temperature at the observation point x located in the $i-th$ layer with respect to the input U_1 is obtained by solving the following system associated to the thermal quadrupoles representation

$$\begin{pmatrix} U_1 & Q_1 \end{pmatrix}^{\mathsf{T}} = M_0^1 M_1^2 M_2^3 ... M_{i-1}^x \begin{pmatrix} U_x & Q_x \end{pmatrix}^{\mathsf{T}} \tag{3.13a}$$

$$\begin{pmatrix} U_x & Q_x \end{pmatrix}^{\mathsf{T}} = M_x^i M_i^{i+1} ... M_{n-1}^n M_n^\infty \begin{pmatrix} U_\infty & Q_\infty \end{pmatrix}^{\mathsf{T}} \tag{3.13b}$$

with $U_\infty = 0$. The relation between U_x and U_1 can be found by solving equation (3.13) for Q_x and Q_∞. Substitution into (3.13a) gives the relation between U_1 and U_x. The solution is in general represented by the following input to output relation

$$\frac{U_x(s)}{U_1(s)} =: G(s) \tag{3.14}$$

In the following we will specialize the transfer function $G(s)$ for different scenarios.

Chapter 4

Approximate closed form solution for damage detection in multi-layer materials

4.1 Introduction

Composite and multi-layer materials are high demand in different fields such as aerospace, ballistic applications, civil engineering, automobile and engineering structure [18], [24], [27], [51]. This class of material is widely used in several critical applications that also involve human life and safety which leads to the need of increasing their safety and reliability of inspection from manufacturing to in-service process.

The inspection becomes more challenging for composite and multi-layer material especially in the field of aerospace [23]. Any defect in multilayer material or composite such as ply separation, air bubbles and delaminating can lead to the modification of their properties [1], which can effect reliability and safety. Detecting a characteristic of a possible defect in a shorter time and easier way are two notable benefits of infrared thermography [45].

The goal of this chapter is to investigate the method for designing efficient infrared non-destructive testing experiments for detecting defects in composite and multi-layer materials. For this purpose, an important issue is to derive new formulas to predetermine the frequency of excitation in design of non-destructive tests [39]. Inverse heat conduction in a multi-layer material slab with periodic temperature excitation is considered. We use the analytical quadrupoles representation to derive a lumped parameters

formulation of the problem that allows for an input-output representation in terms of a transfer function in the Laplace domain. The generally transcendental transfer function is approximated with the corresponding power series, which allows for a polynomial implicit approximated solution of the inverse problem. In addition, the mentioned approach is used to obtain a relation between the frequency of excitation and temperature at observation point for the case that an inclusion models eventual air bubbles among layers or inside the material body. We also consider layer detachments by introducing the appropriate thermal resistance in the lumped model.

Material in the section 4.2 is accepted for publication in the coming QIRT2012 conferences in June $11 - 14$ [10]

4.2 Approximate solution of the inverse problem

Equation (3.14) gives a general relation between normalized temperature U_x/U_1 at the observation point x and the non-dimensional excitation frequency β_1. A closed form solution of the inverse problem, that is a closed form relation between β_1 and U_x cannot be found. Therefore, we approximate the transfer function $G(s)$ by a power series expansion with respect to $\beta_1 s$, and asses the accuracy of the approximation for different truncation orders. The accuracy of approximation in increase by choosing the higher value for N. However, very high value of N makes the approximation more complex, therefore the value should be chosen large enough to have enough accuracy as well as avoiding complexity. Specifically, $G(s)$ is approximated by

$$G(s) \sim G_{\mathrm{a}}(s) = \frac{1}{\sum_{k=0}^{N} b_k (\beta_1 s)^k} =: \frac{1}{p_N(\beta_1 s)} \tag{4.1}$$

where coefficients b_k are given by

$$b_k = \frac{1}{k!} \frac{\partial^k}{\left(\partial(\beta_1 s)\right)^k} \left(\frac{1}{G(s)} \right) \Bigg|_{\beta_1 s = 0} \tag{4.2}$$

The choice in equation (4.1) is not unique. We choose this particular form so that the approximated transfer function is a proper rational function and therefore we can apply the techniques below as long as the roots of the characteristic polynomial, that is the denominator of the approximated transfer function, are stable. The approximated input to output relationship

$$\frac{U_x}{U_1} = G_{\mathrm{a}}(s) = \frac{1}{p_N(\beta_1 s)} \tag{4.3}$$

allows to find an implicit solution of the inverse problem whenever the polynomial $p_N(\beta_1 s)$ is stable, that is whenever the roots have negative real part.

For a linear scalar system with transfer function $G_{\mathrm{a}}(s)$ the response to the sinusoidal input $u_1(0,t) = \sin \omega t$ is given by $u_2(x,t) = |G_{\mathrm{a}}(\jmath\omega)| \sin(\omega t + \varphi)$, see for example[41], where $|G_{\mathrm{a}}(\jmath\omega)|$ and φ are respectively the amplitude and the phase of the transfer function

$$|G_{\mathrm{a}}(\jmath\omega)|^2 = \Re\left(G_{\mathrm{a}}(\jmath\omega)\right)^2 + \Im\left(G_{\mathrm{a}}(\jmath\omega)\right)^2 \tag{4.4}$$

$$\tan\varphi = \frac{\Im\left(G_{\mathrm{a}}(\jmath\omega)\right)}{\Re\left(G_{\mathrm{a}}(\jmath\omega)\right)} \tag{4.5}$$

where the operators $\Re$ and $\Im$ represent respectively the real and the imaginary part of their argument, and $\jmath = \sqrt{-1}$. Therefore the amplitude of the temperature u_x at the observation point located at the non-dimensional abscissa x can be related to the non-dimensional excitation frequency β_1 by

$$\Re\left(p_N(\jmath\beta_1)\right)^2 + \Im\left(p_N(\jmath\beta_1)\right)^2 = \frac{1}{|u_x|^2} \tag{4.6}$$

For $N = 1$, $N = 2$,and $N = 3$ the explicit forms of (4.6) are respectively given by

$$b_0^2 - \frac{1}{|u_x|^2} + b_1^2\beta_1^2 = 0, \tag{4.7a}$$

$$b_0^2 - \frac{1}{|u_x|^2} + (b_1^2 - 2b_0b_2)\beta_1^2 + b_2^2\beta_1^4 = 0, \tag{4.7b}$$

$$b_0^2 - \frac{1}{|u_x|^2} + (b_1^2 - 2b_0b_2)\beta_1^2 + \left(b_2^2 - 2b_1b_3\right)\beta_1^4 + b_3^2\beta_1^6 = 0, \tag{4.7c}$$

The bi-quadratic structure of the expressions allows for the explicit solution to be found by using the formula for the roots of quadratic and cubic polynomials. Among the multiple roots, one must select the one such that β_1 is real and non-negative. We note that the implicit solution in (4.6) applies to multilayer systems provided that coefficients b_k are obtained for the specific materials and geometry. For a generic order N the implicit polynomial relation can be written as

$$b_0^2 + b_N^2\beta_1^{2N} + \sum_{k=1}^{N-1}(b_k^2 - 2b_{k-1}b_{k+1})\beta_1^{2J} - \frac{1}{|u_x|^2} = 0 \tag{4.8}$$

The solution for $N = 2$ is

$$\beta_1^2 = \frac{2b_0b_2 - b_1^2 \pm \frac{1}{|u_x|}\sqrt{|u_x|^2 b_1^2(b_1^2 - 2b_0b_2) + 4b_2^2}}{2b_2^2} \tag{4.9}$$

In order to have $\beta_1^2 > 0$ for $|u_x| \to 0$ (β_1 would otherwise be complex, and so would be the frequency of excitation ω) we must select the solution

$$\beta_1^2 = \frac{2b_0b_2 - b_1^2 + \frac{1}{|u_x|}\sqrt{|u_x|^2 b_1^2(b_1^2 - 2b_0b_2) + 4b_2^2}}{2b_2^2} \tag{4.10}$$

which gives

$$\beta_1 = \sqrt{\frac{2b_0b_2 - b_1^2 \pm \frac{1}{|u_x|}\sqrt{|u_x|^2 b_1^2(b_1^2 - 2b_0b_2) + 4b_2^2}}{2b_2^2}} \tag{4.11}$$

The approximate solution in (4.11) holds provided that the argument of the radical is positive. For $N = 1$ we obtain the very simple formula

$$\beta_1 = \frac{1}{b_1}\sqrt{\frac{1}{|u_x|^2} - b_0^2} \tag{4.12}$$

In the following sections we give expression for coefficients b_k corresponding to different scenarios. Coefficients are obtained with *Mathematica*©

4.2.1 Homogeneous slab

A homogeneous slab is characterized by $n = 1$ in equation (3.13) with the observation point x placed in the single layer. The transfer function is

$$\frac{U_x(s)}{U_1(s)} = \frac{\sqrt{\beta_1 s}\cosh(1-x)\sqrt{\beta_1 s} + \sigma\sinh(1-x)\sqrt{\beta_1 s}}{\sqrt{\beta_1 s}\cosh(\sqrt{\beta_1 s}) + \sigma\sinh(\sqrt{\beta_1 s})} \tag{4.13}$$

The first three coefficients that define the approximate transfer function G_a (for $N = 2$, that is second order truncation) are

$$b_0 = \frac{1+\sigma}{1+\sigma(1-x)} \tag{4.14}$$

$$b_1 = \frac{x}{6(1+\sigma(1-x))^3}\left(\sigma(\sigma+1)x^2 - 3(\sigma+1)^2x + 2(\sigma(\sigma+3)+3)\right) \tag{4.15}$$

$$\begin{aligned} b_2 = {} & \frac{x}{360(1+\sigma(1-x))^3} \\ & \Big(7\sigma^2(\sigma+1)x^5 - 42\sigma(\sigma+1)^2x^4 + 5\left(19\sigma(\sigma(\sigma+3)+3)+15\right)x^3 \\ & - 100(\sigma+1)(\sigma(\sigma+3)+3)x^2 + 24(2\sigma(\sigma(\sigma+5)+10)+15)x \\ & - 8(\sigma(\sigma(\sigma+6)+15)+15)\Big) \end{aligned} \tag{4.16}$$

For $x = 1$ and $\sigma = 0.08$ the plots of β_1 versus $|G_a(\jmath\beta_1)| = |u_x|/U$ are shown in figure 4.1 for $N = 1$ (4.12) and $N = 2$ (4.11) respectively. The approximate solutions (dashed line and dashed-dotted lines) are compared with the exact solution (continuous line). The non-dimensional parameter σ is obtained by considering a slab of unit length with $k_1 = 49.8W/(mK)$ (carbon steel) and $\mu = 20W/(m^2K)$ (air).

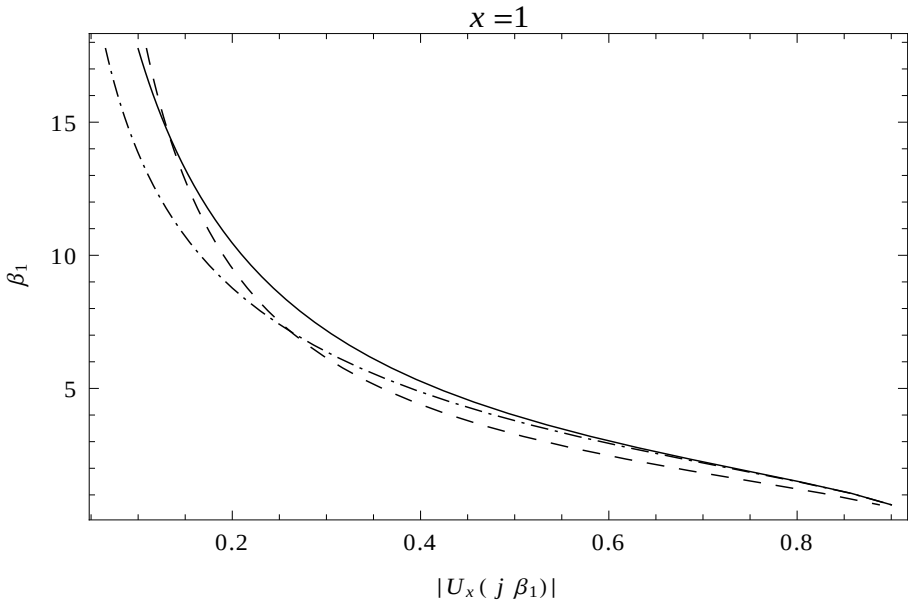

Figure 4.1: Plots of β_1 versus $|U_x(\jmath\beta_1)|$ from the analytical quadrupoles solution (solid line), and the approximated polynomial solution with $N = 1$ (dashed line) and $N = 2$ (dot-dashed line) for a homogeneous slab.

The relative percentage error $100\,|1-\beta_1^a/\beta_1|$ is plotted in figure 4.2 for two values of N ((4.12) and (4.11)) and same values of the non-dimensional parameter σ and x. For low amplitudes U_x the first order polynomial approximation gives lower error than the second order polynomial approximation, whereas of the normalized amplitude approaching 1 the relative error of second order approximation is considerably lower and monotonically decreases consistently with the plot in figure 4.1.

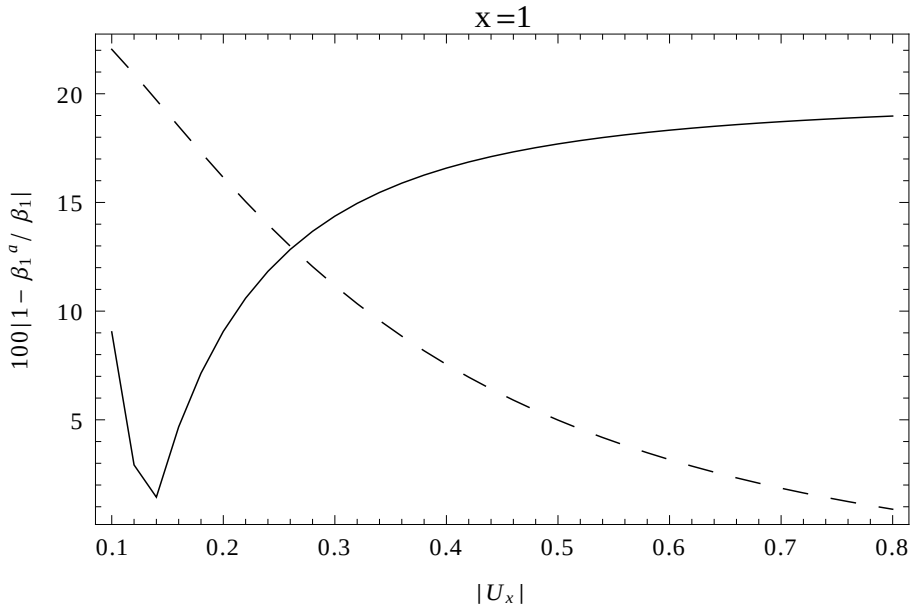

Figure 4.2: Plots of the relative percentage error $100\,|1-\beta_1^a/\beta_1|$ versus $|U_x|$ for $N=1$ (solid line) and $N=2$ (dashed line) .

4.2.2 Two layer slab

We consider a two layer slab ($n=2$) with observation point x at the interface mimicking a test to detect detachments between layers in a composite panel, see figure 3.1. The transfer function is

$$\frac{U_x(s)}{U_1(s)} = \varrho_2\delta_2\beta_1 s\left(\cosh((x-1)\sqrt{\delta_2\beta_1 s}) - \sigma\sinh((x-1)\sqrt{\delta_2\beta_1 s})\right)$$
$$\left(\cosh(a_1\sqrt{\beta_1 s})\cosh((a_1-1)\sqrt{\delta_2\beta_1 s})\left(\varrho_2\sqrt{\delta_2\beta_1 s} + \sigma\varrho_2\sqrt{\delta_2}\right)\right.$$
$$\left.\sinh(a_1\sqrt{\beta_1 s})\sinh((a_1-1)\sqrt{\delta_2\beta_1 s})\left(\varrho_2\delta_2\sqrt{\beta_1 s} + \sigma\right)\right)^{-1} \tag{4.17}$$

The first three coefficients that define the approximate transfer function G_a (for $N = 2$) are

$$b_0 = 1 + \frac{\varrho_2\sigma a_1}{\varrho_2 + \sigma(1-a_1)} \tag{4.18}$$

$$b_1 = \frac{a_1}{6(\varrho_2+\sigma(1-a_1))^2}\left(\sigma^2(3-\varrho_2-2\varrho_2\delta_2)a_1^3 + \sigma(\sigma+\varrho_2)(6-\varrho_2-6\varrho_2\delta_2)a_1^2\right.$$
$$\left. + 3(\sigma+\varrho_2)^2(1-2\varrho_2\delta_2)a_1 + 2\varrho_2\delta_2(3\varrho_2^2+3\varrho_2\sigma+\sigma^2)\right) \tag{4.19}$$

$$b_2 = \frac{a_1}{360(\varrho_2+\sigma(1-a_1))^3}\left(\sigma^3\left((\varrho_2(3+4(5-2\delta_2)\delta_2)) - 15\right)a_1^6\right.$$
$$+ \sigma^2(\varrho_2+\sigma)\left((16\delta_2(3\delta_2-5)-6)\varrho_2+45\right)a_1^5 - 3\sigma(\sigma+\varrho_2)^2\left((40(\delta_2-1)\delta-2-1)\varrho_2+15\right)a_1^4$$
$$+ 5\left(12\varrho_2^4\delta_2(3\delta_2-1) + \varrho_2^3(48\delta_2(2\delta_2-1)\delta_2+3) + 3\varrho - 2^2\sigma(16\delta_2(2\delta_2-1)\sigma+3)\right)a_1^3$$
$$- 20\delta_2\varrho_2(\varrho_2+\sigma)(6\delta_2-1)(3\varrho_2^2+3\varrho_2\sigma+\sigma^2)a_1^2$$
$$\left. +24\delta_2^2\varrho_2(15\varrho_2^3+20\varrho_2^2\sigma+10\varrho_2\sigma^2+2\sigma^3)a_1 + 8\delta_2^2\varrho_2(15\varrho_2^3+15\varrho_2^2\sigma+6\varrho_2\sigma^2+\sigma^3)\right) \tag{4.20}$$

The plot in figure 4.3 shows the first order (dashed line) and second order (dot-dash line) approximate solutions versus the analytical quadrupoles solution (continuous line). Values of non-dimensional parameters used to compute the coefficients in (4.18)-(4.20) are in table 4.1

The set of parameters has been obtained by considering material 1 and material 2 to be, respectively, carbon steel and aluminum.

Table 4.1: Nondimensional parameters for two layer material with observation point at the interface

a_1	δ_2	ϱ_2	σ	x
0.500	0.133	5.02	0.080	0.5

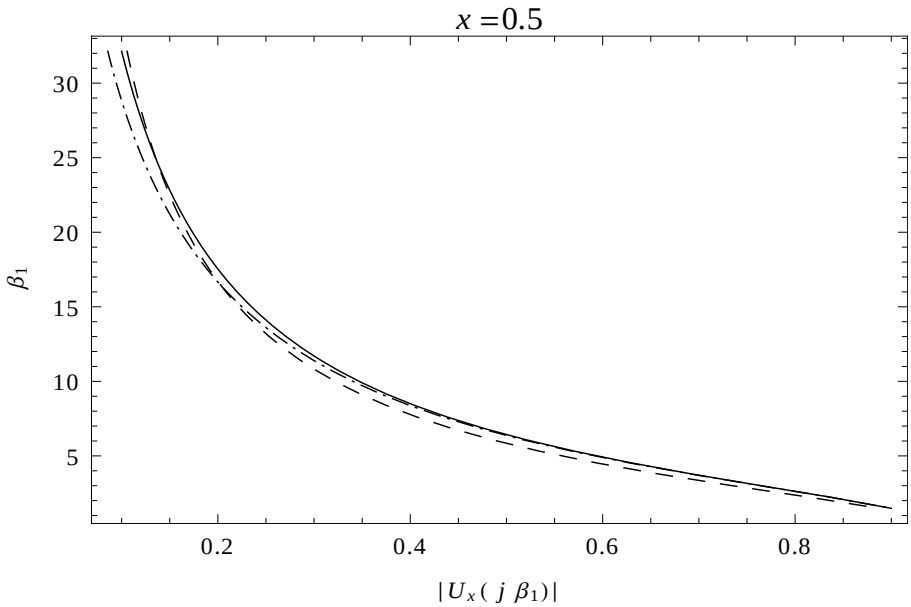

Figure 4.3: Plots of β_1 versus $|U_x(\jmath\beta_1)|$ from the analytical quadrupoles solution (solid line), and the approximated polynomial solution with $N = 1$ (dashed line) and $N = 2$ (dot-dashed line) for a two layer slab.

The relative percentage error $100\,|1 - \beta_1^a/\beta_1|$ is plotted in figure 4.4 for two values of N (4.11) and (4.12) and the same values of the non-dimensional parameters. For low amplitudes U_x the first order polynomial approximation gives lower errors than the second order polynomial approximation, whereas for the normalized amplitude approaching 1 the relative error of the second order approximation is lower. The simple first order approximation in (4.12) allows in this case to estimate the non-dimensional excitation frequency β_1 within a maximum error of about 10%.

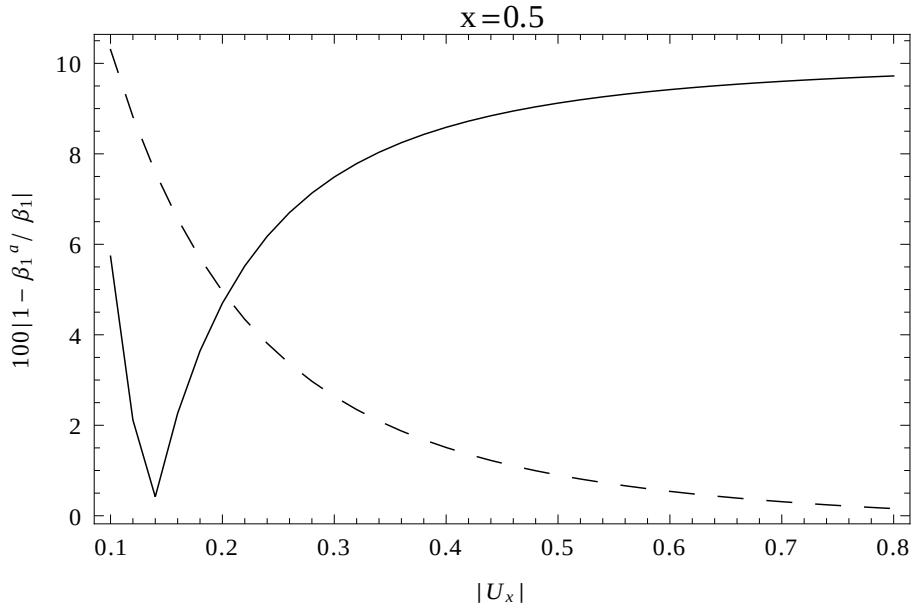

Figure 4.4: Plots of the relative percentage error $100\,|1-\beta_1^a/\beta_1|$ versus $|U_x|$ for $N=1$ (solid line) and $N=2$ (dashed line) (Two layer slab).

Dimensional example

We consider a two layer slab with the same parameters as above. To estimate the frequency of excitation ω we use the first order approximation in (4.12). From the definition of β_1 we obtain the dimensional formula

$$\omega = \frac{\alpha_1\beta_1}{l^2} = \frac{\alpha_1}{l^2 b_1}\sqrt{\frac{1}{|u_x|^2} - b_0^2} \tag{4.21}$$

For a carbon steel we have $\alpha_1 = 1.34\times 10^{-5} m^2 s^{-1}$. Moreover, for the non-dimensional parameters in table 4.1 (obtained by considering carbon steel and aluminum as materials for the two layer slab) we have the following expressions for b_0 and b_1 in terms of $x \in [0,1]$

$$b_0 = \frac{5.26}{5.1 - .08x} \tag{4.22}$$

$$b_1 = \frac{6.23 + 3.42x - 1.79x^2 + 0.00936x^3}{(5.1 - 0.08x)^2} \tag{4.23}$$

For $x = a_1 = 0.5$ and $l = 1$ the plot of ω versus $|u_x|/U$ (4.21) is given in figure 4.5. This plot gives the range of excitation frequencies that need to be used in order to

detect defects in an eventual experiment. Therefore the inverse formula can be use for parameter predetermination in experiments.

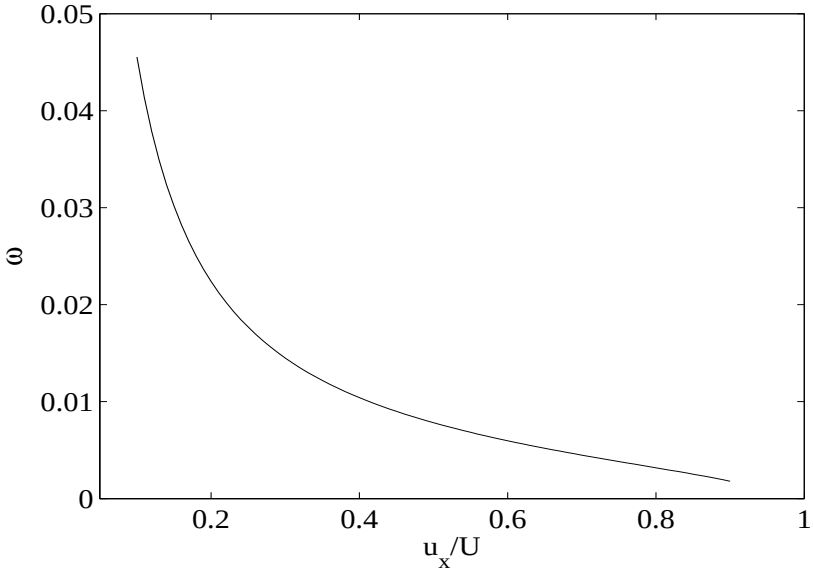

Figure 4.5: For a two layer slab comprised of carbon steel and aluminum, plot of the frequency of excitation ω versus $|u_x|/U$.

4.3 Inclusion at the interface

In this section, we derive a relation between the frequency of excitation and temperature at observation point to predetermine the frequency of excitation for experimental set-up design when there is an inclusion at the interface. Non-dimensional thermal quadrupole method is used to obtain this relation by considering $x = 1$. Therefore the transfer function is $G(s) = \frac{U_x(s)}{U_1(s)} = \frac{U_2(s)}{U_1(s)}$.

In multilayer material, it is possible to have an inclusion when the layers are attached to each other. The inclusion can be an air gap or be conductive glue which fills up the clearance at the interface. Regarding the thermal properties, the inclusion can be approximated by (a) resistance (R) and (b) capacitance (C_t). Resistance is an approximation of the air gap since it has a very low thermal conductivity while the high conductive glue is approximated with capacitance. The accuracies of these approximations are assessed by comparing with the analytical solution.

Figure 4.6 shows the geometry and boundary condition of the two-layer slab with

the inclusion. The front face of the slab is excited with the sinusoidal thermal wave, $u(x,t) = U \sin \omega t$ while there is a convective boundary condition at the rear face with thermal coefficient, μ.

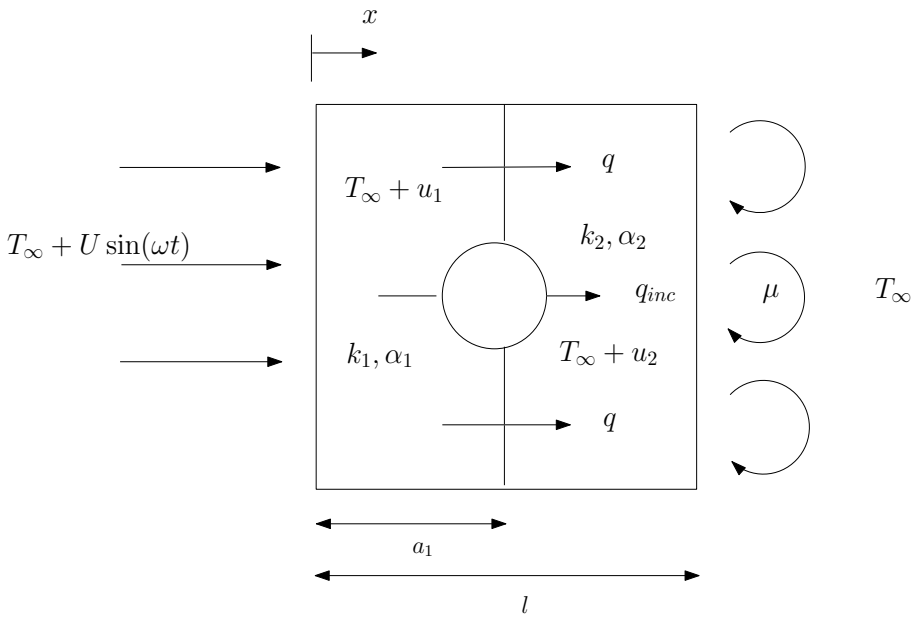

Figure 4.6: Schematic of the two-layer slab with an inclusion at the interface and the boundary condition of the sinusoidal excitation on one side and convection on the other side. q and q_{inc} are the flux at interface for perfect contact and inclusion, respectively

For approximation, the cross section of the inclusion is considered equal to the cross section of the slab. In other words, effect of flux from top and bottom of the inclusion on the temperature at the back of the inclusion is neglected.

4.3.1 Approximation of air gap at the interface with resistance R

Air has a very low thermal conductivity ($0.0243 W/mK$) which makes it as a good insulator. This thermal property causes localized temperature drops, see figure 4.7. The length of the domain for inclusion is $0.005m$. The first layer is a Kevlar composite with thermal $k_1 = 0.32 W/mK$ and $\alpha_1 = 1.8601 \times 10^{-7} m^2/s$, pvc for the second layer with $k_2 = 0.19 W/mK$ and $\alpha_2 = 1.5313 \times 10^{-7} m^2/s$ and an air gap at the interface with thickness $0.0001m$.

Following [30] we model the effect of the air gap with a thermal resistance. The resistance is given by the following formula [30]

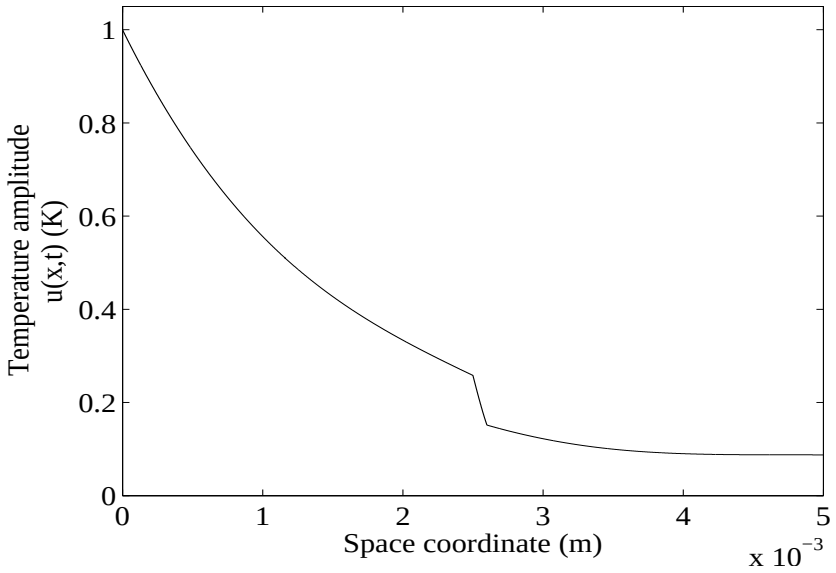

Figure 4.7: Temperature distribution through the domain with an inclusion (resistance) at the interface

$$R = \frac{l_3}{k_3} \tag{4.24}$$

where l_3 is the length of the air gap and k_3 is the thermal conductivity of the filling material, air in this case. To check the accuracy of this approximation, results are compared with analytical solution and also thermal quadrupole method. Table 4.2 shows this comparison.

Table 4.2: Comparison between analytical solution, quadrupole method with approximation with R

$\omega(rad/sec)$	Appximation with R	Analytical solution of (3.2)	Quadrupole
0.01	0.6234	0.6234	0.6289
0.05	0.2772	0.2772	0.2872
0.09	0.1403	0.1403	0.1475
0.14	0.07138	0.07138	0.7601

The comparison is carried on for four different frequency of excitations, $\omega = 0.01$, 0.05, 0.09 and $0.14(rad/sec)$. As the results show, the accuracy of the quadrupole representation is increased by adding the thermal resistance to model the air gap.

In order to non-dimensionalize the resistance, the nominator of (4.24) is divided by the total length of the domain, l and we introduce $\lambda = l_3/l$. The denominator of (4.24) is divided by k_1 which allows us to introduce the nondimensional parameter $\varrho_r = k_3/k_1$. Therefore the nondimensional resistance $\bar{R}$ is

$$\bar{R} = \frac{\lambda}{\varrho_r} \tag{4.25}$$

According to the [30] we have the following relations across the thin layer thermally modelled by the resistance

$$U_1 - U_2 = RQ_1 \tag{4.26a}$$

$$Q_1 = Q_2 \tag{4.26b}$$

These equations (4.26) can be written in matrix form:

$$\begin{bmatrix} U_1(s) \\ Q_1(s) \end{bmatrix} = \begin{bmatrix} 1 & \bar{R} \\ 0 & 1 \end{bmatrix} \begin{bmatrix} U_2(s) \\ Q_2(s) \end{bmatrix} \tag{4.27}$$

The input to output relation of the whole domain is given by the following expression

$$\begin{bmatrix} U_1(s) \\ Q_1(s) \end{bmatrix} = M_0^1 \begin{bmatrix} 1 & \bar{R} \\ 0 & 1 \end{bmatrix} M_1^2 \begin{bmatrix} 1 & 1/\sigma \\ 0 & 1 \end{bmatrix} \begin{bmatrix} U_\infty(s) \\ Q_\infty(s) \end{bmatrix} \tag{4.28}$$

The observation point is $x = 1$ and one can find the transfer function for (4.28)and (3.14). Specifically, the transfer function between U_2 and U_1 is

$$\begin{aligned} &\frac{U_2(s)}{U_1(s)} = \frac{\varrho_2}{\sigma}\sqrt{\delta_2}\beta_1 s \\ &\times \left(\cosh\left((a_1+a_2-1)\sqrt{\beta_1 s}\right)\left(\varrho_2(1+\sigma\bar{R})\sqrt{\delta_2}\beta_1 s\cosh\left(a_1\sqrt{\delta_2\beta_1 s}\right)\right.\right. \\ &+ \left.\left.\sqrt{\beta_1 s}\sinh\left(a_1\sqrt{\delta_2\beta_1 s}\right)\right) + \sinh\left((a_1+a_2-1)\sqrt{\beta_1 s}\right)\right. \\ &\times \left.\left(\varrho_2(\sigma-\sqrt{\beta_1 s}\bar{R})\sqrt{\delta_2}\beta_1 s\cosh\left(a_1\sqrt{\delta_2\beta_1 s}\right) + \sigma\sqrt{\beta_1 s}\sinh\left(a_1\sqrt{\delta_2\beta_1 s}\right)\right)\right)^{-1} \end{aligned} \tag{4.29}$$

The transfer function $G(s)$ is approximated by (4.1) and the coefficients are obtained by (4.2). The first three coefficients are

$$b_0 = \sigma\left(\bar{R} - a_1 - a_2 + \frac{a_1}{\varrho_2} + \frac{1}{\sigma} + 1\right) \tag{4.30}$$

$$b_1 = \frac{1}{4}(a_1+a_2-1)^3(\frac{a_1}{\varrho_2}+1)(\frac{1}{3}-\sigma) + \frac{1}{2}(a_1+a_2-1)^2(1-\bar{R}\sigma) - \bar{R}(a_1+a_2-1)$$
$$- \frac{a_1^2\delta_2}{4}(a_1+a_2-1)\left((\frac{a_1}{3\varrho_2}+1)(1+\sigma)\right) + \frac{a_1^2\delta_2}{2}(1+\bar{R}+\frac{a_1}{3\varrho_2}) \tag{4.31}$$

$$b_2 = \frac{\sigma}{120}\Bigg(\frac{a_1^5\delta_2^2}{\varrho_2} - 5a_1^4\delta_2^2(a_1+a_2-1) + 5a_1^4\delta_2^2\bar{R}$$
$$- 10a_1^2\delta_2(a_1+a_2-1)^3 + \frac{10a_1^2\delta_2(a_1+a_2-1)^2(a_1+3\bar{R}\varrho_2)}{\varrho_2}$$
$$+ \frac{5}{\sigma}\Bigg(a_1^4\delta_2^2 + 6a_1^2\delta_2(a_1+a_2-1)^2 - \frac{4a_1^2\delta_2(a_1+a_2-1)(a_1+3\bar{R}\varrho_2)}{\varrho_2}$$
$$- 4(a_1+a_2-1)^3\left(\frac{a_1}{\varrho_2}+\bar{R}\right) + (a_1+a_2-1)^4\Bigg) + 5(a_1+a_2-1)^4\left(\frac{a_1}{\varrho_2}+\bar{R}\right)$$
$$- (a_1+a_2-1)^5\Bigg) \tag{4.32}$$

$$b_3 = \frac{\sigma}{5040}\Bigg(\frac{a_1^7\delta_2^3}{\varrho_2} - 7a_1^6\delta_2^3(a_1+a_2-1) + 7a_1^6\delta_2^3\bar{R} - 35a_1^4\delta_2^2(a_1+a_2-1)^3$$
$$+ \frac{21a_1^4\delta_2^2(a_1+a_2-1)^2(a_1+5\bar{R}\varrho_2)}{\varrho_2} - 21a_1^2\delta_2(a_1+a_2-1)^5$$
$$+ \frac{1}{\varrho_2}\left(35a_1^2\delta_2(a_1+a_2-1)^4(a_1+3\bar{R}\varrho_2)\right) + \frac{1}{\sigma}\Bigg(7\Bigg(a_1^6\delta_2^3 + 15a_1^4\delta_2^2(a_1+a_2-1)^2$$
$$- \frac{6a_1^4\delta_2^2(a_1+a_2-1)(a_1+5\bar{R}\varrho_1)}{\varrho_2} + 15a_1^2\delta_2(a_1+a_2-1)^4 - \frac{20a_1^2\delta_2(a_1+a_2-1)^3(a_1+3\bar{R}\varrho_2)}{\varrho_2}$$
$$- 6(a_1+a_2-1)^5\left(\frac{a_1}{\varrho_2}+\bar{R}\right) + (a_1+a_2-1)^6\Bigg)\Bigg) + 7(a_1+a_2-1)^6\left(\frac{a_1}{\varrho_2}+\bar{R}\right)$$
$$- (a_1+a_2-1)^7\Bigg) \tag{4.33}$$

For $n = 2$ (dashed line) and $n = 3$ (dotted-dash line) the plot of the left-hand side of (4.6) versus β_1 is shown in figure 4.8, with the horizontal line representing the right-hand side for $|u_2| = 0.6289$. The intersection represents the solution of the implicit inverse problem (4.6) which is approximately 1.27. To check the accuracy, we compute the frequency of excitation by $\omega = (\beta_1\alpha_2)/(\delta_2 l^2)$. Substituting the related value we have $\omega = (1.27 \times 1.5313 \times 10^{-7})/(0.8232 \times 0.005^2) = 0.0094$ which is very close to the result in the table 4.2,$\omega = 0.01$.

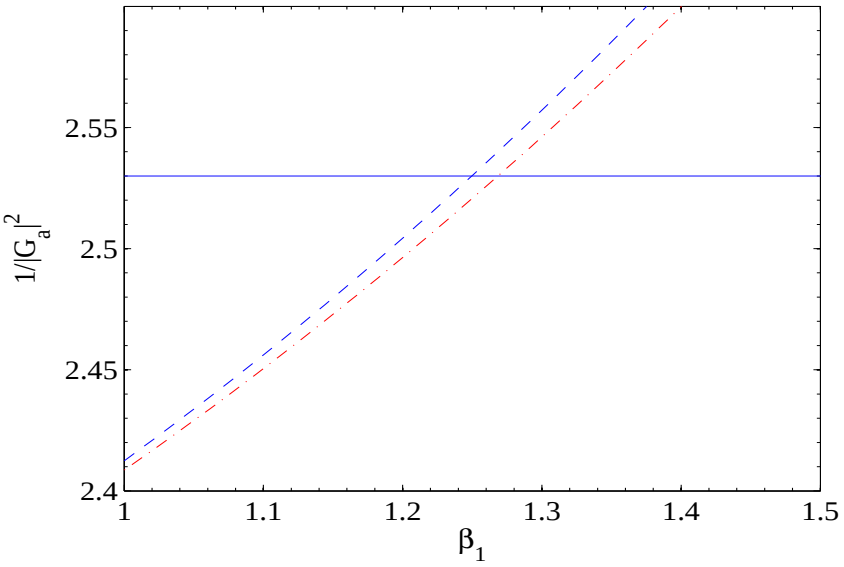

Figure 4.8: Plots of the left hand side of (4.6) versus β_1 for $n = 2$ (dashed line0 and $n = 3$ (dashed-dotted line). The solid line is the graph (versus β_1) of the right-hand side for $|u_2| = 0.6289$

4.3.2 Detachment at the interface approximated by a capacitance

Consider the case with an inclusion characterized by a high thermal conductivity or in which the thermal conductivity is higher than its surrounding. In this condition, having a uniform temperature through the inclusion is expected. Following [30] we approximate the effect of this inclusion by a capacitance, C_t. This scenario can happen when the two layers are attached to each other with conductive glue and the glue fills up the clearance between these two layers. Figure 4.9 shows the temperature distribution through the domain for the case that two composite materials, $k_1 = 0.32W/Km$ and

$k_2 = 0.19W/Km$, are glued to each other with high conductive resin, $k_c = 3W/Km$ with length $0.0005m$. As the plot shows, inclusion has a uniform temperature.

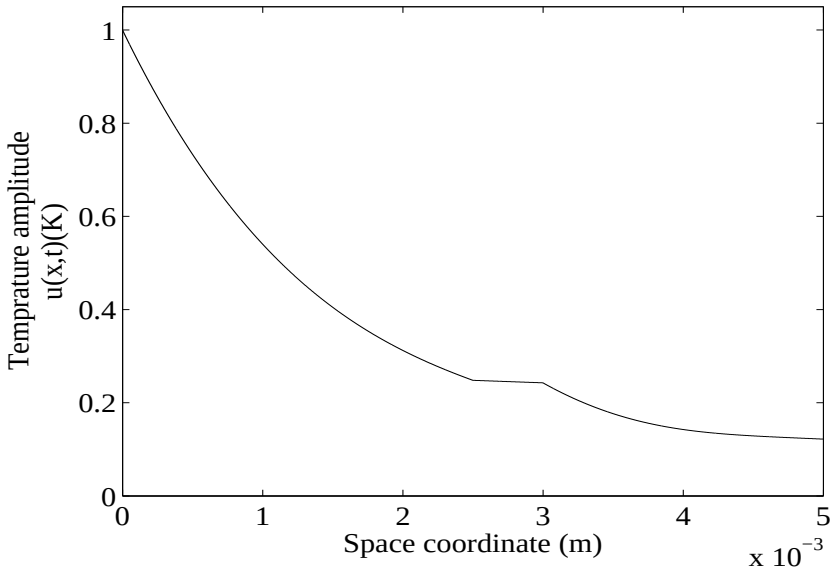

Figure 4.9: Temperature distribution through the domain with a high conductive inclusion at the interface.

The capacitance is given by

$$C_t = \rho C V \tag{4.34}$$

where ρ ,C and V are the density, thermal capacitance and volume of the inclusion, respectively.

For a conductive body with uniform temperature, no bulk heat source and no work done the relation between the heat flux and the temperature is

$$q_c = C_t \frac{du_c}{dt} \tag{4.35}$$

where q_c is the total flux across the boundaries and u_c is the temperature in body. In the Laplace domain we have

$$Q_c(s) = C_t s U_c(s) \tag{4.36}$$

the transformed variables have been indicated by capital letters. We introduce the nondimensional Laplace variable and heat flux by

$$\bar{s} = \frac{s}{\omega}, \quad \bar{Q}_c(\bar{s}) = \frac{Q_c l}{U k_c} \tag{4.37}$$

where U is the amplitude of the boundary sinusoidal temperature excitation and k_c is the thermal conductivity. We define the nondimensional groups

$$\beta_c := \frac{\omega l^2}{\alpha_c}, \quad \delta_c := \frac{\beta_c}{\beta_1} \tag{4.38}$$

where $\alpha_c = k_c/(\rho C)$ is the thermal diffusivity. Therefore the nondimensional relation between total flux on the boundaries and bulk temperature in the inclusion is

$$\frac{V\delta_c}{l}\beta_1 \bar{s}\bar{U}_c(\bar{s}) = \bar{Q}_c(\bar{s}) \tag{4.39}$$

with the nondimensional thermal capacitance given by

$$\bar{C}_t = \frac{V\delta_c}{l}\beta_1 \tag{4.40}$$

which depends on the volume of the inclusion, V, and on the total length l. The effect of the capacitance is therefore relevant if the ratio V/l is not negligible.

For the system in figure 4.6 the input to output relation is given by the following relation

$$\begin{bmatrix} U_1(s) \\ Q_1(s) \end{bmatrix} = M_0^1 \begin{bmatrix} 1 & 0 \\ \bar{C}_t s & 1 \end{bmatrix} M_1^2 \begin{bmatrix} 1 & 1/\sigma \\ 0 & 1 \end{bmatrix} \begin{bmatrix} U_\infty(s) \\ Q_\infty(s) \end{bmatrix} \tag{4.41}$$

The plot of ω versus the temperature amplitude at $x = 1$ obtained from the analytical solution of system (3.3) and from the quadrupoles solution with thermal capacitance is given in figure 4.10. Thermal conductivity of first and second layer are $k_1 = 0.32W/Km$ and $k_2 = 0.19W/Km$ and they are glued by high conductive resin with $k_c = 3W/Km$.

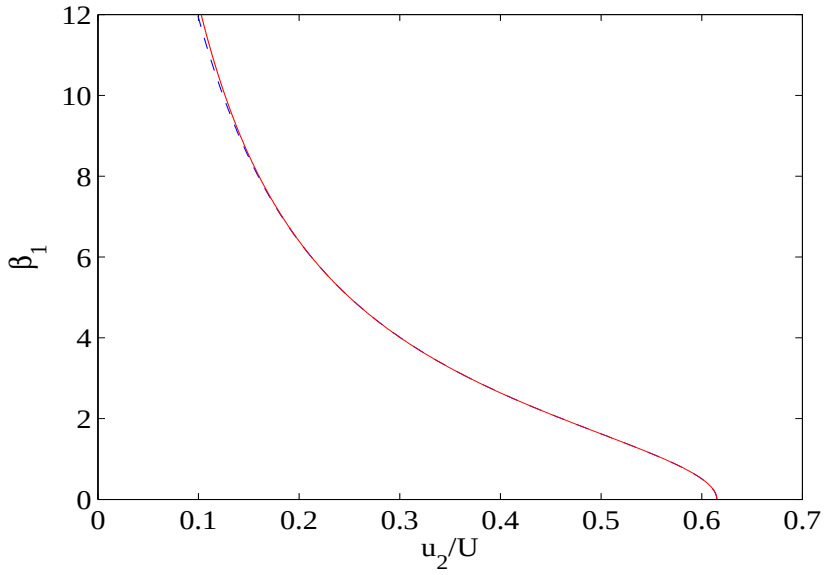

Figure 4.10: Comparison between the analytical solution (solid line) and approximation of the inclusion with C_t (dashed line)

The observation point is the back side of the slab and by considering $x = 1$, one can find the transfer function for (4.41) and (3.14). Specifically, the transfer function between U_2 and U_1 is

$$\begin{aligned}
&\frac{U_2(s)}{U_1(s)} = \frac{\varrho_2}{\sigma}\sqrt{\delta_2}\beta_1 s \\
&\times \Bigg(\cosh((a_1+a_2-1)\sqrt{\beta_1 s}) \Bigg(\varrho_2\sqrt{\delta_2}\beta_1 s \cosh(a_1\sqrt{\delta_2\beta_1 s}) \\
&+ (\sigma\sqrt{\beta_1 s} + (\beta_1 s)^{3/2}\bar{C}_t)\sinh(a_1\sqrt{\delta_2\beta_1 s}) \Bigg) \\
&- \sinh((a_1+a_2-1)\sqrt{\beta_1 s}) \Bigg(\sigma\varrho_2\sqrt{\delta_2\beta_1 s}\cosh(a_1\sqrt{\delta_2\beta_1 s}) \\
&+ (\sigma\bar{C}_t - 1)\beta_1 s \sinh(a_1\sqrt{\delta_2\beta_1 s}) \Bigg) \Bigg)^{-1}
\end{aligned} \tag{4.42}$$

The transfer function is approximated by (4.1) and the coefficients are obtained by (4.2). The first three coefficients are

$$b_0 = \sigma\left(a_1/\varrho_2 - a_1 - a_2 + 1/\sigma + 1\right) \tag{4.43}$$

$$b_1 = \sigma\Bigg(\frac{3(a_1+a_2-1)^3}{12} - (a_1+a_2-1)\left(\frac{a_1^2\delta_2}{2}+\frac{a_1\bar{C}_t}{\varrho_2}\right)$$
$$+\frac{(a_1+a_2-1)^2+a_1^2\delta_2}{2\sigma}+\frac{\bar{C}_t a_1 - a_1(a_1+a_2-1)}{\sigma\varrho_2}-\frac{a_1^3\delta_2^{3/2}}{12\varrho_2\delta_2^{1/2}}-\frac{a_1\delta_2^{1/2}(a_1+a_2-1)^2}{4\varrho_2\delta_2^{1/2}}$$
$$+a_1\frac{(a_1+a_2-1)^2+a_1^2\delta_2}{4\varrho_2}+a_1\frac{(a_1+a_2-1)^2}{2\varrho_2}\Bigg) \tag{4.44}$$

$$b_2 = \frac{\sigma}{120}\Bigg(-\frac{5a_1^3\delta_2(a_1+a_2-1)(a_1\delta_2\varrho_2+4\bar{C}_t)}{\varrho_2}+$$
$$\frac{a_1}{\varrho}\left(a_1^4\delta_2^2+10a_1^2\delta_2(a_1+a_2-1)^2\right)+\frac{5a_1}{\varrho}(a_1+a_2-1)^4$$
$$+\frac{5a_1}{\varrho}(a_1+a_2-1)^4+\frac{5}{\sigma}\Bigg(a_1^4\delta_2^2+\frac{4a_1^3\bar{C}_t\delta_2}{\varrho_2}+\frac{4a_1(a_1+a_2-1)\left(a_1^2(-\delta_2)-(a_1+a_2-1)^2\right)}{\varrho_2}$$
$$+\frac{6a_1(a_1+a_2-1)^2(a_1\delta_2\varrho_2+2\bar{C}_t)}{\varrho_2}+(a_1+a_2-1)^4\Bigg)-\frac{10a_1(a_1+a_2-1)^3(a_1\delta_2\varrho_2+2\bar{C}_t)}{\varrho_2}$$
$$-(a_1+a_2-1)^5\Bigg) \tag{4.45}$$

For $n = 2$ and $n = 3$ the plot of the left-hand side of (4.6) versus β_1 is shown in figure 4.8, with the horizontal line representing the right-hand side for $|u_2| = 0.3403$. The intersection represents the graphical solution of the implicit inverse problem (4.6) which is approximately 6.5.

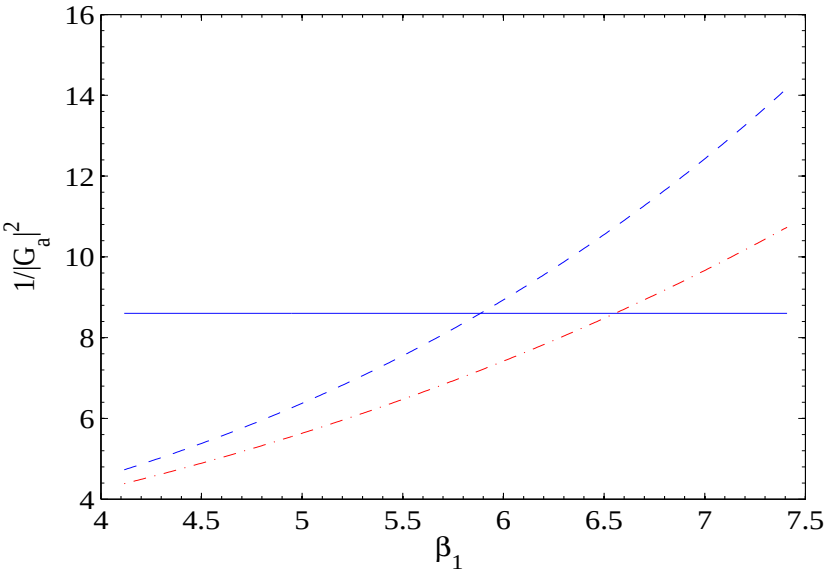

Figure 4.11: Plots of the left hand side of (4.6) versus β_1 for $n = 2$ (dashed line and $n = 3$ (dashed-dotted line). The solid line is the graph (versus β_1) of the right-hand side for $|u_2| = 0.3403$

Chapter 5

Effect of the finite length of the domain in the problem of frequency predetermination

5.1 Introduction

The goal of this chapter is to assess the effect of finite length of the domain on the solution of the inverse problem. A closed form solution of the inverse problem was derived in [38] within the assumption of semi-infinite domain. Here we investigate the effect of the finite length and indirectly assess the validity of the semi-infinite domain simplified framework. The final goal is to establish the peculiar conditions that require the additional complications associated to the solution in the finite domain.

5.2 Fourier series solution

The Fourier series solution of the non homogeneous initial-boundary- values problem (3.2) for $i = 1$ (in the remaining part of the thesis we will drop the subscript 1) is obtained by transforming it into a semi-homogeneous problem. Following [4], we express the solution for in the form

$$u(x,t) = S(x,t) + \nu(x,t) \tag{5.1}$$

where $S(x,t) = A(t)\,x + B(t)$ satisfies the non-homogeneous boundary condition (3.2b). Time dependent coefficients $A(t)$ and $B(t)$ are determined by enforcing the boundary

conditions (3.2e) and (3.2c). We obtained

$$B(t) = U\sin(\omega t) \tag{5.2a}$$

$$A(t) = \frac{U\mu\sin(\omega t)}{k+\mu l} \tag{5.2b}$$

and

$$S(x,t) = \frac{U\mu\sin(\omega t)}{k+\mu l}x + U\sin(\omega t) \tag{5.3}$$

Substituting from (5.1) into (3.2) gives an homogeneous initial boundary-value-problem for U with internal heat source given by $-\partial S/\partial t$

$$\frac{\partial\nu}{\partial t} + \frac{\partial S}{\partial t} = \alpha\frac{\partial^2\nu}{\partial x^2} \Rightarrow \frac{\partial\nu}{\partial t} = \alpha\frac{\partial^2\nu}{\partial x^2} + \frac{\mu\omega\cos(\omega t)}{k+\mu l}x - \omega\cos(\omega t) \tag{5.4a}$$

$$\nu(0,t) = 0 \tag{5.4b}$$

$$k\frac{\partial\nu}{\partial x}(l,t) + \mu\nu(l,t) = 0 \tag{5.4c}$$

$$\nu(x,0) = 0 \tag{5.4d}$$

To solve the initial-boundary-value problem, separation of variable is used. We have

$$\nu(x,t) = X(x)\,\psi(t) \tag{5.5}$$

by substituting it in (3.2a) we obtain

$$X(x)\frac{\partial\psi}{\partial t} = \alpha\frac{\partial^2 X}{\partial x^2}\psi(t) \tag{5.6}$$

therefore

$$\frac{\frac{\partial\psi}{\partial t}}{\alpha\psi(t)} = \frac{\frac{\partial^2 X}{\partial x^2}}{X(x)} = \lambda^2 \tag{5.7}$$

where λ is called separation constant or eigenvalue. Therefore the space and the time parts of the solution satisfy the ordinary differential equations

$$\frac{\partial^2 X}{\partial x^2} = \lambda^2 X(x) \tag{5.8}$$

$$\frac{\partial\psi}{\partial t} = \lambda^2\alpha\psi(t) \tag{5.9}$$

by combining the general solutions we obtain

$$\nu\left(x,t\right)=e^{-\lambda^2\alpha^2 t}\left(A\sin(\lambda x)+B\cos(\lambda x)\right) \tag{5.10}$$

By enforcing the boundary condition (5.4b) and (5.4c), eigenfunctions and eigenvalues are obtained. By applying these boundary conditions to the spatial equation we have

$$B=0 \tag{5.11}$$

$$\begin{aligned} kA\lambda\cos(\lambda l)+\mu A\sin(\lambda l)&=0 \\ \Rightarrow\tan(\lambda l)&=\frac{-k}{\mu}\lambda \end{aligned} \tag{5.12}$$

and the corresponding eigenfunctions are

$$X_n=\sin(\lambda_n x) \tag{5.13}$$

where the eigenfrequencies λ_n, $n=1,2,...$ are the solutions of (5.12). The solution for ν is then written as the series

$$\nu(x,t)=\sum_{n=0}^{\infty}T_n(t)X_n(x) \tag{5.14}$$

The time dependent coefficients T_n are given by

$$T_n=\left[A_n+\int_0^t F_n(s)e^{a_n s}ds\right]e^{-a_n t} \tag{5.15}$$

with

$$F_n=L_n^{-1}\int_0^l \xi(x,t)X_n dx \tag{5.16}$$

where $a_n=\alpha^2{\lambda_n}^2$ and $\xi(x,t)=-\left(\frac{-\mu\omega\cos(\omega t)}{k+\mu l}\right)x-\omega\cos(\omega t)$ which is obtained from (5.4a). Also we have

$$A_n=L_n^{-1}\int_0^l -S(x,0)X_n dx \tag{5.17}$$

$$L_n = \int_0^l X_n^2 dx \tag{5.18}$$

where A_n and L_n are the Fourier coefficients and normalizing constant, respectively.

Fourier coefficients and normalizing constants can be explicitly written as

$$L_n = \int_0^l \sin(\lambda_n x)^2 dx = \frac{1}{2}\left(l - \sin(2\lambda_n l)\right)/2\lambda_n \tag{5.19}$$

$$\begin{aligned} A_n &= L_n^{-1} \int_0^l -S(x,0)\sin(\lambda_n x)dx \qquad (5.20)\\ &= \frac{1}{L_n}\int_0^l \left[-\left(\frac{\mu\sin(0)}{k+\mu l}\right)x\sin(\lambda_n x) + \sin(0)\sin(\lambda_n x)\right]dx \\ &= 0 \end{aligned}$$

$$\begin{aligned} F_n(t) &= L_n^{-1} \int_0^l -\xi(x,t)\sin(\lambda_n x)dx \qquad (5.21)\\ &= \frac{1}{L_n}\int_0^l \left[-\left(\frac{\omega\mu\cos(\omega t)}{k+\mu l}\right)x\sin(\lambda_n x) + \omega\cos(\omega t)\sin(\lambda_n x)\right]dx \\ &= \frac{1}{L_n}\left[\left(\frac{\omega\mu\cos(\omega t)}{k+\mu l}\right)\left(\frac{-l\cos(\lambda_n l)}{\lambda_n} + \frac{\sin(\lambda_n l)}{\lambda_n^2}\right)\right] \\ &+ \frac{1}{L_n}\left[\left(\frac{\omega\cos(wt)}{\lambda_n}\right)\left[\cos(\lambda_n l) - 1\right]\right] \end{aligned}$$

To calculate the integral part in T_n (5.15),we define

$$H = \int_0^t F_n(s) e^{a_n s} ds \tag{5.22}$$

$$= \frac{1}{L_n}\left[\left(\frac{\omega\mu}{k+\mu l}\right)\left(\frac{-l\cos(\lambda_n l)}{\lambda_n} + \frac{\sin(\lambda_n l)}{\lambda_n^2}\right)\right]\int_0^t \cos(\omega s) e^{a_n s} ds$$

$$+ \frac{1}{L_n}\left[\left(\frac{\omega}{\lambda_n}\right)[\cos(\lambda_n l) - 1]\right]\int_0^t \cos(\omega s) e^{a_n s} ds$$

$$H = \frac{1}{L_n}\left[\left(\frac{\omega h}{k+\mu l}\right)\left(\frac{-l\cos(\lambda_n l)}{\lambda_n} + \frac{\sin(\lambda_n l)}{\lambda_n^2}\right)\right]$$

$$\left(\frac{\omega}{(\omega^2 + a_n^2)}\right)\left(\sin(\omega t) e^{a_n t} + \frac{a_n}{\omega}\cos(\omega t) e^{a_n t} - \frac{a_n}{\omega}\right)$$

so that

$$T_n = H e^{-a_n t} \tag{5.23}$$

Substitution into equation (5.1) gives

$$u(x,t) = S(x,t) + \sum_{n=0}^{\infty} T_n(t) X_n(x) \tag{5.24}$$

with steady-state solution given by

$$u_{ss}^F(x,t) = U\sin\omega t\left(1 - \frac{\mu x}{k+\mu l}\right) + U\omega\sum_{n=0}^{\infty}\sin\left(\omega t + \tan^{-1}\frac{\alpha\lambda_n^2}{\omega}\right)\sin\lambda_n x \tag{5.25}$$

5.2.1 Approximate eigenfrequencies

The plot in figure 5.1shows the first graphical solution (circles) of the characteristic equations (5.12). The proximity with the vertical asymptote suggests the possibility of approximating $\lambda_n l$ with the more convenient expression

$$\bar{\lambda}_n \cong (2n-1)\,\pi/2 \tag{5.26}$$

Table 5.1 gives the first five values of the actual and approximation of λ_n.

Table 5.1: Numerical values for the approximation of $\tan(\lambda_n l) = \frac{-k}{\mu}\lambda_n$

eigenvalue	λ_n	$(2n-1)\,\pi/2$
1	67.6253	52.3599
2	163.7727	157.0796
3	265.9555	261.7994
4	369.5179	366.5191
5	473.5812	471.2389

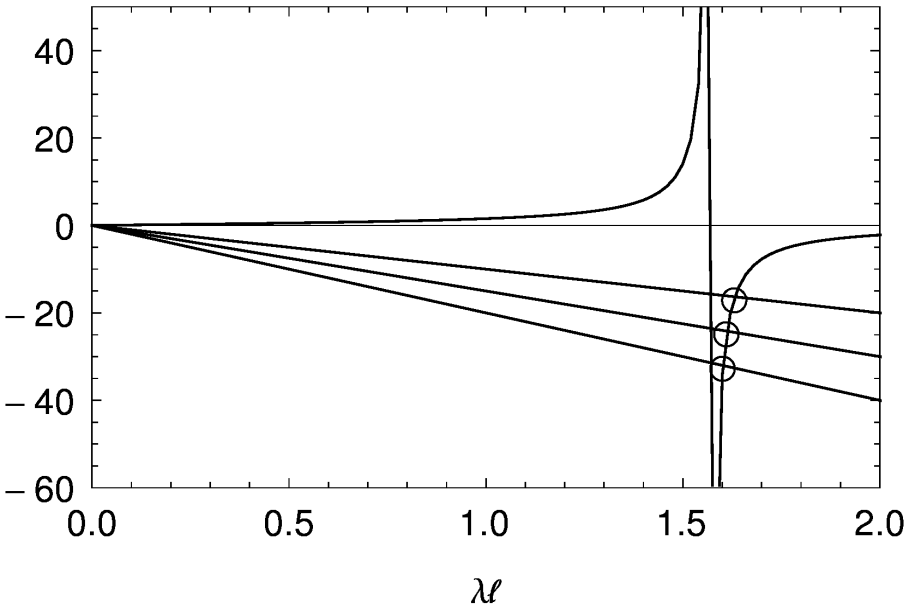

Figure 5.1: Plot of the function $\tan \lambda l$ vs. λl and of the line $-\frac{k}{\mu l}\lambda l$ vs. λl for three values of the non dimensional group $\frac{k}{\mu l}\lambda l$, that is 10,15, and 20. Circles are located on the first root of the characteristic equation (5.12)

5.2.2 Error of eigenvalues approximation

The relative percentage error

$$\epsilon_n = 100\left(1 - \frac{\bar{\lambda}_n}{\lambda_n}\right) \tag{5.27}$$

introduced by the approximated eigenvalues, is plotted in figure 5.2 versus $k/\mu l \in [0.2, 20]$ for $n = 1, 2, 3$. As the figure 5.2 shows, for carbon steel with $k = 49\frac{W}{mK}$ slab with length $l = 1m$ in air with $\mu = 25\frac{W}{m^2K}$ the maximum relative percentage error is $16\% < \epsilon_1 < 18\%$. For a slender bar of length $l = 10m$ the error ϵ_1 increases to about 30%. Interpolation function to estimate the error for $n = 1, 2$ versus $k/\mu l$ have been obtained by fitting data in the range $k/\mu l \in [0.2, 20]$ by assuming the dependency to be a power series of $\mu l/k$ truncated at the third order

$$\epsilon_1 = 37.5 - 19.5\frac{\mu l}{k} + 0.167\left(\frac{\mu l}{k}\right)^2 + 4.27\left(\frac{\mu l}{k}\right)^3 \tag{5.28}$$

$$\epsilon_2 = 4.51 - 0.431\frac{\mu l}{k} + 0.000391\left(\frac{\mu l}{k}\right)^2 + .00844\left(\frac{\mu l}{k}\right)^3 \tag{5.29}$$

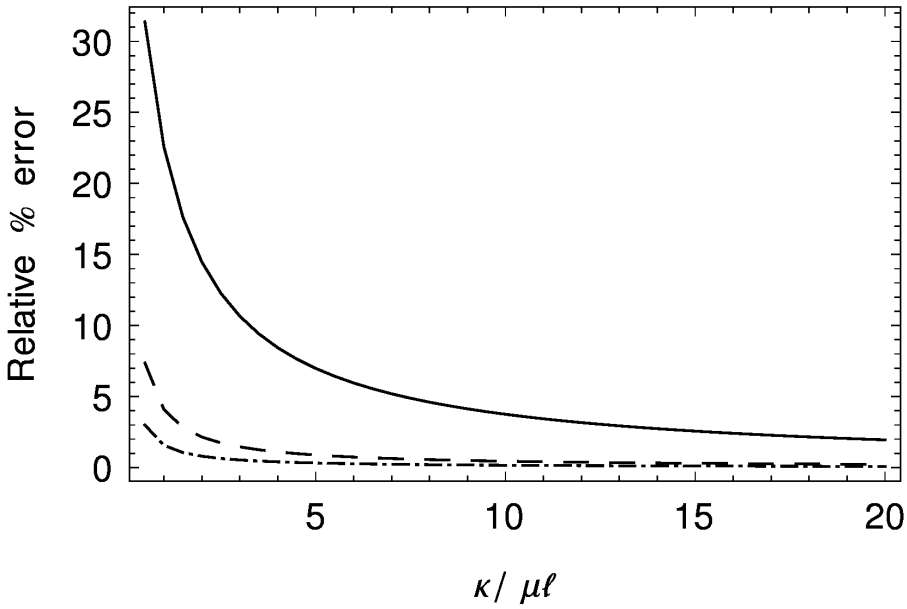

Figure 5.2: Relative error introduce by the approximated frequency vs. $k/\mu l \in [0.2, 20]$ for $n = 1, 2, 3$ (respectively: continuous line, dashed line, dashed-dotted line).

The expression in (5.28) and (5.29) interpolate the data with a maximum relative percentage error of less than 3% in the given range of $\mu l/k$. By using the approximated eigenvalues the boundary condition at $x = l$ is not exactly satisfied.

5.3 Periodic solution

In this section we derive a closed form solution of the initial-boundary-value problem (3.1) that is based on the fact that the boundary condition at $x = 0$ is periodic. The generalized version of (3.1b) is introduced [49]

$$u(0,t) = U exp(\jmath\omega t) \tag{5.30}$$

where $\jmath = \sqrt{-1}$.

Since the excitation is periodic, the solution is expressed as $u(x,t) = \zeta(x) exp(\jmath\omega t)$. In this framework, the second derivative with respect to the space variable can be viewed as a transformation of the time-periodic function with amplitude U at the point $x = 0$ to the time-periodic function of amplitude $\zeta(x)$ at point $x \in [0, l]$.

Substituting into (3.2a) gives the following governing equation for $\zeta(x)$

$$\frac{\partial^2 \zeta}{\partial x^2} - \frac{\jmath\omega}{\alpha}\zeta = 0 \tag{5.31}$$

whose general solution is

$$\zeta(x) = C_1 exp(\sigma x) + C_2 exp(-\sigma x) \qquad\qquad \sigma^2 = \frac{\jmath\omega}{\alpha} \tag{5.32}$$

The constants, C_1 and C_2, as determined by the boundary conditions are

$$C_1 = U\left(\frac{k\sigma - \mu}{k\sigma + \mu}\right)\frac{exp(-2\sigma l)}{1 - \frac{\mu - k\sigma}{\mu + k\sigma} exp(-2\sigma l)} \tag{5.33a}$$

$$C_2 = \frac{U}{1 - \frac{\mu - k\sigma}{\mu + k\sigma} exp(-2\sigma l)} \tag{5.33b}$$

Substituting (5.32) to (5.30) the general solution for the homogenous equation is

$$u(x,t) = \left[C_1 exp(\sigma x) + C_2 exp(-\sigma x)\right] exp(\jmath\omega t) \qquad \sigma = (1+\jmath)\sqrt{\frac{\omega}{2\alpha}} \tag{5.34}$$

Note that for $l \to \infty$ the periodic (steady-state) solution reduces to

$$u_{ss}(x,t) = U exp\left(-x\sqrt{\frac{\omega}{2\alpha}}\right) exp\left(\jmath\left(\omega t - x\sqrt{\frac{\omega}{2\alpha}}\right)\right) \tag{5.35}$$

which is consistent with the approximate steady-state solution found in [38] for a semi-infinite domain.

Consider the complex number $\Xi = \frac{\mu - k\sigma}{\mu + k\sigma} exp(-2\sigma l)$. For $l > 0$ and $\omega > 0$ we have $|exp(-2\sigma l)| < 1$. Therefore the absolute value of Ξ is bounded by

$$|\Xi| \leq \frac{\sqrt{4k^4 + \mu^4}}{2k^2 + \mu^2 + 2k\mu} \tag{5.36}$$

which is always less than one provided that $k > 0$ and $h > 0$. This implies that

$$\frac{1}{1 - \Xi} = \sum_{n=0}^{\infty} \Xi^n = \sum_{n=0}^{\infty} \left(\frac{\mu - k\sigma}{\mu + k\sigma} \right)^n exp(-2n\sigma l) \tag{5.37}$$

by substituting (5.37) into (5.33) gives the steady-state periodic solution in the finite spatial domain

$$\begin{aligned} u_{ss}^p(x,t) = U \sum_{n=0}^{\infty} & \left(\frac{\mu - k\sigma}{\mu + k\sigma} \right)^n \\ & \times \left(exp\left(-\frac{x + 2nl}{\delta} \right) exp\left(\jmath \left(\omega t - \frac{x + 2nl}{\delta} \right) \right) \right. \\ & - \left(\frac{\mu - k\sigma}{\mu + k\sigma} \right) exp\left(\frac{x - (2n+1)\, l}{\delta} \right) \\ & \left. \times exp\left(\jmath \left(\omega t + \frac{x - (2n+1)\, l}{\delta} \right) \right) \right) \end{aligned} \tag{5.38}$$

where $\delta = \sqrt{\frac{2\alpha}{\omega}}$. Terms in the series (5.38) represents thermal wave propagating in the finite domain, with successive reflection at the extremities of the specimen. The $(n+1)^{th}$ reflection occurs at time

$$t_n = \frac{2nl}{\sqrt{2\alpha\omega}} \tag{5.39}$$

respectively at $x = l$ for even n and at $x = 0$ for odd n. For a given time instant it is therefore possible to find the number of reflections occurred up to that time. For $n = 1$ and for a given time lapse, this formula can be used to obtain an estimation of the characteristic length for which the semi infinite domain framework holds.

To evaluate the error between semi-infinite domain and the model with the finite length of the domain, relative error of u_{ss} from (5.35) with respect to u_{ss}^p is defined as follows

$$\epsilon(x,l) = \left|1 - \frac{u_{ss}}{u_{ss}^{p}}\right|(x,l) \tag{5.40}$$
$$= \left|\frac{1 - exp(-2\sigma l)}{1 - \frac{\mu - k\sigma}{\mu + k\sigma} exp(-2\sigma(l-x))}\right|$$

where $|.|$ is the amplitude of the complex number in the argument. As the error equation shows, by increasing the length, l, $\lim_{l\to\infty} \epsilon = 0$ for a finite x. For given observation point x the error decreases as l increases. On the other hand, for a finite length, l, error increases by changing the observation point for 0 to l.

5.4 Results and Comparison

This section is composed of two main parts. In the first part, the prediction of semi-infinite domain solution is compared with the analytical results of Fourier series and periodic solution which are derived in previous sections and with numerical results from ANSYS^{TM} commercial finite element software. In the second part, an interpolating formula between the frequency of excitation ω and the amplitude of the steady-state solution $\left|u_{ss}^{P}\right|$ is derived. Power series based on the closed form solution in [38] prove that in several relevant cases the dominant term is identifiable with the semi-infinite domain solution.

I.Comparison and numerical validation

The results in this section have been computed for carbon steel with the material properties $k = 49.8\ W/Km$ and $\alpha = 1.34 \times 10^{-5} m^2/sec$. The air convection parameter is $\mu = 20\ W/Km^2$.

Figure 5.3 shows the temperature profile from Fourier series solution (5.24) as a function of space and time coordinates for $l = 0.03m$. Convection boundary condition has been considered at the right side of the plate, $l = 0.03m$. Due to the sinusoidal excitation, for every spatial location x the solution oscillates in time with constant amplitude.

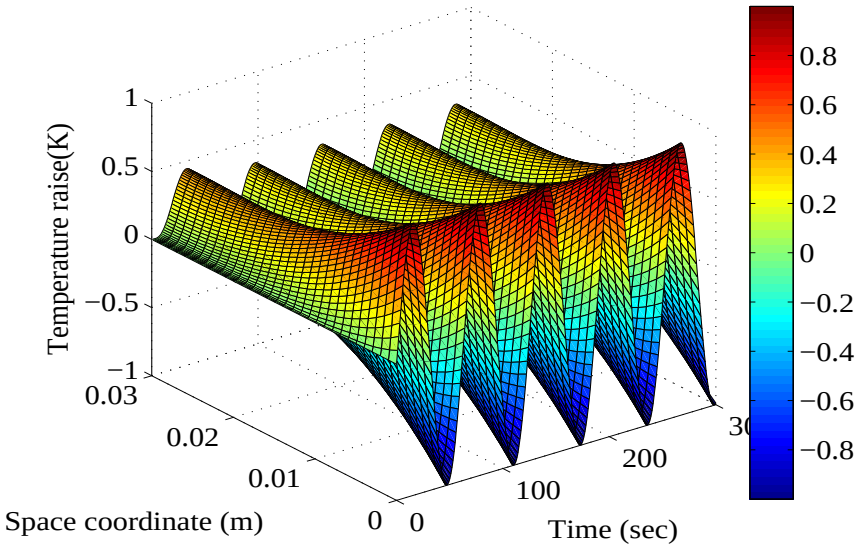

Figure 5.3: Temperature profile in space coordination corresponding to Fourier series solution.

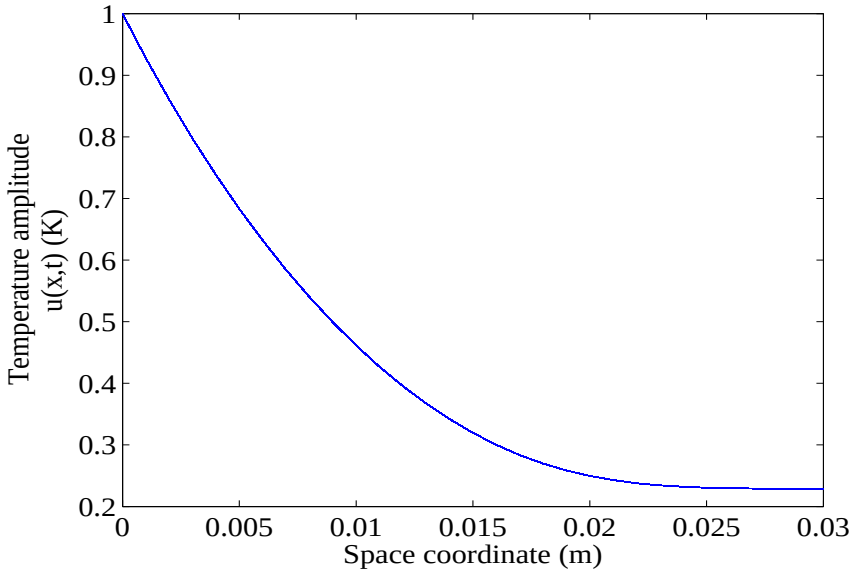

Figure 5.4: Temperature profile in space coordination corresponding to periodic solution.

Temperature amplitude profile for periodic solution with the periodic excitation (5.35) at $x = 0$ and finite length, $l = 0.03m$ with convection boundary condition at $l = 0.03m$ is shown in figure 5.4. The simplified formula of the radial frequency of the excitation as

a function of the temperature profile amplitude was derived in [38] under the hypothesis of semi-infinite domain

$$\omega = \frac{2\alpha}{x^2}\left(\ln\left(\frac{|u_{ss}|\,(x)}{U}\right)\right)^2 \tag{5.41}$$

which is consistent with (5.35).

To assess the validity and limitation of (5.41) two different lengths are considered, $l = 0.03m$ and $l = 1m$, with observation point at $x = 0.03m$. Figure 5.5 illustrates the comparison of ω versus $|u_{ss}/U|$ among the semi-infinite domain, analytical solution from Fourier series and ANSYS software for $l = 1m$, $t = 300s$ and observation point $x = 0.03m$. Observation point is relatively far from the extreme of the spatial domain. As it is shown in the figure 5.5, the semi-infinite domain is qualitively a good approximation of the Fourier series solution in the finite domain, and of ANSYS numerical solution, due to the fact that in this case the observation point is far from the extreme subjected to convection, and therefore the effect of the boundary excitation dominates the effect of the finite length. The same conclusion holds for the plot in figure 5.6 which shows semi-infinite solution reproducing results from ANSYS and from the periodic solution in the finite domain. In this case the two sets of analytical results are virtually overlapped.

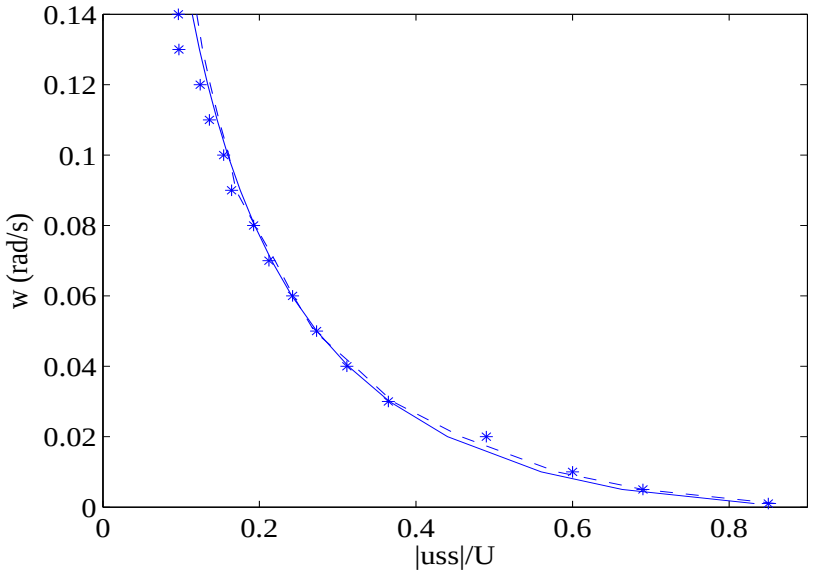

Figure 5.5: For $l = 1m$,$t = 300sec$, and $x = 0.03m$ plots of ω versus $|u_{ss}|$ corresponding to semi-infinite solution (solid line), Fourier series solution in the finite domain (dashed line), and ANSYS numerical simulation(*).

The effect of the finite length cannot be neglected when the temperature is observed at the boundary subjected to convection boundary condition. We consider again a domain of length $l = 0.03m$ with observation point at $x = 0.03m$. At point $x = 0.03m$ the semi-infinite solution is observable [38] and the therefore the comparison is possible. In this case the semi-infinite domain hypothesis obviously fails and the frequency of excitation ω is underestimated. The result is illustrated in figure 5.7.

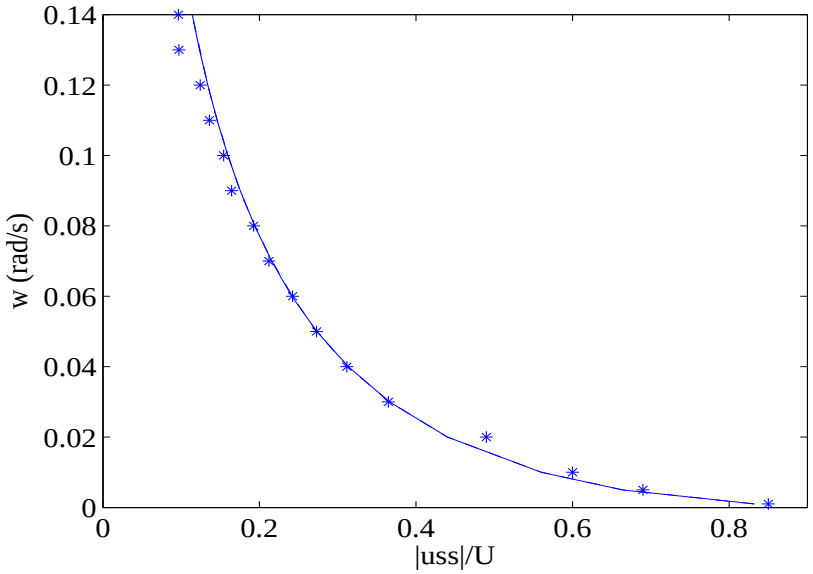

Figure 5.6: For $l = 1m$,$t = 300sec$, and $x = 0.03m$ plots of ω versus $|u_{ss}|$ corresponding to semi-infinite solution (solid line), Periodic solution in the finite domain (dotted-dashed line), and ANSYS numerical simulation (*).

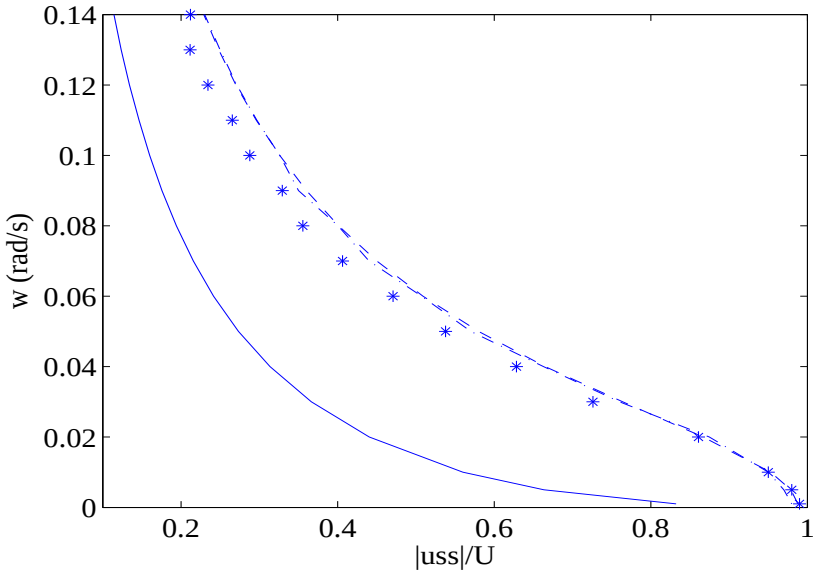

Figure 5.7: For $l = 0.03m$,$t = 300sec$, and $x = 0.03m$ plots of ω versus $|u_{ss}|$ corresponding to semi-infinite solution (solid line), Fourier series solution (dashed line), Periodic solution in the finite domain (dotted-dashed line), and ANSYS numerical simulation (*).

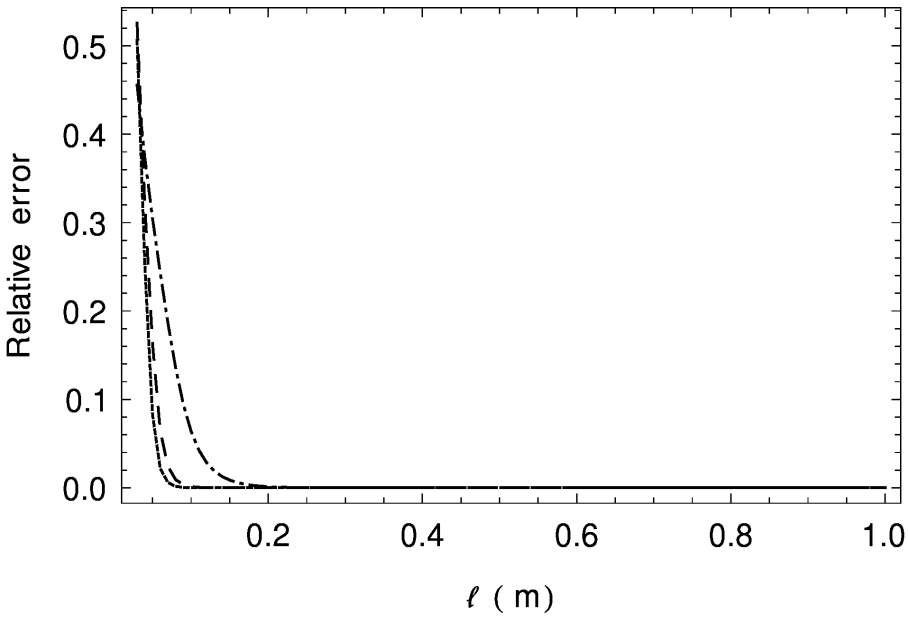

Figure 5.8: Plot of the relative error function $\epsilon(0.03, l)$ versus l for $\omega = 0.01rad/sec$(dotted-dashed line), $\omega = 0.06rad/sec$(dashed line), $\omega = 0.11rad/sec$(solid line).

The error function $\epsilon(x,l)$ in (5.40) is illustrated in figure 5.8. Three values of the excitation frequency are used, namely $\omega = 0.01 rad/sec$(dotted-dashed line), $\omega = 0.06 rad/sec$(dashed line), $\omega = 0.11 rad/sec$ (solid line). The error function indicates that the amplitude rapidly decays to zero as the length increases; the characteristic length at which the error is virtually zero decreases with increasing ω. The result in figure 5.8 implies the validity of semi-infinite approximation for relevant experimental conditions. In addition, if the length of the specimen is relatively larger than the observation point, the related closed form for parametric predetermination can be used to design the experiment.

II.Parameter predetermination with finite length periodic solution

Consider a carbon steel slab with the same material parameters as in the previous subsection. In order to assess the limits of applicability of formula (5.35) with respect to the length l we consider the observation point $x = 0.03\ m$, in which the semi-infinite solution is measurable (in the sense that the amplitude is non zero), and compute the parameter ω versus $\left|u_{ss}^P\right|$ for $l \in [0.03m, 0.4m]$. In order to obtain interpolation expressions that can be compared with (5.35) the data obtained for different values of l is best fitted with power series of $\ln\left|\frac{u_{ss}^P}{U}\right|$:

$$\omega = \sum_{j=0}^{n} a_j \left(\ln\left|\frac{u_{ss}^P}{U}\right|\right)^j \tag{5.42}$$

The first four fitting coefficients ($n = 3$) are plotted in figure 5.9 versus l. For $l > 0.15m$ coefficient $a_2 \to 2\alpha/x^2$ and $a_j \to 0$ for $j \neq 2$. Therefore for carbon steel it is appropriate to use the semi-infinite domain model for $l > 0.15m$ with $x = 0.03m$.

By repeating the same analysis for aluminum ($k = 235 W/Km, \alpha = 8.6 \times 10^{-5} m^2/sec$) we obtain the plot in figure 5.10, which reveals that in this case it is appropriate to use formula (5.35) for parameter predetermination when $l > 0.1m$ and the observation point is locates at $x = 0.03m$.

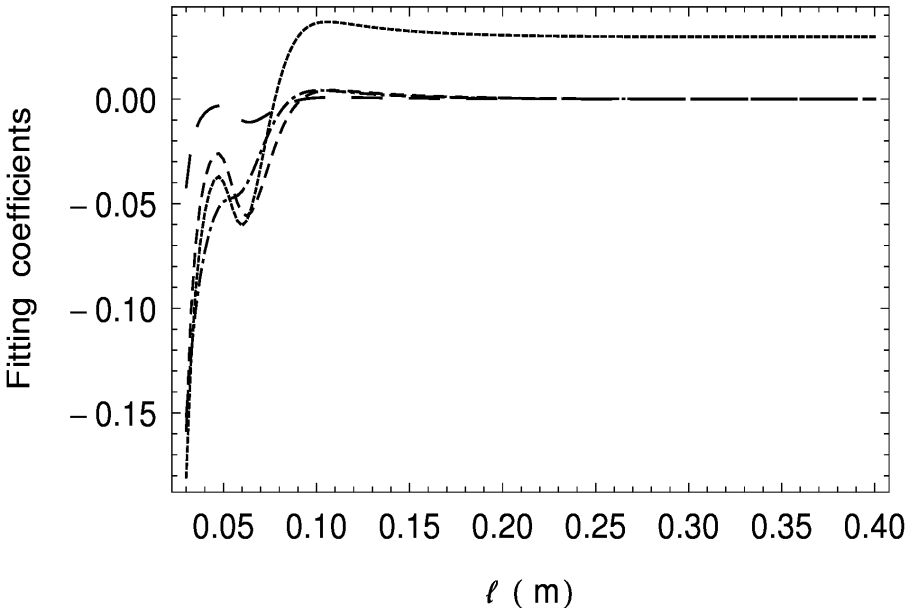

Figure 5.9: Plot of the first four fitting coefficients in (5.42) for $x = 0.03m$. Fine dashed, coarse dashed, continuous, and dashed-dotted lines correspond respectively to fitting coefficients with increasing index. Material is carbon steel.

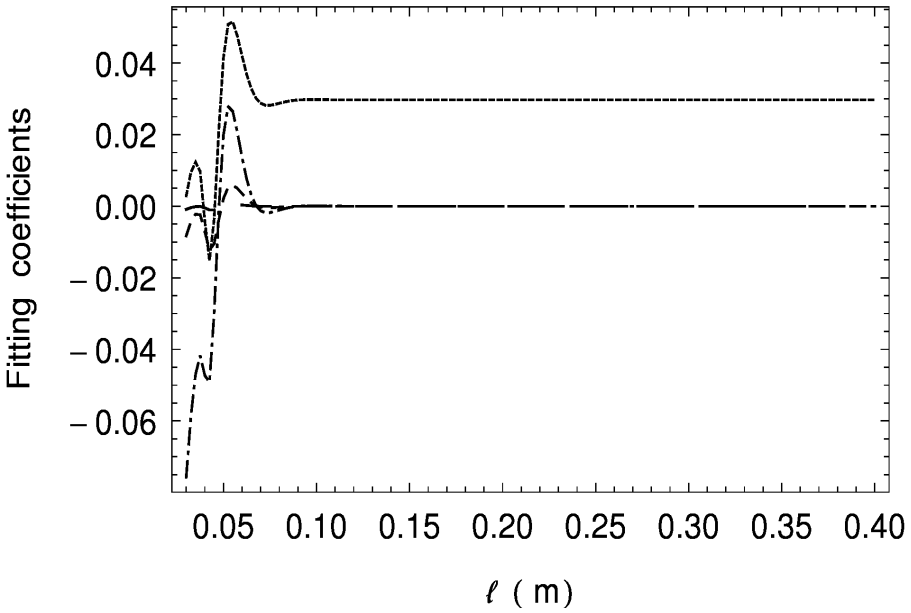

Figure 5.10: Plot of the first four fitting coefficients in (5.42) for $x = 0.03m$. Fine dashed, coarse dashed, continuous, and dashed-dotted lines correspond respectively to fitting coefficients with increasing index. Material is aluminum.

Chapter 6

Experimental validation

6.1 Introduction

The aim of this chapter is to experimentally verify formulas derived in chapter 4. The approximated formulas for frequency of excitation, (4.7), can be used for single layer material and for two layer material when the layers are in a perfect contact. Also, the simplified formula in [38] is assessed experimentally. The frequency of excitation which is obtained by this simplified formula is used in this experiment for fault detection.

6.2 Experiment design

6.2.1 Material and geometry

A. Single-layer

A $50 \times 50 \times 0.6$ cm acrylic glass plate with thermal conductivity $k = 0.3$ W/Km and diffusivity of $\alpha = 1.1239 \times 10^{-7}$ m^2/sec is used for this experiment. Acrylic glass is used because of the low thermal conductivity which allows to localize into a relatively small area the heat transfer and consequently the effect of the edges can be neglected.

To verify that the defect can be detected by the frequency of excitation from simplified formula, (5.41), three defects with deferent sizes are considered. Since a large panel is needed, we divide the panel into four parts. In three of them a circular hole is made as a defect while the fourth one left as a healthy part (no defect in it). In part one and two we introduce a circular hole with diameter $\phi = 2''$ and $\phi = 1''$ and with depth of 3 mm, respectively. These defects are located at the center of each portion which all of them

are at the back side of the plate. In part three, four identical circles with the diameter of $\phi = 0.5''$ are considered. The centre to centre distance between the four holes is $1''$. (see figure 6.1). To avoid effects associated with transparency, the back side of the panel is painted with black paint.

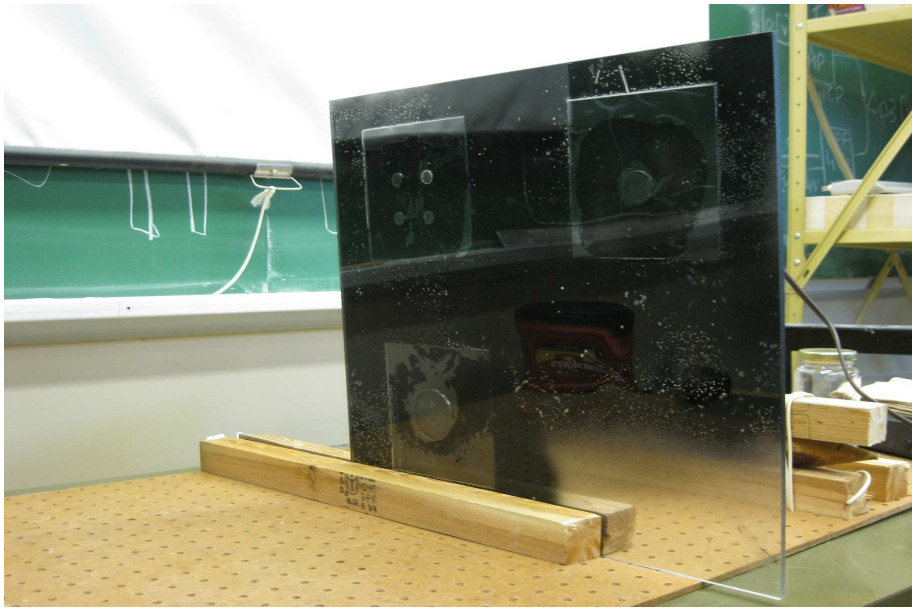

Figure 6.1: Illustrate the specimen with defects, $\phi = 2''$, $\phi = 1''$ and $\phi = 0.5''$

We require the defects to have a flat end to obtain almost uniform temperature distribution. To satisfy this condition, milling is used for machining.

B. Two-layer

To experimentally reproduce an interface, two acrylic glass sheetswith the size of $50 \times 50 \times 0.3$ cm is considered. The layers are glued with Methylene chloride. Since the Methylene chloride loses adhesion properties when heated and since the area subjected to heating is the center, we glue only the regions near the edges. High pressure is applied after putting some glue on the surface. The final thickness is measured by caliper to be 0.006 mm and since the surface is smooth with virtually zero curvature, we assumed perfect contact at the center of the material. To avoid effects associated to transparency the back side of the panel is painted with black paint.

6.2.2 Experiment set-up

The experimental set-up is shown in figure 6.2. An infrared lamp with power 300 W is used to heat the material. The lamp is installed in front of the surface where the defects cannot be seen approximately with the center coincident with the center of the defect. This concentric condition helps to excite the defect in a uniform way since the diameter of the lamp, close to $5''$, is bigger than the defects size. The distance between the lamp and panel is set to 10 cm. An infrared camera FLIR-$i7$ is used to capture the images. The camera specification is given in table 6.1. The camera is equipped with software for post processing the images. We used FLIR R&D to visualize thermal pattern, analyze images, and reduce the noises to have precise detection of deficiencies.

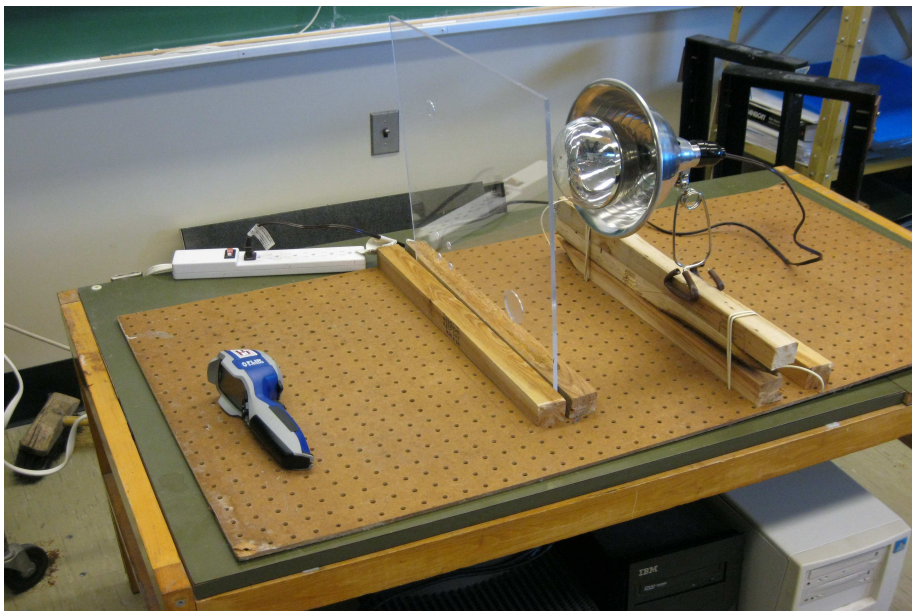

Figure 6.2: Experimental set-up for infrared thermography

6.2.3 Experiment

First, the formula,(5.41), is tested. Second, the approximated formula, (4.7c), for single layer and two-layer are tested.

To produce the frequency of excitation for experiment, the lamp is turned on and off alternatively in a constant period of time which is computed by the $t = \pi/\omega$. For example for $\omega = 0.02\ rad/sec$ we have $t = \pi/.02 = 157.0796\ sec$. The experiment is run for frequency of $\omega = 0.02, 0.05$ and $0.15\ rad/sec$ and the period of excitations are

Table 6.1: FLIR $i7$ specification

Thermal image quality: 140×140 pixels
Field of View: $29°(H) \times 29°(V)$
Spot meter, area with max./min. temperature, isotherm above/below
Field of View: Thermal sensitivity: $0.10°C$

computed and illustrated in table 6.2. The excitation is applied for three cycles and then the images are captured from the same side of excitation during the cool-down process.

Table 6.2: Required time for excitation in experiment for different ω

ω (rad/sec)	0.02	0.05	0.15
time (sec)	157	63	21

A. formula (5.41)

The frequency range for acrylic glass with the defect at the depth of 3 mm is obtained by (5.41) and the result is shown in the figure 6.3.

In order to verify equation (5.41), the parts of the panel with defects are exposed to an oscillatory heat source with three different frequency of excitation. The first two frequencies($\omega = 0.02$ and 0.05) are chosen from the frequency range of detectability predicted by the formula (5.41) and the third frequency, $\omega = 0.15$, is chosen outside the range to verify the prediction (see figure 6.3). As suggested by the analysis in Chapter 5,(see figures 5.5-5.6-5.9-5.10),since the observation point is on the excited surface the finite length should not influence the results, and therefore the simplified formula valid for a semi-infinite domain can be used.

Figures 6.4 to 6.12 show the temperature distribution on the front surface of the acrylic glass. The defects are detected by the given frequency from formula (5.41), $\omega = 0.02$ and 0.05 rad/sec, but for the value of frequency of excitation which is out of the range, $\omega = 0.15$ rad/sec, the images are fuzzier and it would be hard to have a

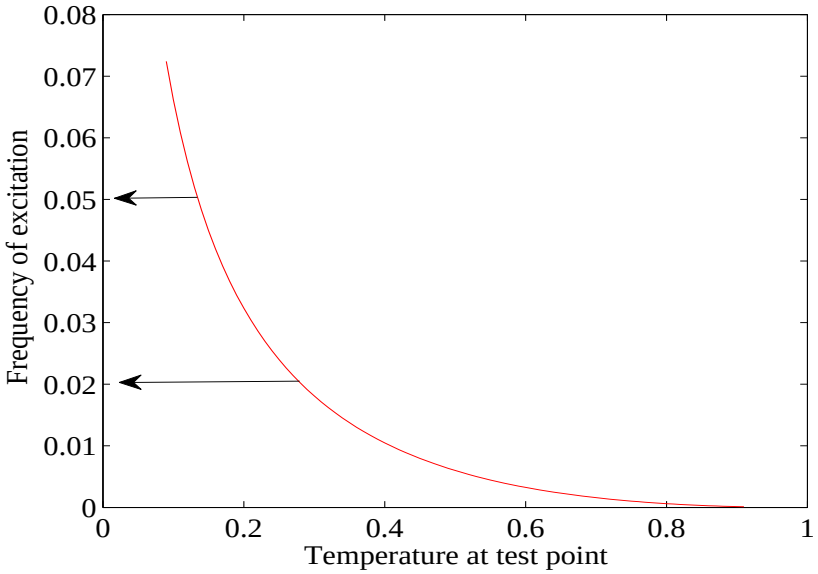

Figure 6.3: Plot of frequency of excitation versus temperature at observation point for acrylic glass with the thickness 6 mm

correct detection. The results show that by increasing the frequency of excitation, the images become fuzzier as predicted by the model. For example, images in figure 6.6 and 6.9 for $\omega = 0.15\ rad/sec$ are fuzzier and because of lacks accuracy we might have a wrong detection.

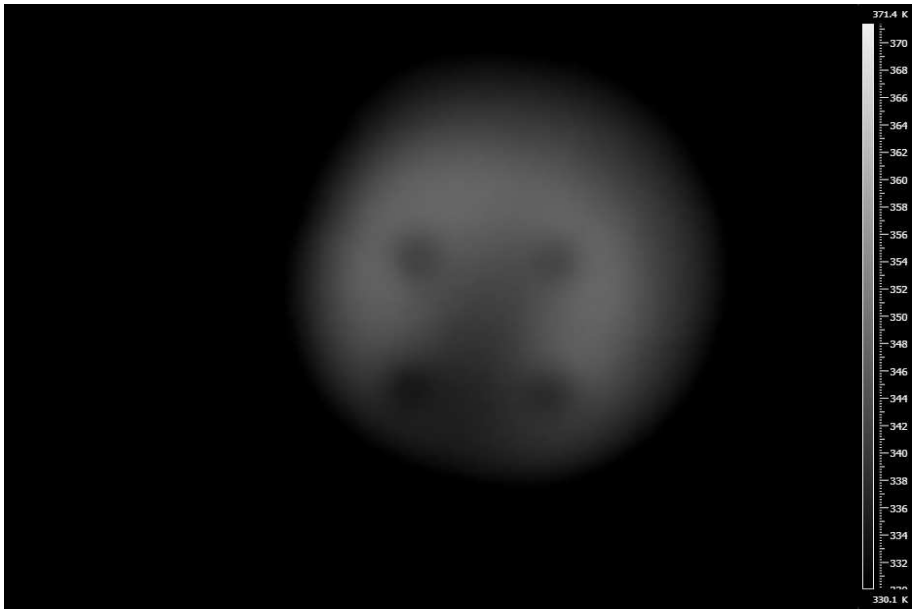

Figure 6.4: Image of temperature distribution for the defect size $\phi = 0.5''$ with the excitation frequency $\omega = 0.02\ rad/sec$

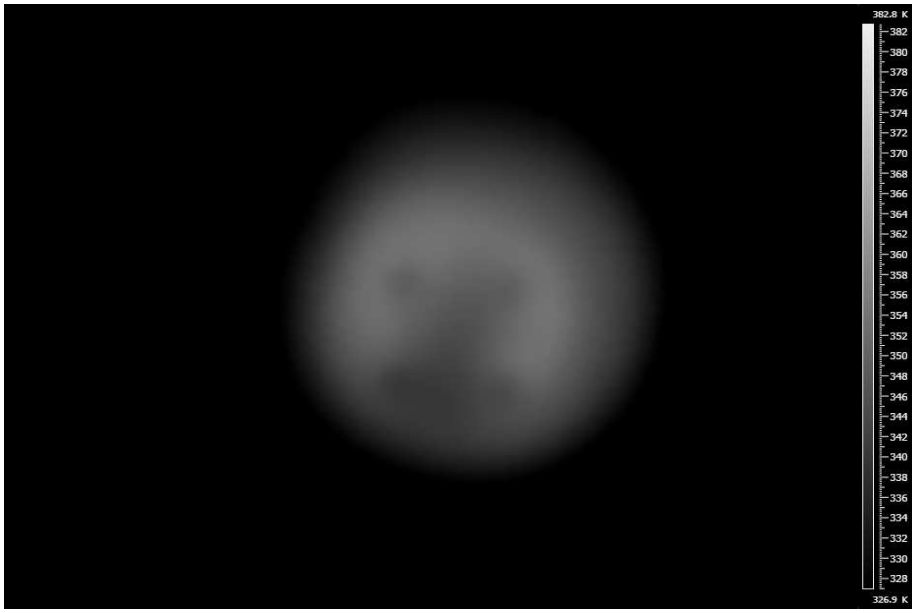

Figure 6.5: Image of temperature distribution for the defect size $\phi = 0.5''$ with the excitation frequency $\omega = 0.05\ rad/sec$

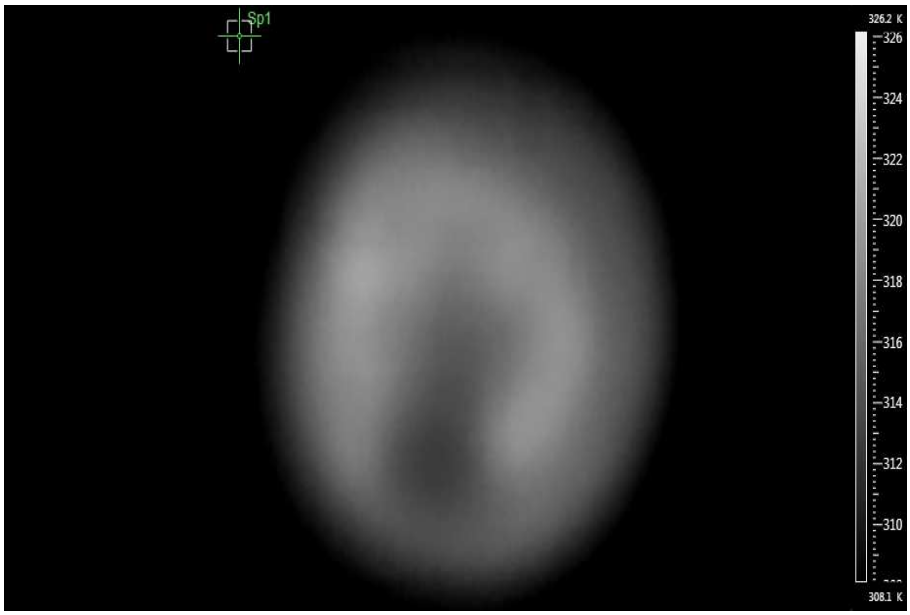

Figure 6.6: Image of temperature distribution for the defect size $\phi = 0.5''$ with the excitation frequency $\omega = 0.15\ rad/sec$

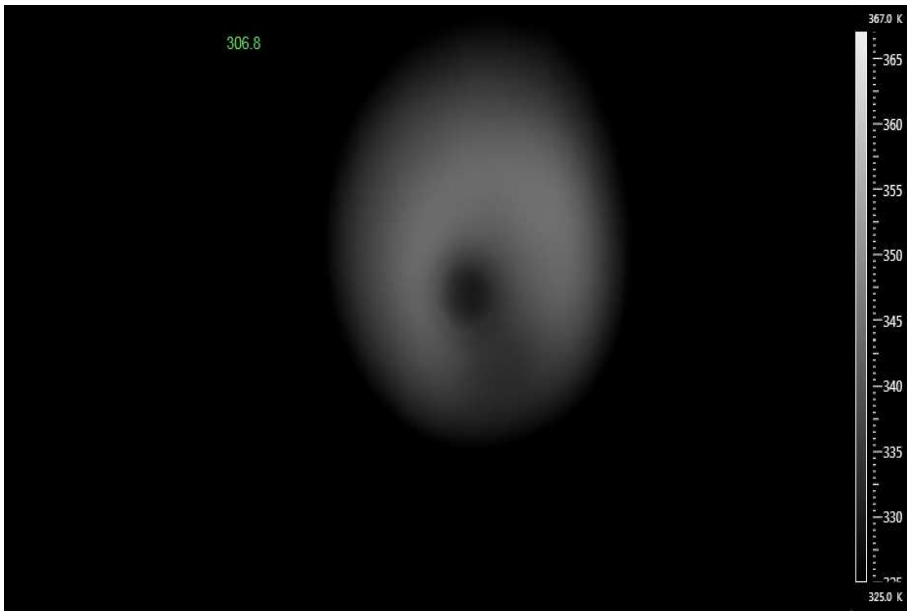

Figure 6.7: Image of temperature distribution for the defect size $\phi = 1''$ with the excitation frequency $\omega = 0.02\ rad/sec$

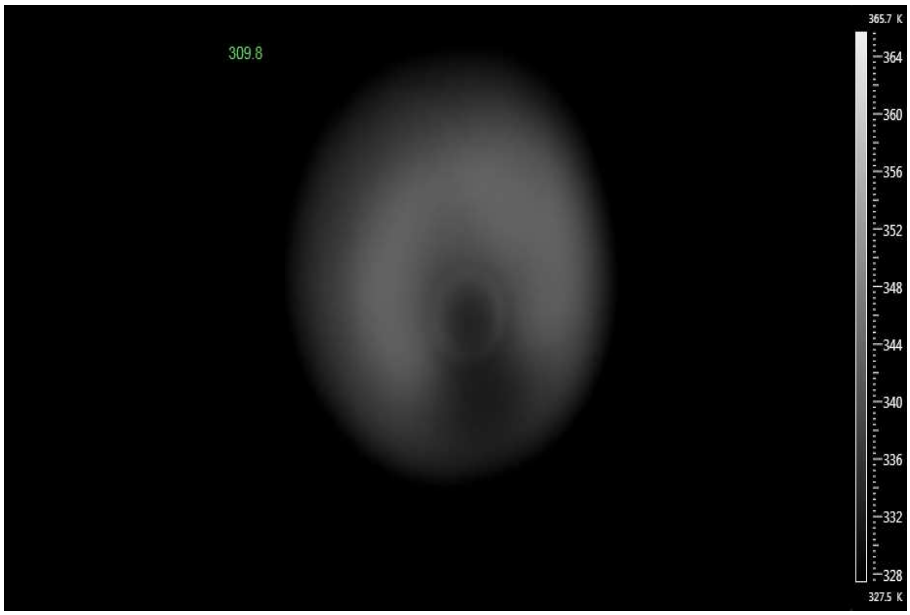

Figure 6.8: Image of temperature distribution for the defect size $\phi = 1''$ with the excitation frequency $\omega = 0.05\ rad/sec$

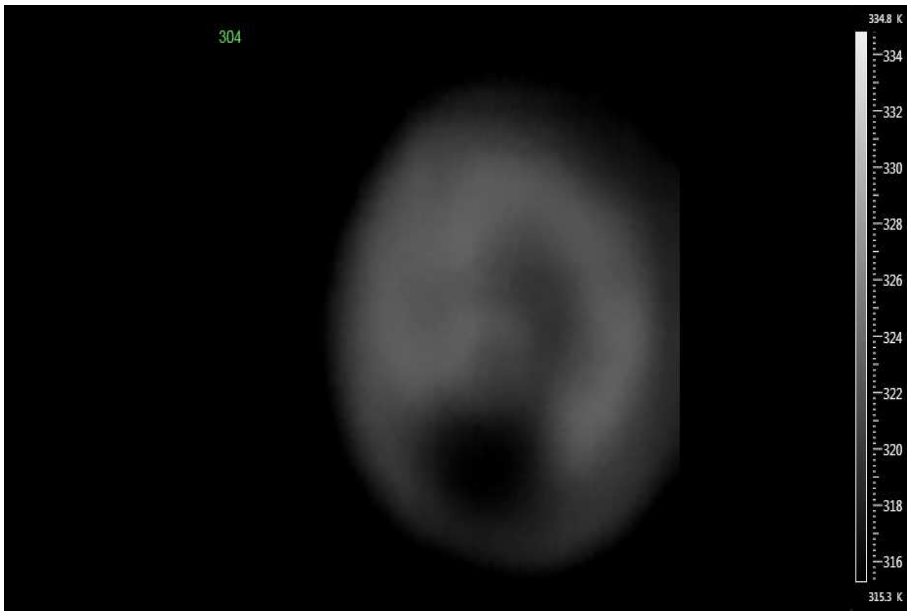

Figure 6.9: Image of temperature distribution for the defect size $\phi = 1''$ with the excitation frequency $\omega = 0.15\ rad/sec$

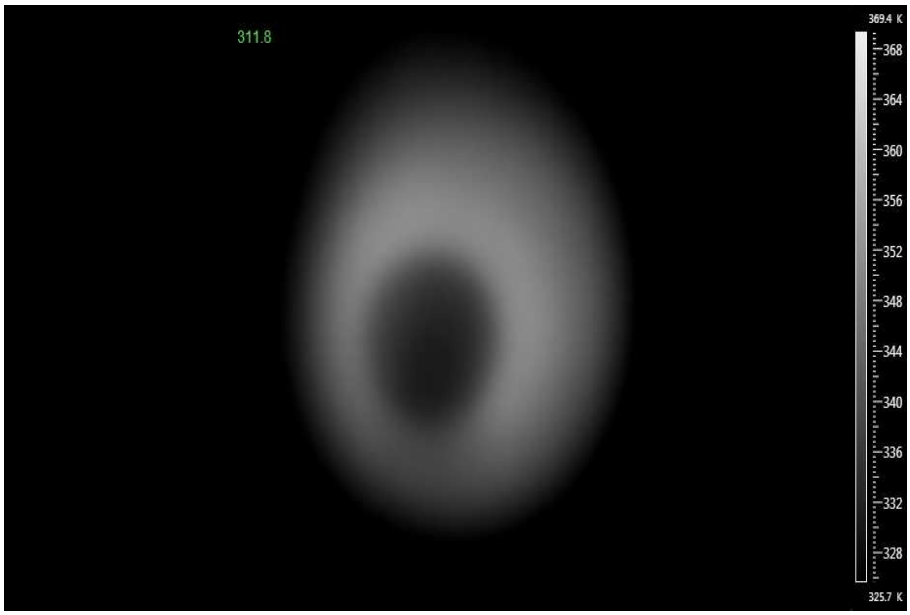

Figure 6.10: Image of temperature distribution for the defect size $\phi = 2''$ with the excitation frequency $\omega = 0.02\ rad/sec$

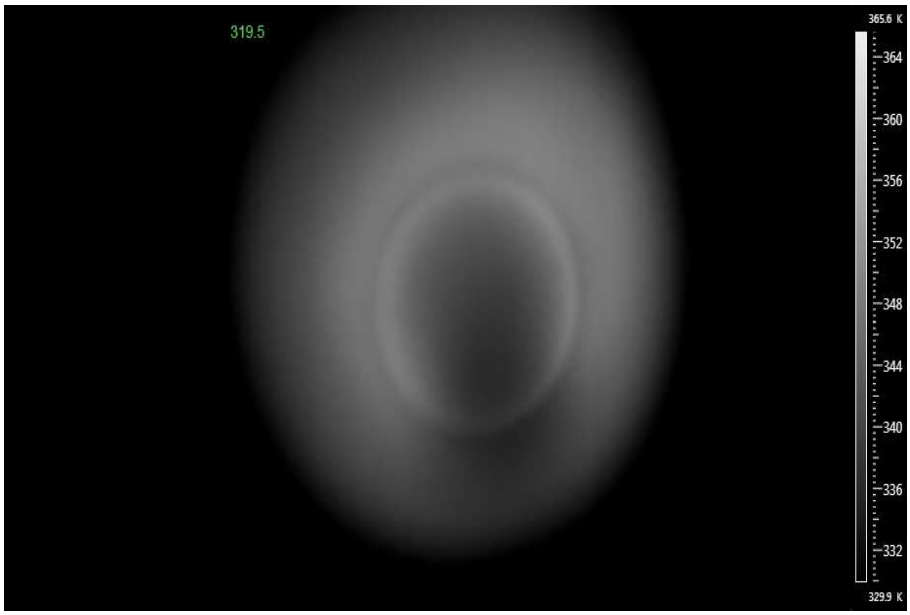

Figure 6.11: Image of temperature distribution for the defect size $\phi = 2''$ with the excitation frequency $\omega = 0.05\ rad/sec$

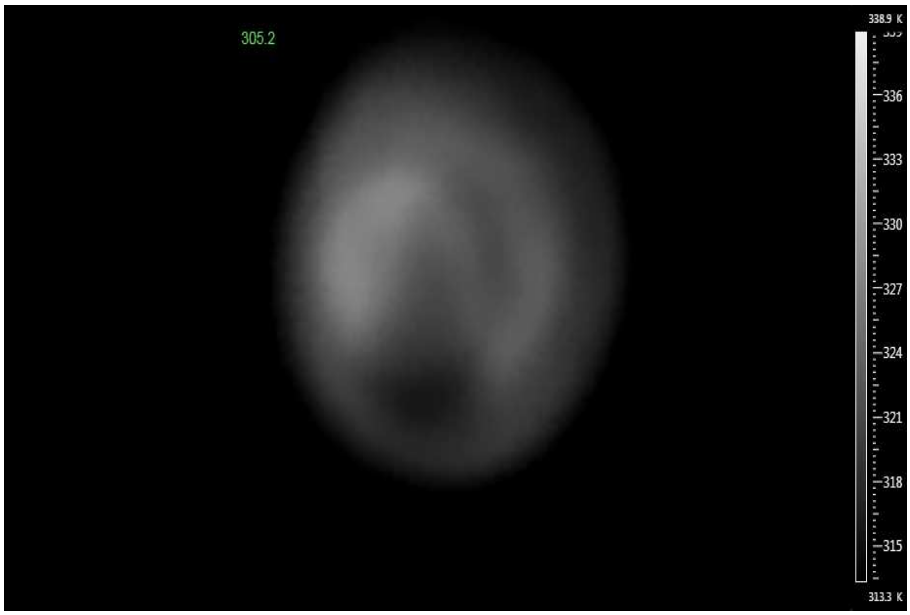

Figure 6.12: Image of temperature distribution for the defect size $\phi = 2''$ with the excitation frequency $\omega = 0.15\ rad/sec$

B. Single-layer

In order to test equation (4.7), the defefct-free of the panel is heated with a sinusoidal excitation. The temperature at the observation point (back side of the specimen) is obtained by capturing the image for each frequency of excitation, ω. The panel is excited for 3-4 cycles and in cooling down process the camera captures the temperature distribution of back side of the object. In (4.7), the temperature at observation point is normalized with the amplitude of the source. Amplitude of the heat source is captured by the camera right after beginning of the cool down process. This result is compared with the result from (4.7c), $N = 1$ and $N = 3$, that we presented in chapter 4. The comparison are shown in figure 6.13.

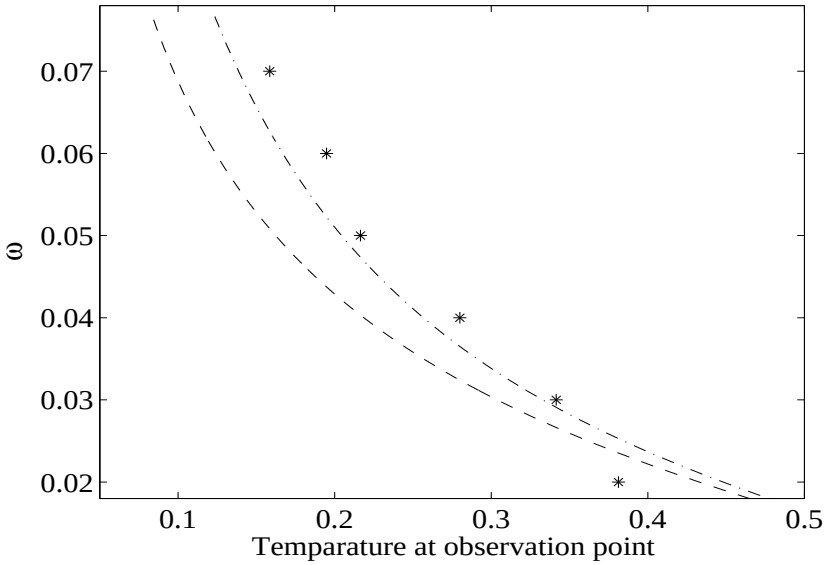

Figure 6.13: Plots of frequency of excitation versus temperature at observation point for comparison between the experiment result (*), approximation solution, (4.7c), for $N = 1$(dashed line),and approximation solution for $N = 3$ (dotted-dashed line) for material acrylic glass with the thickness of $6mm$.

C. Two-layer

We used the same parameters and procedure as in the single layer case. The comparison between the (4.7c), $N = 1$ and $N = 3$, and experimental result is plotted in figure 6.14

Conclusion for single and two-laye material

As the plots in figures, 6.13 and 6.14, show the experimental result are in a good agreement with the polynomial approximated solution. However, there are some unavoidable errors intrinsically associated to the basic equipments that we used and to the experimental protocol. Some of the possible sources of inaccuracy in the experimental procedure discrepancies with the models are

- In analytical analysis excitation is considered on the boundary. To produce this situation in experimental set up, we should locate the lamp very close to the surface of the panel. Close distance makes some damages to the surface. To avoid this damage we should increase the distance for excitation which leads to amplitude attenuation.

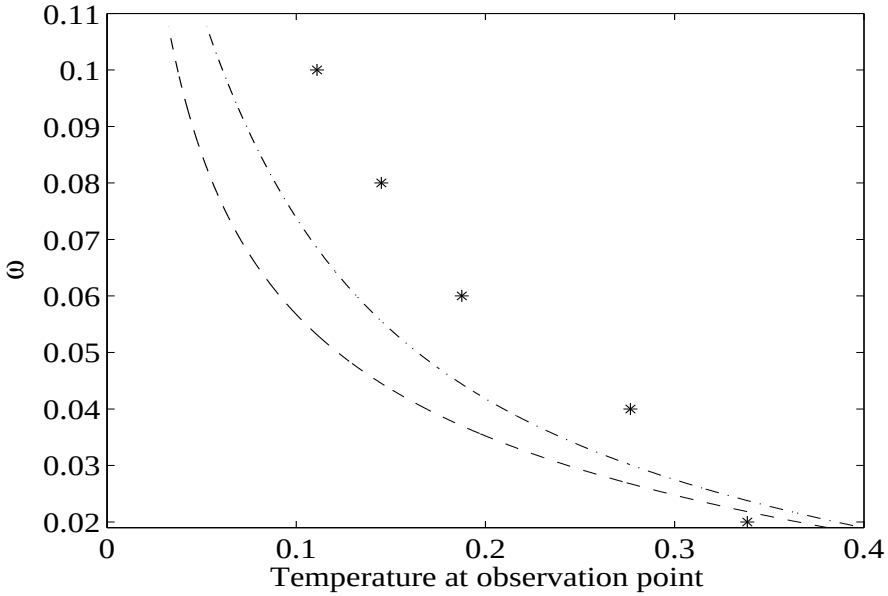

Figure 6.14: Plots of frequency of excitation versus temperature at observation point for comparison between the experiment result (*), approximation solution, (4.7c), for $N = 1$(dashed line),and approximation solution for $N = 3$ (dotted-dashed line) for two-layer panel with the thickness of $6mm$.

- the model is one dimensional and therefore heat conduction in the transversal directions is neglected.
- It is difficult to create a uniform excitation because of the curvature of the infrared lamp and because the Tungesten in the infrared lamp produces a concentrate excitation rather a distributed and uniform one. A uniform excitation can be obtained by increasing the distance between the lamp and the plate; however, there would not be a enough heat for excitation.
- Temperature stops raising after it reaches the melting temperature. It occurs when the panel is excited with low frequency,$\omega = 0.02$ for a long time. This is the reason of the big error associated to $\omega = 0.02$ in figures 6.13 and 6.14.
- human, equipment, and measurement error.

Chapter 7

Summary and Future work

7.1 Summary of contributions

- The relation between the frequency of excitation and temperature at observation point is estimated by an implicit polynomial solution for homogeneous and two-layer slab.
- A simple approximated formula based on first order truncation is obtained.
- The first order approximation can be an effective design tool for infrared non-destructive testing when the solution of the inverse problem is required
- The relation between the frequency of excitation and temperature at observation point is estimated in bi-quadratic structure for two layer slab with imperfect contact at interface:

  ✓The relation for the case when an air gap exists at interface is obtained.

  ✓The air gap is approximated with resistance in thermal quadrupole method.

  ✓The relation for the case when a conductive material exists at the interface is obtained.

  ✓This conductive material is approximated with capacitance in thermal quadrupole method.
- These estimated solutions can be used for predetermination of frequency of excitation in experimental infrared thermography.

- The detectability range predicted by the approximated formula are in good agreement with experimental results.
- These estimation formulas for homogeneous and two-layer slab are verified experimentally.
- The limitation and applicability of the simplified formula, [38], are assessed:

  ✓It can be used to detect a defect in thin plate.

  ✓The defect should be close to surface where the excitation is applied.
- Effect of finite length on simplified formula is investigated:

  ✓When the test point and convective boundary condition are in the same location, effect of finite length cannot be discarded.

  ✓For aluminum and carbon steel, critical lengths with the simplified formula is valid are obtained.
- The simplified formula for single-layer is verified experimentally that it can be used for predetermination of frequency of excitation for in experimental design.

7.2 Future work

The present study is motivated by the design of experiment for Infrared non-destructive testing techniques for single and multi-layer materials. Simple analytical model was derived for predetermination of frequency of excitation which can be used for different scenarios. This model allows to predict the range of frequencies necessary to detect a defect at a given depth in single-layer, two-layer and when an inclusion exists at the interface. The future work includes using this analytical model to find the location, size and characteristic of the possible anomalies for parameter predetermination in experiment design of non-destructive testing and damage detection in solid.

Appendix A

MATLAB codes

A.1 MATLAB code for single layer wall with persistant sinusoidal osciliation on the boundary

```
k=49.8;h=20;D=7872;C=473;Tinf=0;T0=0;l=.03;H0=1;        for Carbon steel
x=0:.000001:l;t=.01;kk=0;
for w=.001:.001:ww
Alfa=k/(C*D);
S=(1+1i)*sqrt(w/(2*Alfa));
T1=zeros(1,length(x));
T11=zeros(1,length(x));
Ttot=zeros(1,length(x));
A=H0*(((k*S-h)/(k*S+h))*(exp(-2*S*l)/(1-((h-k*S)/(k*S+h))*exp(-2*S*l))));
B=(H0/(1-((h-k*S)/(k*S+h))*exp(-2*S*l)));
for ii=1:1:length(x)
T1(ii)=(A*exp(S*x(ii))+B*exp(-S*x(ii)))*exp(1i*w*t);
T11(ii)=abs(T1(ii));
Ttot(ii)=T11(ii);
end
kk=kk+1;
TG(kk)=Ttot(length(x));
omega(kk)=w;
end
figure
```

```
plot(TG,omega,'blue')
```

A.2 MATLAB code for single layer wall in Fourier series

```
k=49.8;h=20;D=7872;C=473;Tinf=0;T0=0;l=.1;N=50;U=1;delta=.001; kk=0;
for l=.03:.02:.4
x=0:delta:l;
t=0:1:300;
T00=0;
M=zeros(1,N);
An=zeros(1,length(x));
u=zeros(length(x),length(t));
S=zeros(length(x),length(t));
HH=zeros(1,length(t));
Err1=zeros(1,length(l));
MaxFS1=zeros(1,length(l));
Landa=zeros(1,N);
a=zeros(1,length(x));
A=zeros(1,length(x));
for jj=1:1:length(t)
for ii=1:1:length(x)
for ll=1:1:N
Landa=((ll-.5)*pi)/l;
M(ll)=(1/2)*(l-sin(Landa*l*2)/(2*Landa));
a=(k/(D*C))*Landa^2;
An=(1/M(ll))*((h*Tinf/(h*l+k))*(-sin(Landa*l)/(Landa^2)...
+l*cos(Landa*l)/Landa));
A=(1/M(ll))*(w*U/(w^2+a^2))*(1/Landa)*((h/(k+h*l))*(-l*cos(Landa*l)....
+sin(Landa*l)/Landa)+cos(Landa*l)-1);
u(ii,jj)=u(ii,jj)+A*sin(Landa*x(ii))*(w*sin(w*t(jj))+a*cos(w*t(jj)))...
+(An-A*a)*exp(-a*t(jj))*sin(Landa*x(ii));
end
S(ii,jj)=((h*Tinf-h*U*sin(w*t(jj)))/(k+h*l))*x(ii)+U*sin(w*t(jj));
```

```
u(ii,jj)=u(ii,jj)+S(ii,jj);
if ii==.03/delta+1 && t(jj)>=50
HH(jj)=u(ii,jj);
end
end
end
```

A.3 MATLAB code for single layer wall using quadrupole method

```
K1=49.8;Den1=7872;Cap1=473;l1=.03;          Carbon steel3
w=input('Omega=  ');
Hout=20;Tinf=0;
Area=1;
tmax=1180;
c=.0175;
N=350;
NT=3500;
dt=.1;
ii=0;
n=(1:N+1);
J=sqrt(-1);
Om=(n)*pi/tmax;
kk=0;
for ii=.001:.001:w;
M1=sqrt((J*ii)./a1);
\%Material Matrix;
A1=cosh(l1*M1);
B1=sinh(l1*M1)./(M1*K1*Area);
C1=K1*Area*M1.*sinh(l1*M1);
D1=A1;
M maltiplication                Matrix M
Bc=(A1)/Hout/Area+B1;
Transferfunction=abs(1./Bc./Hout./Area);
```

```
kk=kk+1;
TG(kk)=Transferfunction;
omega(kk)=ii;
BB(kk)=ii*a2./((l1+l2)^2);
end
```

A.4 MATLAB code for two layer wall using quadrupole method with inclusion at the interface (Resistance and Capacitance)

```
%K1=49.8;Den1=7872;Cap1=473;l1=0.003; %matrial #1
a1=K1/(Den1*Cap1);
%K2=0.19;Den2=1410;Cap2=880;l2=.002;  %matrial #2
% a2=K2/(Den2*Cap2);
%% Boundary Condition
w=input('Omega=  ');
Hout=20;Tinf=0;R=.01;
Area=pi*R^2;
la1=0.001;la2=0.001;l3=.00005;        %inclusion geometry
%l1=l1-l3;
%% Capacitant properties
Roa=1.293;                            %inclusion material propertis
Ca=1005;
Ka=.0243;
V=pi*(la1+la2)*(R)^2;
Ct=Roa*Ca*V;                          %Capacitant value
%% Material for Laplace Transform
tmax=1180;c=.0175;N=350;NT=3500;dt=.1;
ii=0;
n=(1:N+1);
J=sqrt(-1);
Om=(n)*pi/tmax;
kk=0;
for ii=.01:.01:w;
```

```
%% Material Matrix
M1=sqrt((J*ii)./a1);
M2=sqrt((J*ii)./a2);
%M1 for material #1                %calculation of laplace parameters
A1=cosh(l1*M1);
B1=sinh(l1*M1)./(M1*K1*Area);
C1=K1*Area*M1.*sinh(l1*M1);
D1=A1;
%M2 for material #2                %calculation of laplace parameters
A2=cosh(l2*M2);
B2=sinh(l2*M2)./(M2*K2*Area);
C2=K2*Area*M2.*sinh(l2*M2);
D2=A2;
%%
R=(l3)/(Ka*Area);
%% %M maltiplication
%Bc=D2*(B1 + A1*Rcontact) + A1*B2 + (C2*(B1 + A1*Rcontact)....
 + A1*A2)/(Area*Hout);
%Bc=(B2*(A1 + B1*Ct1))/(Area*Hout) + B1*D2;
Bc=D2*(B1 + A1*R) + A1*B2 + (C2*(B1 + A1*R) + A1*A2)/(Area*Hout);
Bc1=(A1.*A2+B1.*C2)/Hout/Area+A1.*B2+B1.*D2;
Transferfunction=abs(1./Bc./Hout./Area);
Transferfunction1=abs(1./Bc1./Hout./Area);
kk=kk+1;
TG(kk)=Transferfunction;
TG1(kk)=Transferfunction1;
omega(kk)=ii;
BB(kk)=ii*a2./((l1+l2)^2);
dif(kk)=abs(TG(kk)-TG1(kk));
end
%% Numerical Laplace Transform by Classic Fourier
%for i=1:NT
% t=i*dt;
% T2(i)=(exp(c*t)*(1/tmax)*sum(real(Teta2).*cos(Om*t)....
-imag(Teta2).*sin(Om*t))+exp(c*t)*(1/2/tmax)*real(Teta2(1)));
```

```
% end
% plotting the results
```

Bibliography

[1] D.P. Almond and S.K. Lau. Defect sizing by transient thermography. i. an analytical treatment. *Journal of Physics D: Applied Physics*, 27:1063, 1994.

[2] N.P. Avdelidis, D.P. Almond, A. Dobbinson, B.C. Hawtin, C. Ibarra-Castanedo, and X. Maldague. Aircraft composites assessment by means of transient thermal ndt. *Progress in Aerospace Sciences*, 40(3):143–162, 2004.

[3] O. Balima, J. Boulanger, A. Charette, and D. Marceau. Near infra-red imaging with the radiative transfer equation: A comparative study with finite elements. In *Proceeding international conference on Quantitative Infrared Thermography (QIRT)*, July 27-30 2010.

[4] D. Betounes. *Partial Differential Equations for Computational Science with Maple and Vector Analysis*. Springer, 1998.

[5] G.M. Carlomagno and C. Meola. Comparison between thermographic techniques for frescoes ndt. *NDT & E International*, 35(8):559–565, 2002.

[6] M. Cehlin, B. Moshfegh, and M. Sandberg. Visualization and measuring of air temperatures based on infrared thermography. In *Proc. 7th Int. Conf. on Air Distribution in Rooms ROOMVENT 2000 (Reading, UK, 9–12 July 2000)*, 2000.

[7] R. Chowdhury. Active infrared (IR) thermographic testing procedure by 3-d finite element analysis and experimental correlation. Master's thesis, Wayne Sate University, 2004.

[8] J. Dumoulin, C. Ibarra-Castanedo, M. Quiertant, F. Taillade, A. Bendada, and X. Maldague. Evaluation of frp gluing on concrete structures by active infrared thermography. In *Proceeding international conference on Quantitative Infrared Thermography (QIRT)*, July 27-30 2010.

[9] J. Dumoulin, L. Ibos, C. Ibarra-Castanedo, A. Mazioud, M. Marchetti, X. Maldague, and A. Bendada. Active infrared thermography applied to defect detection and characterization on asphalt pavement samples: comparison between experiments and numerical simulations. *Journal of modern optics*, 57(18):1759–1769, 2010.

[10] D. Spinello E. Borazjani and D. Necsulescu. Design of infrared non-destructive testing for damage detection in multi-layer materials. In *Proceeding international conference on Quantitative Infrared Thermography (QIRT)*, June 11-14 2012.

[11] V. Feuillet, L. Ibos, M. Fois, J. Dumoulin, and Y. Candau. Defect detection and characterisation in composite materials using active infrared thermography coupled with svd analysis and thermal quadrupole modeling. In *Proceeding international conference on Quantitative Infrared Thermography (QIRT)*, July 27-30 2010.

[12] BAM Federal Institute for Materials Researchand Testing. Bam. `http://www.bam.de/en/index.htm`, Accessed on Dec 2010.

[13] Frazer. Frazer does physics. `http://frazerphysics.blogspot.ca/2011/05/311-order-of-electromagnetic-spectrum.html`, Accessed on Dec 2010 1921.

[14] M. Genest, M. Martinez, N. Mrad, G. Renaud, and A. Fahr. Pulsed thermography for non-destructive evaluation and damage growth monitoring of bonded repairs. *Composite Structures*, 88(1):112–120, 2009.

[15] V.S. Ghali, N. Jonnalagadda, and R. Mulaveesala. Three-dimensional pulse compression for infrared nondestructive testing. *Sensors Journal, IEEE*, 9(7):832–833, 2009.

[16] K.K. Ghosh and V.M. Karbhari. Use of infrared thermography for quantitative nondestructive evaluation in frp strengthened bridge systems. *Materials and Structures*, 44(1):1–17.

[17] G. Gralewicz, G. Owczarek, and B. Wikecek. Investigations of single and multilayer structures using lock-in thermography-possible applications. *International Journal of Occupational Safety and Ergonomics (JOSE)*, 11(2):211–215, 2005.

[18] G. Gralewicz, J. Wozny, G. Owczarek, and B. Wikecek. Detecting flaws in composite materials–thermal model and simulation results. In *Proceeding international conference on Quantitative Infrared Thermography (QIRT)*, 2008.

[19] H.Carlslaw and J.Jaeger. *Conduction of Heat in Solid*. Oxford, 1959.

[20] A. Hellen, A. Mandelis, Y. Finer, and B.T. Amaechi. Real-time monitoring of dental lesions using transmission-mode photothermal radiometry and modulated luminescence. In *Proceeding international conference on Quantitative Infrared Thermography (QIRT)*, July 27-30 2010.

[21] J.P. Holman. *Heat Transfer*. Mcgraw-Hill, 2010.

[22] M. Jonsson, B. Rendahl, and I. Annergren. The use of infrared thermography in the corrosion science area. *Materials and Corrosion*, 61:961–965, 2010.

[23] L. Junyan, L. Huijuan, W. Yang, and D. Jingmin. Defect estimation of aircraft and aerospace components based on neural network using lock-in thermography. In *Proceeding international conference on Quantitative Infrared Thermography (QIRT)*, July 27-30 2010.

[24] R. Krankenhagen, GN Kervalishvili, and C. Maierhofer. Influence of air-gaps on the thermal behaviour of the plaster-concrete bond. In *Proceeding international conference on Quantitative Infrared Thermography (QIRT)*, July 27-30 2010.

[25] W.B. Larbi, C. Ibarra-Castanedo, M. Klein, A. Bendada, and X. Maldague. Experimental comparison of lock-in and pulsed thermography for the nondestructive evaluation of aerospace materials. In *6 th International Workshop, Advances in Signal Processing for Non Destructive Evaluation of Materials (IWASPNDE), Ontario, Canada*. Citeseer, 2009.

[26] B. Larson. Ndt education resource center. `http://www.ndt-ed.org/index_flash.htm`, Accessed on Dec 2010.

[27] J.S. Leng and A. Asundi. Non-destructive evaluation of smart materials by using extrinsic fabry-perot interferometric and fiber Bragg grating sensors. *NDT & E International*, 35(4):273–276, 2002.

[28] A. Lesniak and B. Bukowska-Belnia. Detecting the wastewater leakage from cesspool using noisy thermographic images. In *Proceeding international conference on Quantitative Infrared Thermography (QIRT)*, July 27-30 2010.

[29] F. R. Lopez and V. P. Nicolau. Thermal sensitivity analysis applied on infrared thermography evaluation. In *Proceeding international conference on Quantitative Infrared Thermography (QIRT)*, July 27-30 2010.

[30] D. Maillet, S. Andre, J. C. Batsale, A. Degiovanni, and C. Moyne. *Thermal Quadrupoles: Solving the Heat Equation through Integral Transforms*. Wiley, 2000.

[31] X. Maldague, F. Galmiche, and A. Ziadi. Advances in pulsed phase thermography. *Infrared Physics & Technology*, 43(3-5):175–181, 2002.

[32] M. Marchetti, M. Moutton, S. Ludwig, L. Ibos, V. Feuillet, and J. Dumoulin. Implementation of an infrared camera for road thermal mapping. In *Proceeding international conference on Quantitative Infrared Thermography (QIRT)*, July 27-30 2010.

[33] P. Menner, C. Spiessberger, A. Gleiter, and G. Busse. Aerospace applications of lock-in thermography with optical, ultrasonic and inductive excitation. In *AIP Conference Proceedings*, volume 1211, page 525, 2010.

[34] C. Meola and G.M. Carlomagno. Recent advances in the use of infrared thermography. *Measurement Science and Technology*, 15(9):R27, 2004.

[35] C. Meola and G.M. Carlomagno. Impact damage in gfrp: New insights with infrared thermography. *Composites Part A: Applied Science and Manufacturing*, 41:1839–1847, 2010.

[36] C. Meola, GM Carlomagno, D. Annicchiarico, M. Giordano, and M. Zarrelli. Detection of delamination in carbon-fibre-reinforced polymers with lock-in thermography. *Proceedings of the Institution of Mechanical Engineers, Part G: Journal of Aerospace Engineering*, 224(11):1–9, 2010.

[37] J.M. Milne and WN Reynolds. The non-destructive evaluation of composites and other materials by thermal pulse video thermography. In *Society of Photo-Optical Instrumentation Engineers (SPIE) Conference Series*, volume 520, page 119, 1985.

[38] D. Necsulescu, S. Bayat, and M. Eghtesad. IR non destructive testing experiment design. In *Proceeding international conference on Quantitative Infrared Thermography (QIRT)*, July 27-30 2010.

[39] D. Necsulescu, D. Spinello, E. Borazjani, and S. Bayat. Analytical and simulation investigation of the experimental design for infrared non destructive testing. In *Control & Automation (MED), 2011 19th Mediterranean Conference on*, pages 946–951. IEEE, 2011.

[40] NetComposites. Interactive knowledge base on nde of composites. `http://www.netcomposites.com`, Accessed on Dec 2010.

[41] K. Ogata. *Modern control engineering*. Prentice Hall PTR, 2009.

[42] M. N. Özişi and H. R. B. Orlande. *Inverse Heat Transfer: Fundamentals and Applications*. Taylor & Francis, 2000.

[43] M. Ceseri P. Bison and G. Inglese. Detecting hidden defects on a thin metalic plate. In *Proceeding international conference on Quantitative Infrared Thermography (QIRT)*, July 27-30 2010.

[44] A. Bendada R. S. Ghiass and X. Maldague. Infrared face recognition: A review of the state of the art. In *Proceeding international conference on Quantitative Infrared Thermography (QIRT)*, July 27-30 2010.

[45] N. Rajic. Principal component thermography for flaw contrast enhancement and flaw depth characterisation in composite structures. *Composite Structures*, 58(4):521–528, 2002.

[46] W.M. Rohsenow, J.P. Hartnedd, and Y.I. Cho. *Handbook of Heat Transfer*. Addison-Wesley, third edition, 1998.

[47] M.R. Sharlon. Active thermography: An overview of methods and their applications in use today. `http://www.irinfo.org/articles/1_1_2008_sharlon.html`, Accessed on Dec 2010.

[48] S.M. Shepard. Introduction to active thermography for non-destructive evaluation. *Anti-Corrosion Methods and Materials*, 44(4):236–239, 1997.

[49] P.J. Shull. *Nondestructive Evaluation: Theory, Techniques, and Applications*. Dekker, New York, 2002.

[50] S. Švaić, I. Boras, and N. Ferdekji. Implementation of Thermography for Determination of Air Jet Geometry in HVAC Systems. In *Proceeding international conference on Quantitative Infrared Thermography (QIRT)*, July 27-30 2010.

[51] C. Wallbrink, S.A. Wade, and R. Jones. The effect of size on the quantitative estimation of defect depth in steel structures using lock-in thermography. *Journal of applied physics*, 101:104907, 2007.

[52] B. Wiecek, T. Wajman, G. Gralewicz, and S. Zwolenik. Theory and measurement of single and multilayer structures using lock-in and pulse thermography. In *Proceedings of SPIE*, volume 5073, page 505, 2003.

[53] M. Willcox and G. Downes. A brief description of ndt techniques. `http://www.turkndt.org/sub/makale/ornek/`, Accessed on Dec 2010.

[54] M. Wisniewski, S.E. Lindow, and E.N. Ashworth. Observations of ice nucleation and propagation in plants using infrared video thermography. *Plant Physiology*, 113(2):327, 1997.

[55] D. Wu and G. Busse. Lock-in thermography for nondestructive evaluation of materials. *Revue generale de thermique*, 37(8):693–703, 1998.

[56] D. Wu, T. Zweschper, A. Salerno, and G. Busse. Lock-in thermography for nondestructive evaluation of aerospace structures. *NDT.net (Online)*, 3(9), Sep 1998.

[57] Xenics. Xenics infrared solution. `http://www.xenics.com/en/infrared_technology/infrared_detector_history.asp`, Accessed on Dec 2010.